UC San Diego
UC San Diego Electronic Theses and Dissertations

Title

Chaotic ultrasonic excitation and statistical pattern recognition for structural damage classification

Permalink

https://escholarship.org/uc/item/2qs7m55h

Author

Fasel, Timothy R.

Publication Date

2009

Peer reviewed|Thesis/dissertation

eScholarship.org Powered by the California Digital Library
University of California

UNIVERSITY OF CALIFORNIA, SAN DIEGO

Chaotic Ultrasonic Excitation and Statistical Pattern Recognition for Structural Damage Classification

A Dissertation submitted in partial satisfaction of the
Requirements for the degree Doctor of Philosophy

in

Structural Engineering

by

Timothy R. Fasel

Committee in charge:

Michael D. Todd, Chair
Francesco Lanza di Scalia
Charles R. Farrar
Hyonny Kim
William S. Hodgkiss
Gyuhae Park

2009

Copyright

Timothy R. Fasel, 2009

All rights reserved.

The Dissertation of Timothy R. Fasel is approved, and it is acceptable in quality and form for publication on microfilm and electronically:

Chair

University of California, San Diego

2009

TABLE OF CONTENTS

LIST OF ABBREVIATIONS

SHM	structural health monitoring
NDE	non-destructive evaluation
HUMS	health and usage monitoring
MFC	macro fiber composite
AR	auto-regressive
CUW	chaotic ultrasonic wave
DAQ	data acquisition
AMI	average mutual information
SVD	singular value decomposition
FNN	false nearest neighbor
DSP	digital signal processing
FIR	finite impulse response
IIR	infinite impulse response
ADC	analog-to-digital converter
DAC	digital-to-analog converter
MSB	most significant bit
LSB	least significant bit
SNR	signal-to-noise ratio
RMS	root mean square
MAC	modal assurance criterion
VCC	vector consistency criterion
pdf	probability density function

cdf	cumulative distribution function
EVS	extreme value statistics
DC	direct current
PZT	piezoelectric
NI	National Instruments
CFRP	carbon fiber-reinforced plastic
ROC	receiver operating characteristic

LIST OF SYMBOLS

y_n	chaotically modulated waveform
f_c	carrier frequency
f_s	sampling frequency
d	modulation depth
x_n	original chaotic waveform
x_1, x_2, x_3	Lorenz system coordinates
R	frequency ratio
$X(n)$	reconstructed attractor
$x(n)$	original time series
T	time delay
m	embedding dimension
N	number of bits
I	current
F	number of fiducial points
$X_1(n)$	baseline attractor
$X_2(n)$	comparison attractor
P	number of nearest neighbors
s	prediction horizon
$\gamma_{CC,f}$	prediction error for a particular fiducial point
f	fiducial point
n_f	initial time index for a particular fiducial point

$c_{1f}(n_f+s)$	centroid of the neighborhood of the baseline attractor
$c_{2f}(n_f+s)$	centroid of the neighborhood of the comparison attractor
p	AR model order
α_i	AR coefficients
$\mathbf{e}(n)$	residual error
ψ_t	test modal vector
ψ_r	reference modal vector
H	Hermitian operator
λ, δ, β	EVS distribution parameters
n	window size used to extract minima
α	type-I error level
μ_b, μ_c	mean of baseline and comparison distributions
σ_b, σ_c	standard deviation of baseline and comparison distributions
V_1, V_2, V_3	parameter vectors
F	scaling factor
CR	crossover constant
N	signal length

LIST OF FIGURES

LIST OF TABLES

ACKNOWLEDGEMENTS

I would like to give special thanks to my advisor, Michael Todd. His constant support, advice and commitment to my research have been invaluable. No doubt I would not have been able to achieve as well as I did without his guidance. I would like to thank my other committee members Francesco Lanza di Scalea, Gyuhae Park, Chuck Farrar, Hyonny Kim and William Hodgkiss for their guidance and technical contributions. Especially I would like to thank Gyuhae Park for his one-on-one guidance that he gave me while I was working at Los Alamos National Laboratory as well as Chuck Farrar for accepting my application to the Los Alamos National Laboratory Dynamics Summer School and showing me there the importance of graduate school and obtaining an advanced degree. I would not have come this far without either of you. I would also like to thank Francesco Lanza di Scalea and Hyonny Kim for furnishing test structures that were of great use to me in completing this dissertation

Thanks to my friends and collaborators at UCSD including Matt Kennel for his ideas on group classification theory, and Colin Olson and Luke Overbey for being there to supply intellectual inspiration as well as mind-relaxing activities through the majority of my time here at UCSD (although I took a little longer to finish). Thank you also to my family without whose constant moral (and monetary) support completing this dissertation would certainly have been much more difficult.

I would like to acknowledge funding through the UCSD/Los Alamos National Laboratory Engineering Institute for Structural Health Monitoring, Damage Prognosis, and Validated Simulations and the American Society of Engineering Education via a

National Defense Science and Engineering Graduate Fellowship. This work was also supported by the Air Force Office of Scientific Research (Dr. Victor Giurgiutiu, Program Manager) under contract #FA9550-07-1-0016.

Sections 1 and 3, in part, are in print in the *Journal of Smart Structures and Systems*, Fasel, T.R.; Todd, M.D.; Clayton, E.H.; Park, G., 2009. The title of this paper is “Damage state evaluation of experimental and simulated bolted joints using ultrasonic chaotic waves.” The dissertation author was the primary investigator and author of this paper.

Section 2, in part, has been submitted for publication in *Structural Health Monitoring*, Fasel, T.R.; Todd, M.D., 2009. The title of this paper is “Changes in signal dimension of chaotic ultrasonic waves during data acquisition and generation.” The dissertation author was the primary investigator and author of this paper.

Sections 3 and 4, in part, have been published in the *Proceedings of the SPIE 11th Annual International Symposium on NDE for Health Monitoring and Diagnostics*, Fasel, T.R.; Todd, M.D.; Park, G., 2006. The title of this paper is “Active chaotic excitation for bolted joint monitoring.” The dissertation author was the primary investigator and author of this paper.

Section 4, in part, has been published in the *Proceedings of the SPIE 11th Annual International Symposium on NDE for Health Monitoring and Diagnostics*, Fasel, T.R.; Todd, M.D.; Park, G., 2006. The title of this paper is “Plate damage identification using up-converted chaotic excitations.” The dissertation author was the primary investigator and author of this paper.

Section 5, in part, has been published in the *Proceedings of the SPIE 13th Annual International Symposium on NDE for Health Monitoring and Diagnostics*, Fasel, T.R.; Olson, C.C.; Todd, M.D., 2008. The title of this paper is "Optimized guided wave excitations for health monitoring of a bolted joint." The dissertation author was the primary investigator and author of this paper.

Sections 5, in part, has been submitted for publication in *Mechanical Systems and Signal Processing*, Fasel, T.R.; Todd, M.D., 2009. The title of this paper is "Chaotic insonification for health monitoring of a bonded composite skin-to-spar joint." The dissertation author was the primary investigator and author of this paper.

Sections 3 and 5, in part, have been submitted for publication in the *Journal of Sound and Vibration*, Fasel, T.R.; Todd, M.D., 2009. The title of this paper is "An adhesive bond state classification method for a composite skin-to-spar joint using chaotic insonification." The dissertation author was the primary investigator and author of this paper.

VITA

2002	B.S., Aerospace Engineering, Case Western Reserve University
2005	M.S., Structural Engineering, University of California, San Diego
2009	Ph.D., Structural Engineering, University of California, San Diego

PUBLICATIONS

Journal Publications

Fasel, T.R. and Todd, M.D. (2009). An adhesive bond state classification method for a composite skin-to-spar joint using chaotic insonification, *J. of Sound and Vibration*, in review.

Fasel, T.R. and Todd, M.D. (2009). Chaotic insonification for health monitoring of an adhesively-bonded composite skin-to-spar joint, *Mechanical Systems and Signal Processing*, in review.

Fasel, T.R. and Todd, M.D. (2009). Changes in signal dimension of chaotic ultrasonic waves during data acquisition and generation, *Structural Health Monitoring: An International Journal*, in review.

Fasel, T.R., Kennel, M.B., Todd, M.D., Clayton, E.H. and Park, G. (2009). Damage state evaluation of experimental and simulated bolted joints using ultrasonic chaotic waves, *J. of Smart Structures and Systems,* in press.

Salamone, S., Fasel, T.R., Bartoli, I., Srivastava, A., Lanza di Scalea, F. and Todd M.D. (2009). Health monitoring approach for adhesively bonded joints, *Materials Evaluation*, **67**(7): 828-836.

Fasel, T.R., Sohn, H., Park, G. and Farrar, C.R. (2005). Active sensing using impedance-based ARX model and extreme value statistics for damage detection, *Earthquake Engineering and Structural Dynamics*, **34**(7): 763-785.

Conference Publications

Fasel, T.R., Olson, C.C. and Todd, M.D. (2008). Optimized guided wave excitations for health monitoring of a bolted joint, *Proceedings of the SPIE 13th Annual International Symposium on NDE for Health Monitoring and Diagnostics*, San Diego, CA, March.

Fasel, T.R., Kennel, M.B., Todd, M.D., Clayton, E.H., Stabb, M.C. and Park, G. (2008). Bolted joint damage assessment using chaotic probes, *Proceedings of the International Modal Analysis Conference XXVI*, Orlando, FL, February.

Todd, M.D., Fasel, T.R. and Park, G. (2006). Health monitoring of a bolted lap joint using active chaotic excitation with guided waves, *Proceedings of the 3rd European Workshop on Structural Health Monitoring*, Granada, Spain, July.

Fasel, T.R., Todd, M.D. and Park, G. (2006). Active chaotic excitation for bolted joint monitoring, *Proceedings of the SPIE 11th Annual International Symposium on NDE for Health Monitoring and Diagnostics*, San Diego, CA, March.

Fasel, T.R., Todd, M.D. and Park, G. (2006). Plate damage identification using up-converted chaotic excitations, *Proceedings of the SPIE 11th Annual International Symposium on NDE for Health Monitoring and Diagnostics*, San Diego, CA, March.

Fasel, T.R., Todd, M.D. and Park, G. (2005). Piezoelectric active sensing using chaotic excitations and state space reconstruction, *Proceedings of the SPIE 10th Annual International Symposium on NDE for Health Monitoring and Diagnostics*, San Diego, CA, March.

Fasel, T.R. and Todd, M.D. (2005). Effects of data acquisition and generation on using upconverted chaotic waves for active structural health monitoring, *Proceedings of the International Modal Analysis Conference XXIII*, Orlando, FL, February.

Fasel, T.R., Park, G., Sohn, H. and Farrar, C.R. (2003). Application of frequency domain ARX models and extreme value statistics to impedance-based damage detection, *International Mechanical Engineering Congress and Exposition Winter Annual Meeting of the ASME,* Washington, D.C., November.

Fasel, T.R., Sohn, H. and Farrar, C.R. (2003). Damage detection using extreme value statistics on frequency domain ARX models, *Proceedings of the SPIE 9th Annual International Symposium on NDE for Health Monitoring and Diagnostics*, San Diego, CA, March.

Fasel, T.R., Gregg, S.W., Johnson, T.J., Farrar, C.R. and Sohn, H. (2002). Experimental modal analysis and damage detection in a simulated three story building, *Proceedings of the International Modal Analysis Conference XX*, Los Angeles, CA, February.

ABSTRACT OF THE DISSERTATION

Chaotic Ultrasonic Excitation and Statistical Pattern Recognition for Structural Damage Classification

by

Timothy R. Fasel

Doctor of Philosophy in Structural Engineering

University of California, San Diego, 2009

Professor Michael D. Todd, Chair

The desire to push aging civil, mechanical, and aerospace structures beyond their intended design lives has highlighted the need for structural health monitoring (SHM) strategies that are able to detect, locate, and quantify various forms of damage within them. SHM strategies may also be tailored for newly-deployed structures in an attempt to optimize their performance and maintenance over an entire life cycle so that

total ownership costs are reduced. Specifically within the aerospace industry, standard non-destructive evaluation (NDE) techniques have been used for decades for inspection of components and systems. One of the most common and widely-accepted NDE domains is ultrasonic inspection, where components are imaged with the component out of service. Recent advances in sensor technology, distributed networks, and advanced signal processing techniques have begun to be exploited for *in situ* ultrasonic (and other forms of) SHM systems that are being deployed in a wide variety of real-world structures. In most cases, however, the ultrasonic excitation signals and feature extraction techniques being employed are the same as the standard NDE methods that have been in use for decades and are only applicable to relatively simple component geometries. This dissertation contributes to the body of knowledge in this field by introducing a new class of excitation signals and pattern recognition algorithms that, when paired with novel sensor networks, improve on the ability of standard SHM techniques to locate and identify damage on more complex geometry systems, including bolted joints and composite materials.

This dissertation describes a methodology whereby chaotic guided waves are created and optimized (in a detection sense) and used as probes to perform damage assessment by building both time- and state-space domain models (rooted in pattern recognition) and using statistical modeling for performing damage classification under Type I/II error control. Multiple chaotic ultrasonic excitation formats are explored, including short-time chaotic wave packets and long-time chaotic bulk insonification, in which the diffuse, reverberant wave field is examined to identify structural changes. This method of insonification, in addition to enhanced pattern recognition techniques, allows this damage detection scheme to be employed on complex structural geometries with which standard ultrasonic-based SHM methods cannot be used.

The outlined SHM method is applied to various test structures with different forms of induced damage including an aluminum plate with corrosion damage, bolted connections on several aluminum test structures (single and multiple-bolt configurations) and several adhesively-bonded composite wing-to-spar structures. Chaotic signal creation parameters are optimized for the composite structures and attempts are made to examine and, where possible, compensate for several sources of variability, such as temperature, within-unit variability and unit-to-unit variability.

1 INTRODUCTION

Civil, mechanical, maritime, and aerospace structures are relied upon daily by most of the world's citizens to perform reliably and safely. All structures constantly interact with forces that tend to, over some time scale, degrade structural integrity. Sudden catastrophic events, e.g. earthquakes, can also introduce unexpected (and undesigned-for) damage into structures that could lead to significant economic or life-safety losses. The consequences of these losses supports a need for performing structural integrity assessments in a manner that supports improved life cycle performance of the structure: detecting performance-degrading trends in a way that supports decision-making to optimize safe service life at a minimized total ownership cost.

This need has subsequently led to research in the areas of non-destructive evaluation (NDE), structural health monitoring (SHM) and condition monitoring (Sohn, Farrar et al. 2003). NDE methods are based on visual procedures or localized experimental methods such as acoustic or ultrasonic methods, magnetic field methods, radiography, eddy-current methods and thermography (Bray and McBride 1992). A number of these approaches are highly-specific (and successful) at detecting various forms of damage or defects, but they share common limitations in usage such as highly localized applicability (small inspection range), non-automated expert execution, long inspection times and the lack of in-service inspectability. SHM is an implemented damage detection strategy that samples dynamic response measurements (from either an active or passive excitation source) that are recorded by a distributed array of sensors in-situ on the structure. Features that are sensitive to the particular type of damage that is likely to occur are then extracted from the recorded response measurements using advanced signal processing techniques. Statistical analysis is then employed on the damage-sensitive features to determine the structural health of the system (Farrar and Worden 2007). As SHM strategies have developed in recent years, individual application domains have created new terms for this general in-situ approach, such as condition monitoring in rotating machinery (Barron 1997), health and usage monitoring (HUMS) in the rotorcraft industry and process control in manufacturing operations.

1.1 Motivation

Traditional NDE methods for structural assessment are often expensive and time-consuming operations involving human operators and visual inspection. For example, the 1994 Northridge earthquake showed that steel moment-resisting frame structures are susceptible to brittle joint failure. During this earthquake, over 70% of steel frame buildings in Northridge suffered from some form of damage at moment-resisting joints. However, many of the damaged joints remained undetected until one was accidentally found. The cost of visually inspecting a single joint, by removing the architectural cladding and fire retardant, was approximately $10,000 (Paret 2000).

The total costs of these inspections, and the subsequent necessary repairs, are not negligible. For example, Hall and Conquest estimate that 27% of total life-cycle costs for an aircraft are associated with inspection and repair (Hall and Conquest 1999) and life-cycle costs are generally much higher than the purchase or manufacturing cost of an aircraft (Boller and Staszewski 2004). In addition to the cost of the inspection procedure, there is an additional cost associated with the removal of the structure from service, as is typically the case with aircraft, construction and military applications.

In addition to economic concerns resulting from loss of operation time and inspection costs, loss of human life is also of paramount concern for aircraft and civil structures. Recent incidents have illustrated the vital need for integrated online SHM systems in critical structures in order to protect human life. One famous example occurred in April, 1988 when Aloha Airlines Flight 243 suffered an explosive decompression in the fuselage that tore off a large section of the roof and resulted in the death of a flight attendant. Another aeronautical accident occurred on Alaska Airlines Flight 261 in January, 2000 when the horizontal stabilizer trim system jackscrew assembly failed resulting in the destruction of the plane and the death of all passengers and crew aboard. The collapse of the I-35W bridge in Minneapolis, MN in August, 2007 resulted in the death of thirteen people and injured 145.

Aerospace structures are increasingly being fabricated using composite materials due to their high strength-to-weight ratio. For example, the newly designed Boeing 787 Dreamliner will become the first full-size commercial aircraft with composite wings and fuselage. Composites on the 787 will account for fifty percent of the weight of the aircraft and aluminum will comprise only 12 percent of the aircraft. By comparison, the Boeing 777 (designed in the early 1990s) is comprised of only 12 percent composites and 50 percent aluminum by weight (Griffiths 2005). However, the long-term fatigue and degradation properties of these composite materials are still being researched. This lack of fundamental material properties knowledge necessitates the use of SHM as a means of assessing structural integrity because no long-term data are available to compile a reasonable *time-based maintenance* schedule. In this approach, maintenance and repairs are performed at regularly scheduled intervals based on assumed wear of the structural component involved. This maintenance is performed regardless of the actual condition of the component and therefore may be unnecessarily economically burdensome because parts that are still structurally sound may be getting replaced.

The economic impact of this *time-based maintenance* approach has led to the desire to implement a *condition-based maintenance* scheme. This approach would only replace a structural component when the true condition of the part necessitated its replacement or repair. There is no way to implement a *condition-based maintenance* approach without an effective and accurate SHM system that provides near real-time assessment of the structure's performance.

1.2 Statistical pattern recognition for SHM

The SHM process involves the extraction and classification of damage-sensitive features from recorded dynamical system responses. This process is essentially a statistical pattern recognition paradigm that must come to a decision about the health of a structure by comparing data taken from the current state of the structure with data taken while the structure was in a known baseline or reference state. This comparison via statistical pattern recognition is accomplished using the following four-part process first outlined by Farrar et al.: (1) operational evaluation, (2) data acquisition, (3) feature selection and (4) statistical model development (Farrar et al. 1999).

Operational evaluation determines the conditions under which the system to be monitored functions. The first step in this assessment is to define and, to the extent possible, quantify the damage that is to be detected. Limitations on types of data that can be gathered for use during the damage detection process are also strictly defined during this stage. Operational and environmental conditions must also be identified. The SHM system that is implemented is then able to be customized to the specific requirements of the particular application

Data acquisition in a SHM process begins with the selection of the types of sensors to be used, placement and number of sensors, and the hardware used to transmit the data from the sensors into storage. Intervals at which data are taken must be explored, as the amount of data necessary depends on the specific structure as well as the type of damage to be detected.

Feature extraction involves the selection of certain information from the measured data that distinguishes between a damaged and an undamaged structure. This extraction often involves condensation of the large amount of available data into a much smaller data set that can be better analyzed in a statistical manner. Ideally, this condensed data should be as insensitive as possible operational noise and environmental effects while maintaining desired sensitivity to the damage to be detected.

Statistical model development is the area of SHM that is least developed to date. Very few of the available SHM techniques have incorporated algorithms that analyze the extracted features from the data and unambiguously determine the damage state of the structure within the typical variation that would occur on the structure, usually due to operational and environmental influences. Examination of the aforementioned features using rigorous statistical procedures should yield information that allows a diagnosis of damage state in the monitored structure. There are three general types of statistical models for SHM: (1) group classification, (2) regression analysis and (3) outlier detection (Worden and Manson 2007).

Group classification and regression analysis are used in a *supervised learning* paradigm. Supervised learning SHM paradigms have data available from the structure in undamaged (baseline) and various known damaged states as long as the structure can be reversibly tested for damage (e.g. bolted connections) or there are physical samples with various defect levels available for testing. Alternatively, high-fidelity physics-based models can also be used to simulate the structure in different known damage states, provided the models have been independently validated in some way. Group classification involves a decision placing the current state of the structure into one of a discrete number of states that have been previously described through experiments or modeling. Regression analysis is used in cases where a continuous quantification of structural condition is required, such as length of a crack. Outlier detection is an *unsupervised learning* technique. In unsupervised learning no data are available except that gathered from the structure in its current state. Statistical models are then employed to detect when an extracted feature has undergone a statistically significant change (a statistical outlier has been produced) to determine whether damage has occurred.

There are five levels of damage state evaluation that are possible for any given system and each level provides greater knowledge of the damage but is also more difficult to ascertain. These five levels were first described by Rytter as: (1) damage existence, (2) damage location, (3) damage type, (4) extent of damage and (5) prediction of the amount of useful life left in a structure, or prognosis (Rytter 1993). Supervised learning SHM paradigms may be able to identify all five levels of damage state evaluation. Unsupervised learning is likely only able to identify damage existence and location.

This dissertation will implement the aforementioned statistical pattern recognition paradigm (including both supervised and unsupervised learning techniques) on a number of applications. Bolted connections between metal structural components and adhesively-bonded connections between composite structural components are examined. These connections are commonly found in many civil, aerospace and maritime structures.

1.3 History of SHM for bolted and bonded connections

Many currently employed vibration-based SHM methods use low frequency broadband excitation as input to an examined structure. These methods are able to perceive the existence of incipient damage, but are mostly unable to identify the precise location(s) of damage within the structure because only global dynamical behavior is excited (Doebling et al. 1996; Doebling et al. 1998). The most prevalent method currently employed in practical field applications for damage location identification in structural joints is ultrasonic testing, especially in the aerospace industry (Guyott et al. 1986). These ultrasonic waves have proven to be a useful tool for damage detection and localization because of the small length and time scales on which they operate. One such conventional ultrasonic bond inspection technique is known as the Fokker bond method. This ultrasonic inspection is executed in ground tests of aircraft and consists of measuring the frequency-dependent reflection coefficients of ultrasonic waves propagating through the bonded or jointed sub-structure in the megahertz frequency range (Guyott and Cawley, 1988). This technique has been successfully implemented for some time, but it has several limitations that cause continuous *in situ* SHM to be infeasible. It is inherently an off-line technique, requires bulky test equipment and an expert technical operator, and has a very limited spatial inspection range.

This problem of damage localization for *in situ* health monitoring has recently been addressed using *guided* ultrasonic waves (Alleyne et al. 1996; Wilcox et al. 1999). These guided waves are suitable for continuous monitoring because relatively few actuators/sensors need to be used by exploiting the waveguide geometry of the structure (plates, rails, bars, etc.). While some work has been done using guided waves created with air-coupled transducers (Castaings et al. 1996; Tuzzeo and Lanza di Scalea 2001) or laser vibrometry (Staszewski et al. 2004), these methods are difficult to implement for continuous health monitoring. Most researchers have turned to the use of piezoelectric actuators/sensors as an effective means of *in situ* ultrasonic damage detection (Giurgiutiu and Zagrai 2002; Wait et al. 2004; Giurgiutiu 2005). Some of the most frequently employed SHM methods that use actively created guided ultrasonic waves to interrogate adhesively bonded joints involve the examination of dispersion curves and attenuation coefficients (Xu et al. 1990; Pilarski and Rose 1992; Seifried et al. 2002) as well as reflection and transmission characteristics (Rokhlin 1991; Lowe and Cawley 1994). Many of these methods also apply the use of denoising and wavelet transforms to increase signal-to-noise ratio and to selectively examine individual mode propagation of sensed waveforms (Abbate et al. 1997; Lanza di Scalea et al. 2004). These techniques are well established and can work in certain structures with simple geometries (plates, beams, etc.) or on sections with constant cross-section properties in the wave propagation direction (rails). However, these methods cannot easily be applied to irregular geometries, such as bolted joints, because of mode conversion and wave interference effects that arise as a result of complex interfaces and mechanical impedance mismatches across the joint. Instead, some researchers have attempted to employ bulk insonification, where an ultrasonic source is excited and the resultant long-time, or diffuse, wave field is recorded (Michaels and Michaels 2005). Statistical pattern recognition features can then be used to examine the recorded wave field and identify structural changes. This method is preferable to the standard guided wave method for structures with complex boundary conditions or geometries that make tracking and analysis of a single propagating mode difficult or impossible. For an overview of the ultrasonic health monitoring paradigm see Figure 1.1.

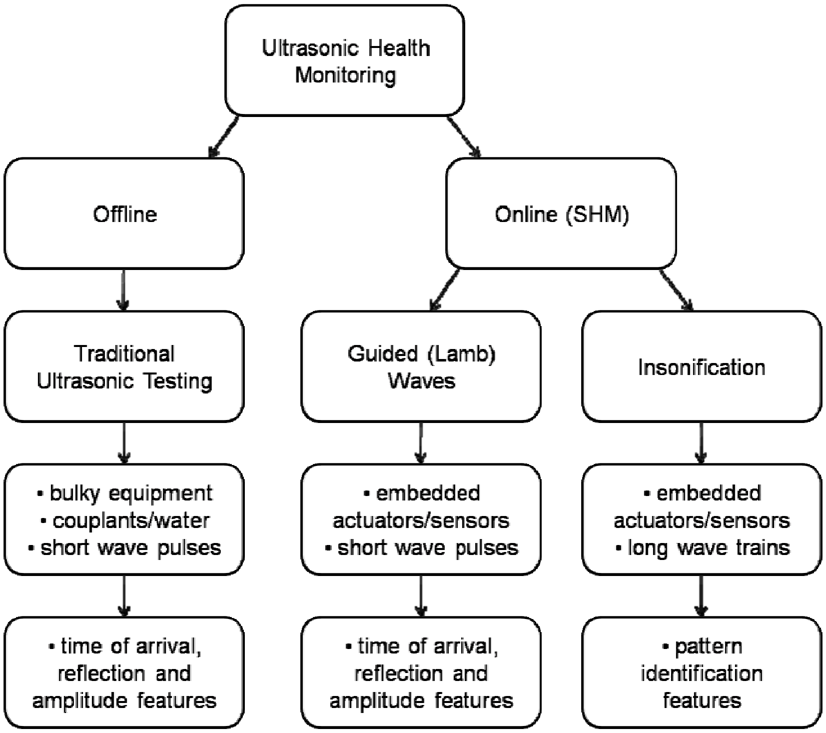

Figure 1.1. Ultrasonic health monitoring paradigm

As a means of addressing the shortcomings of current guided ultrasonic wave health monitoring techniques, this dissertation employs a class of statistical pattern recognition algorithms originally developed in the vibration (lower-frequency acoustic) domain that are based on state space analyses using auto- or cross-prediction methods. These methods employ chaotic excitations and attractor-based prediction error algorithms and have demonstrated the capacity to detect bolt preload loss in various test bed structures with enhanced sensitivity over traditional vibration-domain analyses (Nichols et al. 2003; Todd, Erickson et al. 2004). Unfortunately, these chaotic excitations are also low frequency in nature and are therefore unable to localize damage within a structure. This dissertation uses the benefits of combining ultrasonic guided waves (small length and time scales) with chaotic excitations (which enable and enhance pattern recognition techniques) for damage detection of bolted and adhesively-bonded connections via bulk insonification. This synthesis of techniques is accomplished by shifting the energy of a low-frequency chaotic process, such as the common Lorenz signal, into the ultrasonic frequency range (>20 kHz) and launching it into the structure as a guided wave. These chaotic ultrasonic waves (CUWs) are imparted to a structure by a particular kind of piezoelectric actuator known as a Macro Fiber Composite (MFC) patch and do not require a large energy input into the system. An MFC patch is also used to acquire the vibration response in an active sensing manner. A schematic of an MFC patch can be seen in Figure 1.2. The combination of chaotic ultrasonic excitation and attractor-based prediction error metrics, which require no knowledge of structural geometry, results in a procedure that can be used for *in situ* health monitoring. Such a damage identification scheme can potentially provide significant economic and life-safety benefits by preventing unforeseen catastrophic failures.

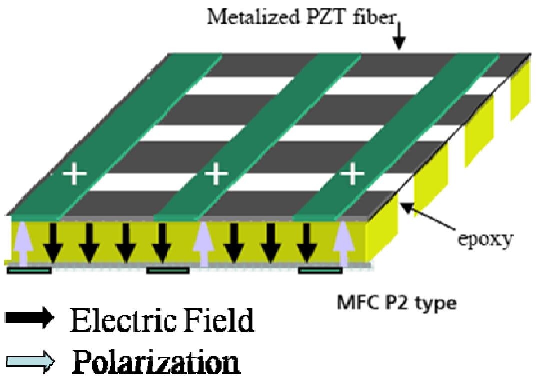

Figure 1.2. Macro fiber composite (MFC) patch schematic

1.4 Dissertation scope

Section 2 details the creation process of the chaotic ultrasonic waves that are used as excitation sources throughout this dissertation. Several signal creation parameters are introduced and their effects on signal characteristics such as power spectral density are detailed. A study of the embedding dimension of chaotic ultrasonic signals (through the creation and data acquisition processes) is also presented. The concepts of state-space embedding and attractor reconstruction are introduced as a means to estimate embedding dimension. A low signal dimension is vital to the efficacy of damage detection methods detailed in Section 3, as low dimensional signals provide reduced processing and storage requirements and increased ability of the system to resolve damage via statistically robust computation of features.

Section 3 describes the feature extraction via data-driven predictive models that are employed in this dissertation. A prediction error model based on attractor reconstruction and state-space embedding is introduced as a means of damage detection. Auto-regressive (AR) time series models that are used in the dissertation are also detailed here and their application to a novel *group classification* scheme is discussed. These damage-sensitive features are demonstrated on a variety of structural connections, including bolted metal connections and adhesively-bonded composite connections. Bolted connections are especially suitable for damage classification studies because damage levels are both controllable and reversible.

Section 4 provides an overview of several experimental platforms on which the state-space prediction error feature is employed in this dissertation. One test structure examined is an aluminum portal structure with bolted angular connections in which damage is induced by reduction of bolt preload. A second test structure is a large aluminum plate that is damaged via corrosion. Subsequent comparison of state-space prediction error feature performance to AR model based performance show that the added computational complexity of the state-space method does not improve detection performance over a much simpler AR model.

Section 5 then details several new experiments that were performed using a *group classification* algorithm based on the use of AR model coefficient vectors as damage discriminators. Single-bolt lap joints and multiple-bolt frame structures are examined using a subset of this classification algorithm. Several experiments involving composite wing-to-spar bonded joints are then conducted and employ the full classification algorithm. In these composite bonded structures damage is created by inserting various sizes of Teflon into the bond region before bonding to simulate disbond conditions. These experiments examine the effect of changing chaotic ultrasonic excitation creation parameters on structural assessment as well as the effects of temperature variability, within-unit variability and unit-to-unit variability on the outlined classification scheme.

Section 6 concludes the dissertation with a summary of results and a discussion of open research questions and further work that can be undertaken to explore these issues.

This dissertation contributes to the SHM body of knowledge by introducing a new class of ultrasonic excitation signals, an overall methodology for performing the damage detection problem and demonstrating its effectiveness on a number of challenging applications for which standard ultrasonic techniques are difficult to implement. The use of bulk chaotic insonification techniques instead of traditional single guided mode tracking allows this damage classification scheme to be employed on a greater number of real-world structures because complex (e.g. bolted, angular) connections do not negatively affect the discrimination ability of the proposed SHM pattern recognition algorithm.

2 CHAOTIC ULTRASONIC WAVES

SHM systems require sufficient excitation to excite the structure to the extent that changes in the dynamic behavior of the structure can be identified and attributed to a change in structural integrity. There are two methods of setting up a sensor network on a structure for SHM: *passive sensing* and *active sensing*. *Passive sensing* uses existing inputs to a structure (such as cars driving over a bridge or wind blowing against a building) as the only input to the structure. This method of sensing is usually unable to detect small levels of damage because the energy exciting the system is too small to effectively change the system dynamics. In *active sensing* an excitation is applied to the structure for the specific purpose of structural state identification. In the vibration domain this excitation is usually supplied via an electro-magnetic shaker. In the ultrasonic domain most research has used piezoelectric devices to excite the system, although as previously mentioned laser vibrometry and air-coupled transducers are also used. *Active sensing* has several advantages over *passive sensing* including the ability to supply user-prescribed excitations to the system to elicit specific dynamic responses expected to be sensitive to damage-induced changes and the ability to tailor those excitations for specific damage type classification and for specific pattern recognition techniques. This dissertation employs *active sensing* techniques using specially tailored ultrasonic waves, specifically ultrasonic waves that are chaotically modulated in order to enhance pattern recognition algorithm effectiveness.

Chaos arises in the dynamics of certain nonlinear systems that are distinguished by extreme sensitivity to initial conditions (Abarbanel 1996). Small changes, or perturbations, to the initial state of a chaotic nonlinear system exponentially diverge and can result in very different steady state dynamics. Nonlinear systems, even in the chaotic regime, are deterministic. This means that for a given initial condition, the dynamics evolve in exactly the same way for a given input.

The chaotic *ultrasonic* signals used in this dissertation are fundamentally created via amplitude modulation, i.e., by multiplying a single ultrasonic frequency tone by an amplitude envelope that is created by a chaotic process. The waveform appears as a narrowband, chaotically-modulated signal centered at the same central frequency as the original ultrasonic tone. A chaotic waveform is able to enhance prediction error based damage detection features because the signal is deterministic, and because of the phase space diversity associated with the chaos. The deterministic aspect of chaotic inputs was used in the context of SHM by Todd et al. when they showed that an attractor-based detection feature had superior performance to modal-based features at detecting loss of stiffness in a computational spring-mass system when excited by a chaotic waveform (Todd et al. 2001). A number of studies involving chaotic excitation were then completed in the following years (Trickey et al. 2002; Nichols et al. 2003; Nichols, Todd, and Wait 2003; Moniz et al. 2004; Nichols et al. 2004). There are also a large number of state-space features that can be employed for damage detection that do not necessarily use chaotic excitation. These state-space features will be further discussed in Section 2.2. It is clear, however, that chaotic excitations can be used effectively for SHM applications. This dissertation seeks to use the effectiveness of chaotic excitation for damage detection in the ultrasonic regime and therefore a method for creating chaotic ultrasonic signals must be detailed.

2.1 Chaotic ultrasonic signal creation

A chaotic ultrasonic waveform y_n is created by simple amplitude modulation of an ultrasonic carrier as detailed in the following Eq. (2.1);

$$y_n = \sin(2\pi n f_c / f_s) \cdot (1 + d \cdot x_n) \tag{2.1}$$

where y_n is the modulated waveform, f_s is the sampling frequency (the hardware used in this dissertation samples maximally at 4 MHz for a high-fidelity waveform), f_c is the desired carrier frequency (typically, in the hundreds of kHz in the applications in this dissertation), d is the modulation depth, and x_n is a chaotic waveform produced by a separate chaotic process. Thus, the waveform x_n appears as a narrowband, chaotically-modulated signal centered at the desired central carrier frequency, f_c, or a chaotic ultrasonic wave (CUW). In this work, the chaotic process was obtained as the x_1 output of the well-known Lorenz system

$$\begin{aligned} \dot{x}_1 &= 10(x_2 - x_1) \\ \dot{x}_2 &= (-x_1 x_3 + 28x_1 - x_2) \\ \dot{x}_3 &= (x_1 x_2 - 8x_3 / 3) \end{aligned} \tag{2.2}$$

There is nothing unique about the Lorenz system for generating chaotic output; any system capable of producing a chaotic output is suitable, but the Lorenz system shown in Eq. (2.2) has a robust parameter region for producing chaotic output and was selected for this study. Eq. (2.2) is integrated using a time-step R/f_s, where R is a frequency ratio that can be modified to change the fundamental time scales of the chaotic signal. This dissertation uses several values of R that affect the frequency regime in which the power of the chaotic signal lies. This chaotic signal is normalized through division by the maximum of the absolute value of the signal so that the values range from -1 to 1. The modulation depth d controls signal bandwidth, and if it is greater than one, the resulting signal will be over-modulated and will result in a phase inversion at the points where $|d*x_n|>1$. These phase inversions would be detrimental to any prediction algorithm, and d is therefore restricted to the range $0<d\leq1$. Figure 2.1 shows the effect of changing the frequency ratio R and the modulation depth d on the time series and power spectral density of the interrogating wave.

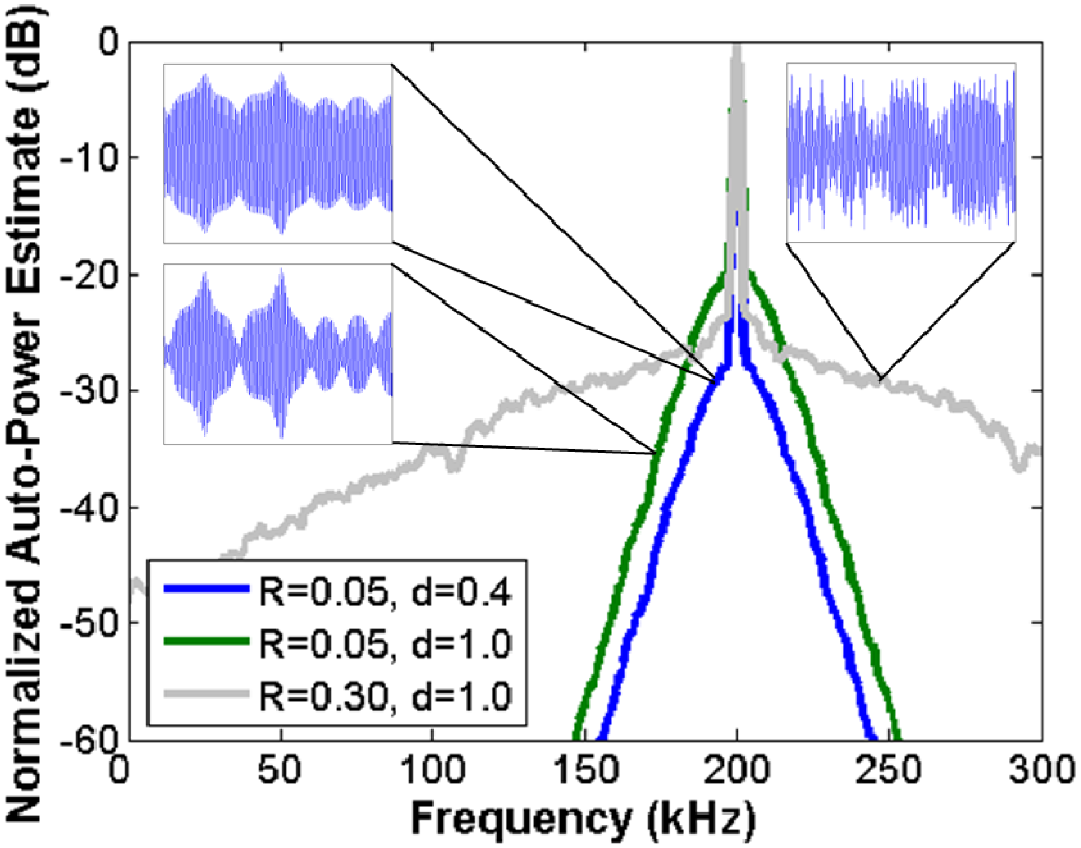

Figure 2.1. Modulated chaotic signal power spectral density and time series using *R* = 0.05 and *d* = 0.4 (upper left), *R* = 0.05 and *d* = 1.0 (mid left) and *R* = 0.30 and *d* = 1.0 (upper right).

2.2 Dimensionality of chaotic ultrasonic signals

Recently, methods based on state-space analysis (of reconstructed dynamic responses) have been used as a means of change detection in SHM applications. In short, geometric objects that are akin to the true state-space attractors of the chaotic waveform are reconstructed by embedding time-delayed copies of the original time series into higher dimensions to create a pseudo-attractor in state-space from which various correlation or prediction metrics may be computed to facilitate the feature extraction part of the pattern recognition paradigm. Features that have been developed for state-space analysis in general include correlation dimension (Grassberger and Procaccia 1983; Logan and Mathew 1996), dynamic continuity (Pecora et al. 1997), nonlinear prediction error (Schreiber 1997), generalized interdependence (Arnhold et al. 1999), time scale separation (Cusumano and Chatterjee 2000), Lyapunov exponents (Trendafilova and Van Brussel 2001), local attractor variance ratio (Todd et al. 2001), parameter drift (Chaterjee et al. 2002), attractor dimension (Nichols et al. 2003) and phase space warping (Chelidze and Cusumano 2004). The idea is that these features may be compared between baseline and test cases to determine how the system response has evolved due to damage.

A critical issue when employing such state-space embedology methods is the embedding dimension choice that will be used in the pseudo-attractor reconstruction (Sauer et al. 1991). Every orbit in a multivariate space has a characteristic fractional dimension that describes the way in which the number of points within a sphere of radius r scales as the radius shrinks to zero. There are various methods for determining the fractional dimension of a signal (Abarbanel 1996). The reconstruction theorem states that at a minimum the embedding dimension must be at least twice the fractional dimension of a signal to ensure that the signal is completely unfolded in state-space and will behave dynamically similar to the true system. However, this is an upper bound to the choice of embedding dimension, and it is usually possible to embed in a smaller dimension than this sufficient criterion dictates.

In SHM applications, it is desirable to keep the embedding dimension as low as possible to maintain damage detection resolution (statistically, many observations of low-dimensional features are superior to fewer observations of high-dimension features for classification problems) and to reduce computational demands, where appropriate. A low embedding dimension is especially necessary if these attractor-based methods are to be employed in real-time monitoring systems, given the processing efforts required to execute them, e.g. nearest neighbors searching. In active sensing, where the interrogating ultrasonic waveform is prescribed with a certain dimension associated with the chaotic process used to create it, the signal is processed and received through various data acquisition and filtering components that themselves can be considered dynamic systems. It is known that these actions can affect the dimension of a process (Pecora and Carroll 1996). Therefore, a dimensionality study is undertaken to examine the possible effects that a standard data acquisition (DAQ) process has on signal dimension through the launching process. The expected filtering due to waveform interaction with the structure itself may very well cause dimension increase as well, but undesired additional dimensional increase due to the DAQ, conditioning, or signal generation steps must be minimized for optimal efficacy of the overall approach.

2.2.1 Attractor reconstruction

Attractor-based methods perform pattern recognition algorithms on state-space attractors that are dynamically similar to the true system. Complete reconstruction of the true state space attractor is often not possible because all of the state space variables are not able to be directly measured. However, Takens has shown that a state space attractor that maintains all the dynamic invariants of the true state space can be reconstructed by forming delayed copies of a single state space variable, e.g. acceleration (Takens 1981). This reconstruction can be shown in the following form:

$$X(n) = \begin{Bmatrix} x(n) \\ x(n+T) \\ \vdots \\ x(n+(m-1)T) \end{Bmatrix} \tag{2.3}$$

The *m* pseudo-state vectors are delayed versions of the original signal with a time delay of *T*. Appropriate choices of embedding dimension *m* and time delay *T* will preserve the dynamics of the true state space. Care must be taken in estimating these parameters in order to form a reconstructed attractor that is most similar to the true attractor. For example, if the chosen time delay is too small the information in succeeding pseudo-state vectors will be highly correlated and contain a large amount of redundant information. However, if too large a time delay is chosen the coordinates in the state space reconstruction will become essentially uncorrelated and will not preserve the dynamics of the true system. Similarly, if too small an embedding dimension is chosen there will be false projections from higher dimensions onto the lower dimensions. For instance, if a simple sine wave is properly embedded in two dimensions it will appear as a circle in state space, whereas if it is only embedded in one dimension the state space reconstruction will appear as a line segment. Also, if too large an embedding dimension is chosen the extra dimensions will no longer characterize the dynamic content of the signal but will be populated by noise effects.

2.2.1.1 Optimum time delay *T*

There are two main methods for calculating the optimum time delay for proper state space reconstruction of a signal. The first method chooses the time when the first zero-crossing of the autocorrelation function occurs (Abarbanel 1996). Another approach uses the first minimum of the average mutual information (AMI) function as the time delay in order to attempt to make each dimension as orthogonal (independent) as possible (Fraser and Swinney 1986). In all the following studies the latter of the outlined approaches is used.

2.2.1.2 Proper embedding dimension *m*

Again there are several approaches that have been investigated for finding the proper embedding dimension for state space reconstruction. Broomhead and King have suggested a method that uses the singular value decomposition (SVD) of the signal as a basis for estimating embedding dimension (Broomhead and King 1986). This method has certain requirements on sampling time and bandwidth that must be considered before using, so this study employs a more versatile method proposed by Kennel and Abarbanel known as the false nearest neighbor (FNN) method that does not have stringent usage requirements (Kennel and Abarbanel 1992). To implement this technique the optimum time delay must already have been chosen using one of the previously mentioned methods. The FNN algorithm then embeds the data for m=1 and m=2. A nearest neighbor in Euclidian space is then calculated for each data point in the m=1 case. If one of these nearest neighbors is no longer the nearest neighbor for the m=2 case it is considered a false nearest neighbor. By summing up all the FNN and dividing by the total number of points, a percentage FNN for dimension m=1 is found. The FNN algorithm then embeds the data for m=2 and m=3 and repeats the outlined procedure. In this manner a percentage of FNN for each embedding dimension m is recorded. When this percentage falls below a threshold level, say 2%, or levels off for increasing m, it is concluded that the attractor has been sufficiently unfolded and the embedding dimension is chosen accordingly.

2.2.2 Digital filters

One of the most basic operations in digital signal processing (DSP) is the application of a filter to a discrete signal. There are two major categories of digital filters: finite impulse response (FIR) filters and infinite impulse response (IIR) filters. IIR filters are recursive, meaning they require knowledge of the prior output of the filter as well as present and past input to the filter. An IIR filter can be represented using the following equation:

$$y(n) = \sum_{k=0}^{N} b_k x(n-k) - \sum_{k=1}^{M} a_k y(n-k) \tag{2.4}$$

FIR filters are non-recursive, meaning they require no knowledge of the output of the filter at previous time steps. An Nth order FIR filter can be represented using the following equation:

$$y(n) = \sum_{k=0}^{N-1} b_k x(n-k) \tag{2.5}$$

It is clear that if the a_k coefficients are set to zero in the IIR filter Eq. (2.4) that it reduces to the FIR filter in Eq. (2.5).

2.2.2.1 Effects of digital filters on embedding dimension

It has been shown that Takens' theorem applies to time series filtered with FIR filters, and furthermore that the FIR filter does not affect the dimension of the signal (Nichols et al. 2003; Broomhead et al. 1992). FIR filters behave in this manner because they can be characterized as a simple moving average process. Conversely, IIR filters can be characterized as a non-autonomous dynamical system. Therefore, interaction between the filter dynamics and the signal dynamics can make embedding dimension dependent upon the contraction rates associated with the filter dynamics (Badii et al. 1988). Davies and Campbell and Davies have shown that if the contraction rates associated with the filter are large enough with respect to the signal dynamics that the dimension of the attractor in the extended state space, which includes both the signal and the filter, remains unchanged (Davies and Campbell 1996; Davies 1997). Therefore, any SHM algorithm that involves digital filtering of an acquired signal must use FIR filters if a guarantee of no increase in dimension of the signal is required. If an IIR filter is used, it will be necessary to confirm that no dimension increase has occurred.

2.2.3 Typical data acquisition process

A standard DAQ process can be represented using the block diagram in Figure 2.2. The input analog signal is often first routed through an analog low pass anti-aliasing filter. This filtering process limits the power spectrum of the input signal to half of the sampling frequency (Nyquist frequency). The low pass filter is carefully applied so as not to mirror aliased spectral components into the frequency bandwidth that is to be examined. If this anti-aliasing filter is not applied correctly, there is no way in which to distinguish which part of the spectrum comes from the original input signal and which part of the spectrum is a result of the mirrored spectral components. An anti-aliasing filter with a sharp-cutoff frequency is required and can often be the most expensive part of a DAQ system. Therefore, on many less expensive DAQ cards, the sharp-cutoff filter is simply left off or converted to a more simplified anti-aliasing filter with a gradual cutoff and used in conjunction with oversampling to ensure that aliasing is not a problem.

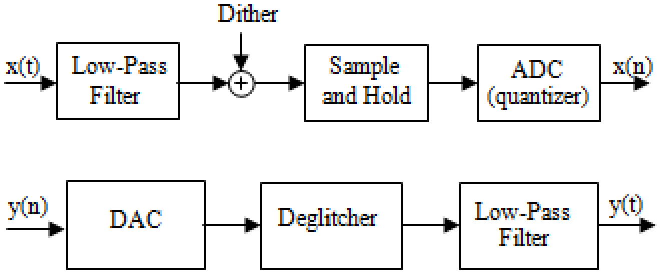

Figure 2.2. DAQ process block diagrams for analog-digital conversion (top) and digital-analog conversion (bottom).

The discrete time signal may then be subject to dithering, which adds Gaussian noise to the signal with magnitude on the order 0.5 LSB_{RMS}. This is used beneficially for applications involving averaging, such as calibration and spectral analysis. Oversampling cannot remove the quantization error that is inherent in ADC, but by combining oversampling, dithering, and averaging, the effects of quantization error can be effectively removed and the stepped nature of the signal that results from using a sample and hold circuit is eliminated. In high-speed DAQ processes that do not involve averaging or spectral analysis, it is usually a good idea to disable dithering to reduce unwanted noise.

Sampling of the analog input signal is achieved using a “sample and hold” circuit. This circuit takes the signal value at a particular sampling instant and holds it over the entire sampling period. The result is a stepped signal as is shown in Figure 2.3. This is a necessary step as the analog-to-digital converter (ADC) requires a constant value for a portion of the sampling period so that it has time to decide on the correct digital value to represent the analog voltage. The most common ADC in high-speed DAQ applications transforms the analog stepped signal from the output of the sample and hold circuit into discretely sampled digital binary values using a technique known as successive approximation. This process involves stepping through each value in the binary word from the most significant bit (MSB) to the least significant bit (LSB) to find the binary word value that most closely approximates the numerical analog value. Because only a certain number of digital values are available, depending on the length of the binary word used to describe a particular value (e.g. 12-bit or 16-bit), there is necessarily a quantization error during ADC. The effect of quantization error on dimension has been studied before, although not using this method, such as in Kumaraswamy et al. in which a mathematical relation between the performance of a vector quantizer and the intrinsic "fractal" dimension of a data set is established (Kumaraswamy et al. 2004).

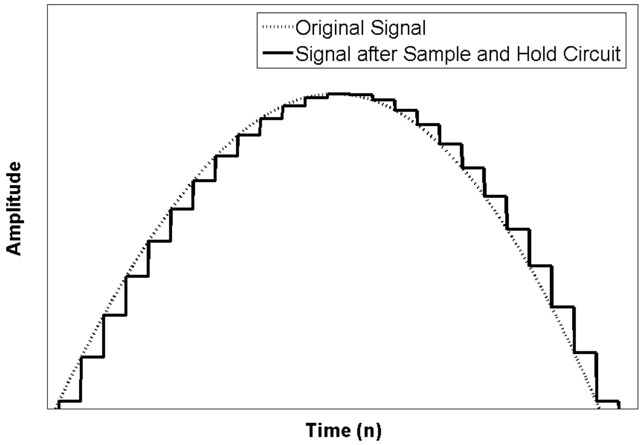

Figure 2.3. Example (idealized) output of a sample and hold circuit.

In many DAQ applications a digital signal must be converted into an analog signal, e.g. to drive an electromechanical shaker for vibration analysis of structures.

This, for example, is a key component of modulated chaotic waves for use in ultrasonic active sensing for SHM. The first step is a digital-to-analog conversion (DAC), which generates a sequence of electrical pulses at each sampling time step whose amplitude is proportional to the value of the corresponding digital samples. The most common manner in which the amplitude of these pulses is determined is to sum the currents of switched current sources with respect to an analog reference voltage and is known as a multiplying DAC. If the conversion process involves digital samples with N-bit resolution, the converter provides N current sources. For instance, if the LSB of the digital word is represented by a current I, then each succeeding source has current values of $2*I$, $4*I$, all the way up to a value of $2^{N-1}*I$ for the MSB. Current sources are then switched on or off depending on the value of the corresponding bit of the digital word. Current sources are preferred over voltage sources for this method because they have a higher achievable conversion speed.

Unfortunately, in practical implementations when a DAC switches from one voltage level to another it produces glitches in the output analog signal due to released charges. The largest glitches occur when the MSB switches values. The result is a period in which the analog output value is uncertain. To combat this problem, a circuit known as a "de-glitcher" is used to sample the output of the DAC when it has reached a stable voltage and to provide an impulse at this voltage with a well-defined length, usually the sampling period. This process is known as a zero-order hold and results in a stepped signal. It is somewhat analogous to the sample and hold circuit used in ADC.

If the stepped analog signal received from the output of the de-glitcher circuit is input into an ideal low-pass reconstruction filter, the high frequency content (steps) of the signal is removed. The low-pass filter interpolates the digital samples to reproduce the intended analog output signal. In reality, an ideal low-pass filter cannot be achieved, and the amount of effort spent trying to closely replicate the ideal filter performance depends upon the application. In applications where the best possible reconstruction of the signal is desired, oversampling techniques that allow linear-phase filtering in the digital domain (FIR filters) are often used. Again, the use of an FIR filter will not increase the dimension of the signal.

2.2.4 Data acquisition simulation

The simulated DAQ system used in this dissertation is designed to emulate the DAQ card that is being used in subsequent physical experiments, the National Instruments PCI-6036E. It does not incorporate an anti-aliasing low pass filter. Therefore, in this study, the effects of a low pass filter will not be examined. The card uses standard sample and hold circuitry and performs ADC using successive approximation and 16-bit resolution. Dithering is automatically enabled and cannot be turned off. DAC is performed using the multiplying method that is described above. No analog low pass filters are available so these effects will also not be considered.

A Lorenz chaotic signal is created using the system of equations shown in Eq. (2.2). This signal has significant frequency information from 0-10 Hz. In this study, the simulated "analog" version of the signal is discretely sampled at 50 kHz. The effect of dithering is then added to the signal by adding noise that ranges from ±0.5*LSB. The sample and hold circuit is implemented by sampling the simulated analog signal at 500 Hz. The ADC is simulated using a simple b-bit digitize function that transforms all the actual values of the signal to integers between $-2^{b-1}+1$ and 2^{b-1}. Signals are digitized using 4, 8, 12, 16, 20, and 24-bit ADC. After each step in the DAQ processes the dimension of the signal is verified using the FNN approach that is outlined in Section 2.2.1.2.

2.2.5 Simulation results

Figure 2.4 shows results of the FNN algorithm for the original "analog" signal as well as the "analog" signal plus dither for varying levels of ADC resolution. The signals corresponding to 4-bit and 8-bit ADC resolution are clearly higher dimensional than the remaining signals. This is because the amplitude of the dither added to the signal is large and, because white noise is infinite dimensional, the decreased signal-to-noise ratio (SNR) results in a higher dimensional signal. Therefore, using dither in ADC systems with low resolution without averaging is not suggested and will not be used for the remainder of this study. However, for ADC resolutions of 12-bits and above, the FNN approach cannot distinguish between the dithered and original signals. The proper embedding dimension for the original Lorenz signal is known to be m=3 which is the same result as is seen in Figure 2.4.

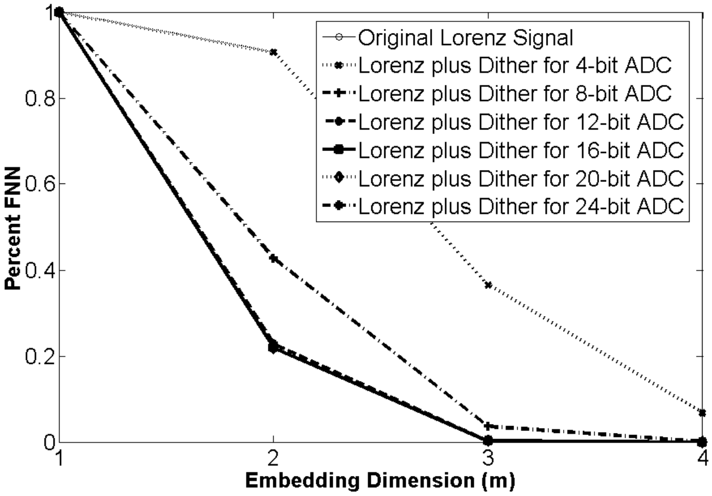

Figure 2.4. Embedding dimension after dithering for various levels of ADC resolution.

The sample and hold circuit introduces a stepped nature to the signal which can be interpreted as high frequency content at each of the discontinuities. This high frequency content has an effect similar to noise contamination and will cause the percentage of FNN to level off or even begin to increase for higher embedding dimensions. This effect can be seen in Figure 2.5. The original Lorenz signal and the dithered signals are indistinguishable after the sample and hold is performed, as one should expect since this was also the case after dither was added. For this case it is concluded that the proper embedding dimension is *m*=3 for all the signals, despite the rise in percent FNN for higher embedding dimensions. This decision is made knowing that there is some high frequency content that cannot be characterized for any embedding dimension, and so the lowest dimension that satisfactorily unfolds the original signal content is used.

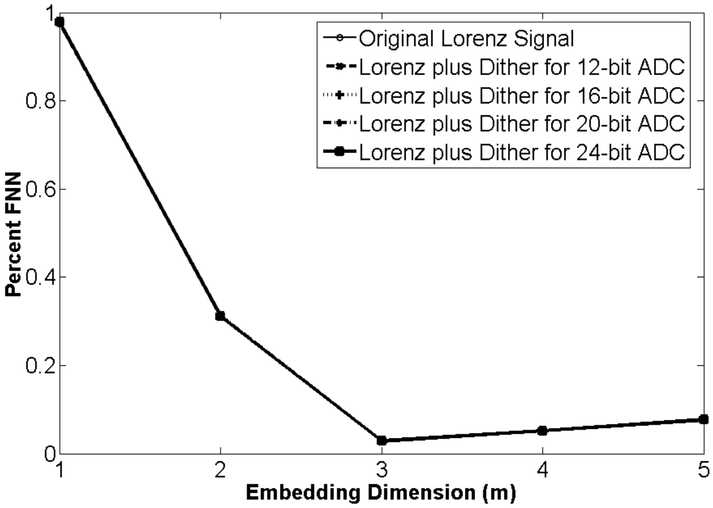

Figure 2.5. Embedding dimension after sample and hold for various levels of dither.

Figure 2.6 shows the signals after they have been put through the ADC. Clearly, using an ADC with a low resolution (4-bit, 8-bit) results in increased embedding dimension. This is a direct result of the large quantization error for these low resolution ADC systems. The discrete time signal of quantization errors is often uncorrelated in complex signals and can therefore be characterized as a white noise process. This addition of white noise to the signal reduces the SNR in much the same way as adding dither and can therefore increase the dimension of the signal. The SNR decreases by approximately 6 dB for each bit subtracted from the digital word length of the quantized samples. Thus, the SNR for a 12-bit quantizer is 24 dB higher than for an 8-bit quantizer. For ADC with a resolution of 12-bits and above, the embedding dimension remains unchanged.

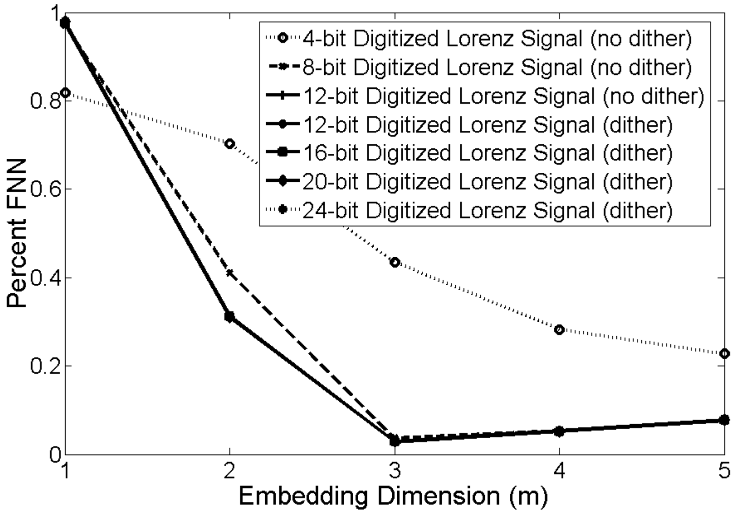

Figure 2.6. Embedding dimension after ADC for different ADC resolutions.

As can be seen below in Figure 2.7, embedding dimension increases as the frequency ratio *R* increases and the modulation depth *d* increases for a chaotic ultrasonic signal centered at 200 kHz. This result is expected because signal bandwidth rises as each of the two parameters increase, as is seen in Figure 2.1. As the bandwidth of the signal grows it differs more from a two-dimensional sine wave and becomes increasingly multi-dimensional. For chaotically amplitude-modulated signals the embedding dimension is unaffected during the DAQ process as long as the card has 12-bit precision or higher.

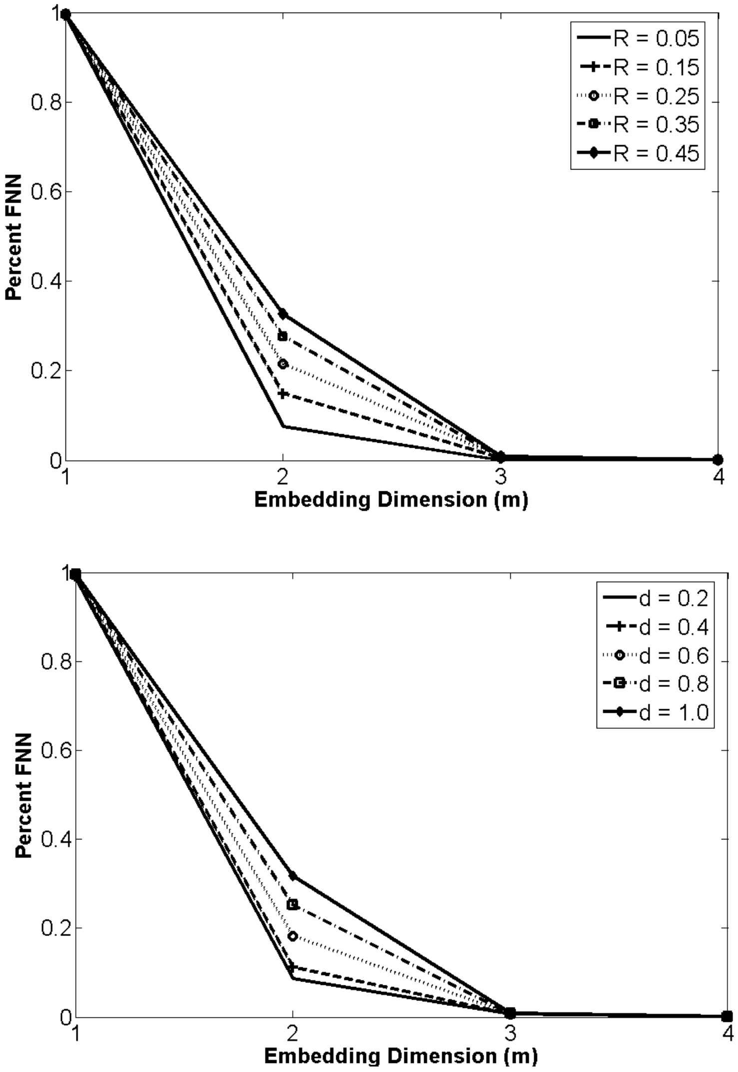

Figure 2.7. Embedding dimension of modulated signals using (a, top) *d* = 1.0 and (b, bottom) *R* = 0.25.

2.2.6 Experimental results

In order to verify simulation results that showed that there is no dimension increase using a DAQ card as the signal goes through a DAC or ADC process, a chaotic ultrasonic signal centered at 200 kHz is created and applied to the DAC on a

16-bit NI PCI-6036E DAQ card. That signal is then converted back to digital data using the DAQ card's ADC. The estimated embedding dimension of the signal that had been routed through the DAC and ADC was identical to the original signal.

2.2.7 Effect of signal-to-noise ratio

Signal-to-noise ratio (SNR) can be defined in decibel form using the following Eq. (2.6)

$$SNR(dB) = 20\log_{10}\left(\frac{A_{signal}}{A_{noise}}\right) \tag{2.6}$$

where A is the root-mean-square (RMS) value of the signal or noise amplitude. Therefore an order of magnitude increase in signal amplitude will result in the SNR rising by 20 dB. To identify the effect of SNR on signal dimension white noise is added to the standard Lorenz signal and then to a chaotic ultrasonic signal centered at 200 kHz. As can be seen in Figure 2.8, embedding dimension decreases as SNR increases. This agrees with prior observations in Section 2.2.5 made about the effect of SNR on embedding dimension.

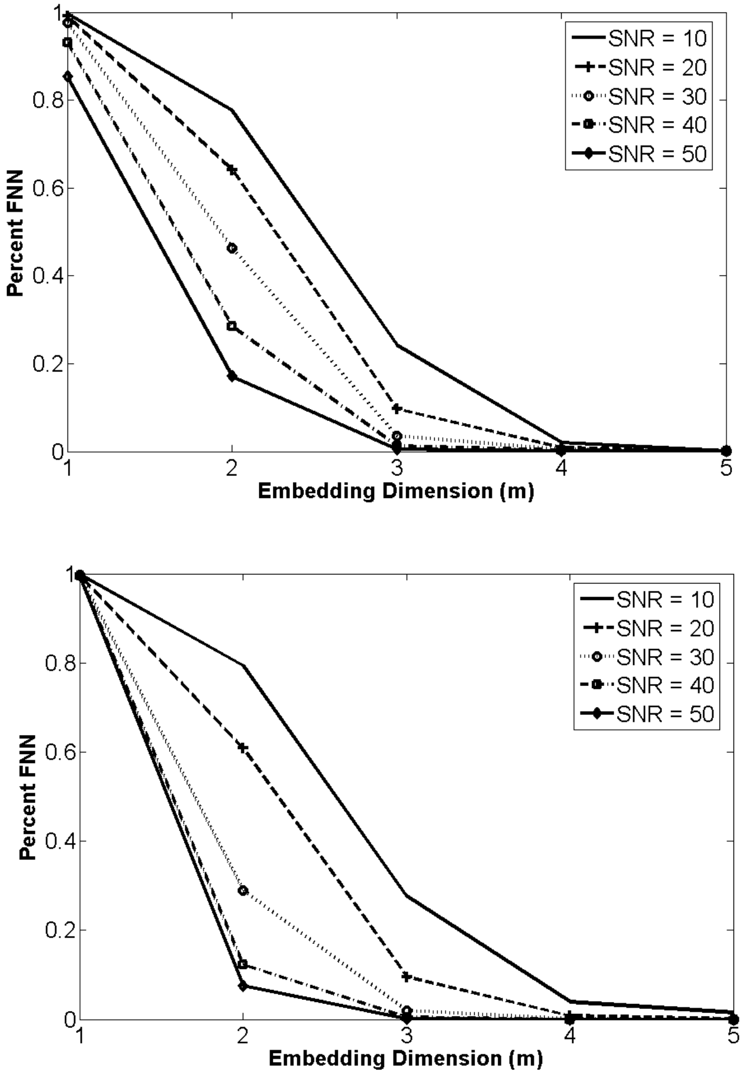

Figure 2.8. Embedding dimension of (a, top) standard Lorenz signal and (b, bottom) 200 kHz chaotic amplitude-modulated signal for various levels of SNR.

2.3 Section summary

This section outlined a method for creating chaotic amplitude-modulated ultrasonic signals. Several signal creation parameters are introduced and their effects on signal characteristics such as power spectral density are detailed. A study of the embedding dimension of chaotic ultrasonic signals (through the creation and data acquisition processes) is also presented. The concepts of state-space embedding and attractor reconstruction are introduced as a means to estimate embedding dimension. A low signal dimension is necessary to provide reduced processing and storage requirements and increase the ability of the system to resolve damage via statistically robust computation of features. It is shown that the DAQ process does not substantially alter the embedded dimension of a chaotic signal as long as the ADC/DAC resolution is at least 12-bits.

3 FEATURE EXTRACTION VIA DATA-DRIVEN PREDICTIVE MODELS

There are several damage-sensitive features used in this dissertation that are based on a statistical pattern recognition paradigm. In this section, a prediction error model based on attractor reconstruction and state-space embedding is introduced as a means of damage detection. Auto-regressive (AR) time series models that are used in the dissertation are also detailed and their application to a novel *group classification* scheme is discussed. These damage-sensitive features are derived from *data-based modeling* and not *physics-based modeling* as no knowledge of the relevant physics of a particular tested structural component is used.

3.1 State-space prediction error

The basic concept of the attractor-based prediction error method can be framed as problem in pattern recognition. A *baseline* attractor is constructed using dynamical data gathered from a structure in its baseline (presumably "undamaged") state. A *comparison* attractor is then constructed using data gathered from the structure in a future unknown state. If the structure has been damaged before the comparison set of data is acquired, the hypothesis is that the state space geometry of the comparison attractor should be different than that of the baseline attractor. Qualitatively these two attractors are simply compared using a geometric pattern recognition algorithm.

Quantitatively this comparison is achieved by tracking the time evolution of points on the baseline attractor and the time evolution of related points on the comparison attractor and then calculating the Euclidian distance between these points some s time steps into the future.

3.1.1 Prediction error model

The first step in the basic prediction error algorithm is to choose a set of F random fiducial points from the baseline attractor $X_1(n)$. These fiducial points are then related to a corresponding set of F fiducial points on the comparison attractor $X_2(n)$. This relation can be either temporal (each fiducial point chosen on the comparison attractor has the same time indices as those from the baseline attractor) or spatial (each fiducial point chosen on the comparison attractor is located at the same geometrical point in state space as those from the baseline attractor). For the following studies a temporal correlation is used. A set of P nearest neighbors to each fiducial point on the baseline and comparison attractors is then established. Points that are closely temporally related to a fiducial point are not considered nearest neighbors because the algorithm seeks to characterize the geometrical evolution in time of the particular region of the attractor surrounding the fiducial point and temporally related points would skew the results of this measurement. The points are excluded from the nearest neighbor searching algorithm through the use of a Theiler window (Theiler 1986).

The P nearest neighbors for each fiducial point on the baseline and comparison attractors are then time evolved s time steps into the future. The mass centroid of these time evolved nearest neighbors is calculated. Prediction error is then calculated as the Euclidian distance between the centroid of the comparison neighbors and the centroid of the baseline neighbors as can be seen in Eq. (3.1):

$$\gamma_{CC,f} = \left\| c_{2f}(n_f + s) - c_{1f}(n_f + s) \right\| \tag{3.1}$$

where $\gamma_{CC,f}$ is the prediction error for a particular fiducial point f that is a subset of the total number of fiducial points F, $c_{2f}(n_f+s)$ is the centroid of the neighborhood of the comparison attractor (evolved s time steps from the initial time n_f), $c_{1f}(n_f+s)$ is the centroid of the neighborhood of the baseline attractor, and s is referred to as the prediction horizon. This method is shown graphically in Figure 3.1.

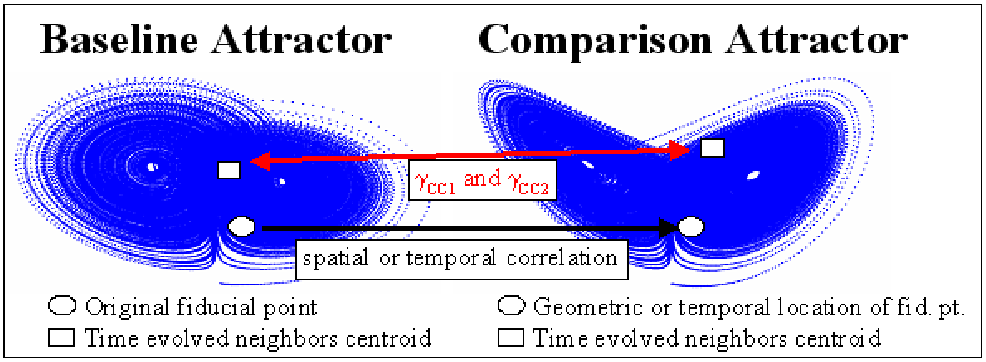

Figure 3.1. State space prediction error metric.

3.1.2 Prediction error resampling

After performing the above outlined procedure a set of prediction error metrics the size of the number of initially chosen fiducial points F is acquired. In general, the distribution of these prediction errors is unknown and may not be characterized as

Gaussian in nature. However, by using a bootstrapping technique that is based on the central limit theorem, these prediction errors can be resampled to obtain a new set of errors whose distribution tends toward Gaussian. This is done by taking a random sampling of the prediction errors (in the following studies 30% of the total number of prediction errors) and calculating the mean of these randomly sampled values. This procedure is repeated until the new set of mean prediction errors is the same size as the original number of fiducial points. These new mean prediction errors are now approximately normally distributed. Prediction errors can now be tracked as the structure is tested in future unknown states, and a significant increase in the error level will indicate that a structural change has taken place.

3.2 Auto-regressive model

Computing prediction error using the above outlined state-space method can be computationally expensive, especially for large data sets, primarily because of the neighbor-searching requirements. The full state-space method may be thought of as a generalized regression procedure, where one attractor is assumed to be spatio-temporally correlated with another attractor. A much simpler regression model class is that of the auto-regressive (AR) models which have previously been shown to be useful as a damage classifier (Sohn and Farrar 2001; Sohn et al. 2001). The discretely observed output time series $\mathbf{x}(n)$ is modeled with an AR model (e.g., an FIR filter) of the form:

$$\mathbf{x}(n) = \sum_{i=1}^{p} \alpha_i \mathbf{x}(n-i) + \mathbf{e}(n) \tag{3.2}$$

where p is the order of the AR model with associated coefficients α_i and residual error $\mathbf{e}(n)$. This dissertation examines various model orders p to determine the most suitable model order for each particular damage detection scheme. The AR coefficients are estimated through minimization of the sum-of-squared forward prediction errors (Brockwell and Davis 1991). All signals are normalized through subtraction of the mean and division by the standard deviation of the signal before use of the AR model.

3.2.1 Standard deviation of the residual error

One type of damage-sensitive feature is calculated by taking the standard deviation of the residual error time series. This particular metric is used instead of the RMS value because the standard deviation is the nearest analogue to the prediction error calculated using a spatio-temporal regression. The efficacy of this damage feature is compared to the state-space prediction error method in Section 4.2.2.

3.2.2 Damage classification scheme

Instead of using residual error derived from an AR model as a damage discriminator, calculated AR coefficients themselves can be used a damage-sensitive feature. This dissertation examines the ability of a two-part classification scheme to determine the existence and size of damage in a structure using a *supervised learning* paradigm. This classification scheme can also be employed with an *unsupervised* *learning* technique to classify whether a structural connection for which there is no baseline data (only data from a similar test structure or validated model) is damaged or undamaged. The classification approach uses features derived from an autoregressive (AR) model coefficient vector cross-assurance criterion as well a group classification scheme with its basis in information theory. Throughout this section, data from a physical experiment on several composite adhesively-bonded wing-to-spar test structures, that will be discussed in detail in Section 5.3.2, is used to illustrate the effectiveness and necessity of the two-part damage classification scheme. Two of these structures have various disbonds built into the bond line through the use of Teflon inserts and one of the structures has no damage built in. The experiment outlined in Section 5.3.2 uses the two-part supervised learning classification scheme outlined in this section to not only to classify disbond size but also to classify whether a bond for which baseline data comes from a similarly configured test structure is undamaged or has some form of disbond.

3.2.2.1 Vector consistency criterion

The first step in the damage classification algorithm is based on a comparison of AR coefficient vectors. Figure 3.2a shows averaged AR coefficients that are acquired using an AR model order of p=10 for three different bond conditions, including an undamaged bond as well as two different disbond sizes on a single adhesively-bonded composite test structure. Figure 3.2b shows averaged AR coefficients that are acquired using an AR model order of p=10 for three different undamaged bond conditions on a similarly configured test structure. The figures show a clear difference in the shape of the AR coefficient vectors for different bond conditions whereas all undamaged bond conditions result in similarly shaped AR coefficient vectors. This result suggests that a feature which compares the shape of two AR coefficient vectors will lead to a quantifiable damage-sensitive metric.

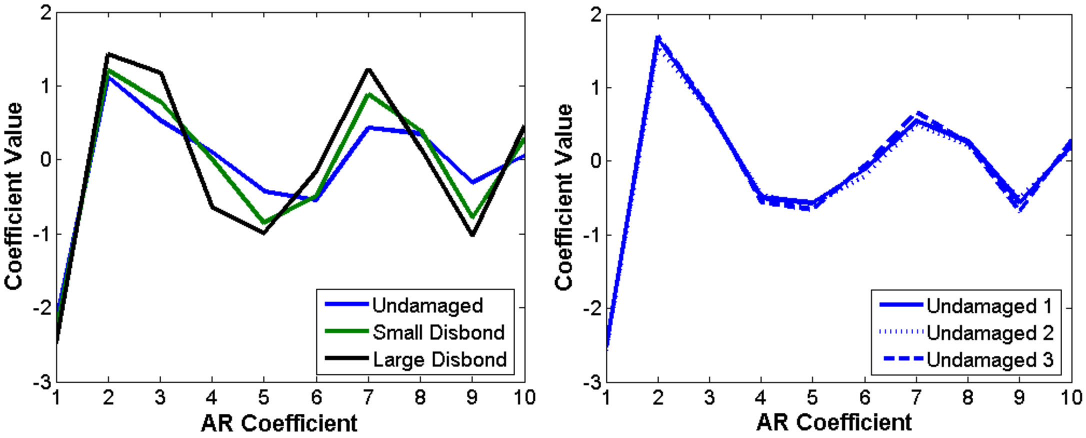

Figure 3.2. Averaged AR coefficient vector comparison for (a, left) different bond conditions and (b, right) three undamaged bond conditions.

This dissertation proposes a feature based on the modal assurance criterion (MAC) that is commonly used in modal analysis to provide a measure of consistency between estimates of a modal vector (Allemang 2003). The MAC is a normalized scalar value detailing the level of orthogonality between a test modal vector and a reference modal vector as follows:

$$MAC_{tr} = \frac{\left|\{\psi_t\}^H\{\psi_r\}\right|^2}{\{\psi_t\}^H\{\psi_t\}\{\psi_r\}^H\{\psi_r\}} \tag{3.3}$$

where ψ_t is the test modal vector, ψ_r is the reference modal vector, and H indicates the Hermitian operator or complex conjugate. The modal assurance criterion can have values ranging from zero, representing complete orthogonality, to unity, representing parallel vectors (no orthogonality). Therefore if the two vectors are consistently related (not orthogonal), then the MAC value should approach unity. This study uses a vector consistency criterion (VCC) similar to the MAC in order to measure the orthogonality of AR coefficient vectors. In this case the Hermitian operator simplifies to a vector transpose because the values of the AR coefficient vector are always real. The fact that the VCC feature can only have a value between zero and unity makes it useful as an extracted feature because scaling effects of the original signal will not affect any decision that needs to be made regarding the bond condition assessment. The hypothesis being tested is that two AR coefficient vectors should be very consistent (nearly parallel) if they are derived from modeled responses of structural connections with the same level (or lack of) damage.

3.2.2.2 Step one: damage existence classification

The determination of whether a connection of unknown condition is undamaged or damaged is accomplished using the following method.

1. Generate a set of input signals
2. Record structural responses for each input signal
    a. Twice for the undamaged condition (baseline)
    b. Once for each known damage condition
3. Estimate AR coefficients from undamaged and damaged conditions
4. Calculate distribution of VCC values
    a. Undamaged-undamaged comparison
    b. Undamaged-damaged comparison

First, a set of distinct 250-microsecond-long input signals are created from the data-generating process that has been previously described in Section 2.1. For each of these input signals a structural response is recorded once under each of the known undamaged and damaged conditions on a particular specimen, using a different actuator/sensor pair for each bond, as well as a second time for the undamaged condition. AR coefficients are then estimated for each of these structural responses using the method outlined in Section 3.2. These sets of AR coefficients form a database of structural responses for known structural conditions with each input signal that will be used to determine the condition of an unknown connection in a *supervised learning* fashion.

For the first step of the bond condition assessment algorithm, which will identify only whether an unknown connection is damaged or undamaged, a distribution of VCC values is then calculated. This is accomplished by comparing, using Eq. (3.3), each of the AR coefficient vectors from responses to the first set of waveforms to probe the undamaged connection with each of the AR coefficient vectors from responses to the second set of waveforms to probe the undamaged connection. This calculation results in a large distribution of VCC values that describe the auto-correlation between the two sets of AR coefficient vectors that are both derived from the undamaged connection condition. A new set of input signals (created from the same underlying process as the supervised learning database input signals) are then applied to the structure for a structural connection whose damage state needs to be determined. AR coefficient vectors are again calculated for each of these new structural responses. The AR coefficient vectors from the original undamaged connection condition are then compared with the new set of AR coefficient vectors from the unknown connection condition by calculating VCC values. This computation results in a second distribution of VCC values that describe the correlation between the AR coefficient vectors of the undamaged connection condition and the AR coefficient vectors of the unknown connection condition.

3.2.2.2.1 Statistical classification

A statistical measure must now be devised that can properly classify a damaged structural connection and at the same time properly classify an undamaged connection in a different geometric location using a different MFC sensor/actuator pair than the baseline undamaged connection. Figure 3.3a shows empirical probability density functions (pdfs) of VCC values for three different bond conditions, including an undamaged bond as well as two different disbond sizes from a single adhesively-bonded composite test structure. Figure 3.3b shows empirical pdfs of VCC values for three different undamaged bond conditions in different geometric locations on a different, but similarly configured, test structure. It is clear that while there are differences in the pdfs of the undamaged bonds in Figure 3.3b that the difference between the pdfs of the undamaged bond and two disbond sizes in Figure 3.3a are much greater. A statistical decision boundary that can account for the small differences in the pdfs due to geometric conditions as well as MFC bonding characteristics while still correctly classifying the damaged bonds would be beneficial.

The pdfs are not normally distributed as can be seen from the elongated left tail. Therefore, standard statistical tests that assume normality such as the Student's t-test cannot be used in this case. There are several non-parametric tests that can be employed for non-Gaussian distributions such as the Kolmogorov-Smirnov test or the Mann-Whitney U test, but for this application these tests decidedly classify the various undamaged pdfs as being from different parent distributions. A solution to this problem is to set a lower confidence limit on an undamaged pdf so that the other undamaged pdfs would not result in a significant number of outliers (VCC values less than the lower bound), but still produce a significant number of outliers for the damaged pdfs.

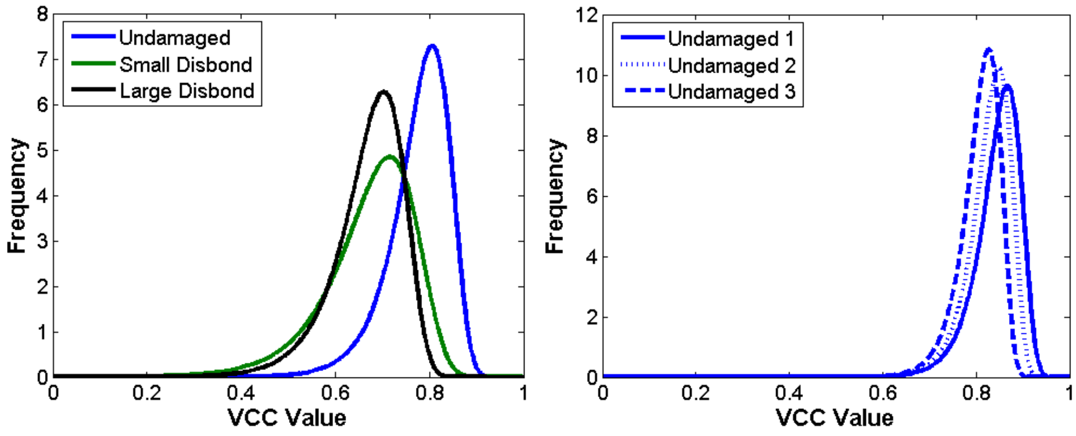

Figure 3.3. VCC value empirical pdf comparison for (a, left) different bond conditions and (b, right) three undamaged bond conditions.

3.2.2.2.2 Extreme value statistics

Extreme value statistics (EVS) are used to set the lower confidence limit on the non-normal distributions that are produced using the above outlined method. EVS is used in this analysis to accurately model the behavior of the feature distribution's tails. The basis of this branch of statistics stems from the following situation. If a moving window is taken along a vector of samples and an extremum value (minimum or maximum) is selected from each of these windows, the induced cumulative distribution function of the extrema of the samples, as the number of vector samples tends to infinity, asymptotically converges to one of three possible distributions: Gumbel, Weibull or Frechet (Castillo 1988). The following equations detail the Gumbel, Weibull and Frechet distributions for minima because that is what this study uses.

$$\text{Gumbel: } F(x) = 1 - \exp\left[-\exp\left(\frac{x-\lambda}{\delta}\right)\right] \quad -\infty < x < \infty \ \ and \ \ \delta > 0 \tag{3.4}$$

$$\text{Weibull: } \mathrm{F(x)} = \begin{cases} 0 & \text{If } x \leq \lambda \\ 1 - \exp\left[-\left(\dfrac{\mathrm{x}-\lambda}{\delta}\right)^{\beta}\right] & \text{otherwise} \end{cases} \tag{3.5}$$

$$\text{Frechet: } \mathrm{F(x)} = \begin{cases} 1 - \exp\left[-\left(\dfrac{\delta}{\lambda - \mathrm{x}}\right)^{\beta}\right] & \text{If } x \leq \lambda \\ 1 & \text{otherwise} \end{cases} \tag{3.6}$$

where λ, δ, and β are the model parameters that are estimated from the data. There are similar functions that apply to the converged distributions for the maxima of the sample sets.

The appropriate distribution is chosen by plotting the cumulative distribution function (cdf) of the extracted vector of minima on the probability paper for a Gumbel distribution (Castillo 1988). Probability paper is designed so that the cdf for a particular cumulative distribution will plot in a linear fashion by transforming the vertical scale of the plot. In this case, if the vector of minima has a Gumbel minimum distribution, the cdf will be a straight line when plotted on Gumbel probability paper. Otherwise, the cdf will have an associated curvature. If this curvature is concave, the feature vector has a Weibull minimum distribution. Similarly, if the curvature is convex the feature vector has a Frechet minimum distribution. In this study the distribution of minima taken from the parent undamaged VCC distributions has a Gumbel minimum distribution. Model parameters are then estimated by fitting the chosen distribution to the data as outlined in Castillo (Castillo 1988).

Once the model parameters are chosen, it is possible to generate confidence limits that can be applied to the distribution. These limits are more accurate than those obtained when assuming a Gaussian distribution, as long as the parent distribution is not Gaussian. The threshold corresponding to a specific confidence level for the Gumbel minimum distribution is given by the following equation (Worden et al. 2002):

$$\text{Gumbel: } x_{\min} = \lambda + \delta \ln\left[-\ln\left(1-\frac{n\alpha}{2}\right)\right] \tag{3.7}$$

where *n* is the window size used to extract the minima, and α is the associated Type I error of the confidence limit. Type I error is simply the percentage of false positives that are expected to appear. For example, when using a 95% confidence interval the Type I error is expected to be 5% ($\alpha = 0.05$). By using the confidence limit calculated through EVS the damage state classification algorithm is able to differentiate between undamaged and damaged connections. To further differentiate between different sizes, levels or types of damage a second classification scheme is used.

3.2.2.3 Step two: damage size/type classification

This dissertation uses a novel statistical classification technique with its basis in information theory to classify different sizes, levels or types of damage in structural connections. The classification method is based on a fundamental theorem of Shannon's information theory that states that "the best compression for any given data set comes from a codebook designed exactly for the statistics of that source; any other codebook will give worse results" (Shannon 1949). For instance, if one has a codebook (e.g. taking language elements like words into shorter codes) consisting of English words and another consisting of French words etc., then a new time series of letters can be represented in the shortest compressed format when using the English codebook versus all others if the new text is, in fact, written in English. Compression performance is the classic text categorization methodology. Recently, information theory has been applied to continuous time signals, where compression performance is related to prediction error, and a codebook is the model for a source that produces time series data. In this study the source is a chaotically-modulated ultrasonic wave propagating through a structural connection. These time series can then be classified using prediction error as a means of virtual data compression (via the AR coefficient vectors). This idea leads to a procedure for classifying time series using cross-prediction error as literal "data compression" in the sense that maximal information recovery on decompression is not actually necessary, just its “virtual” performance as a representative data model. The model for the response time series is the same auto-regressive model used for the undamaged/damaged discrimination that has already taken place. Of course, the better the underlying statistical model is the more the classification performance will improve.

The entire damage state classification technique can be summarized as follows. The same database of AR coefficients that was created using a set of chaotic ultrasonic guided waves is again used to decide the state of the damaged connection. In this case only AR coefficients from the damaged paths are used because it is now known that the test path has some form of damage after using the first classification technique. A new input signal (created from the same underlying process as the training database input signals) is then applied to the structure along the known damaged bond condition path. One of the sets of AR coefficients in the training database for each of the paths with disbond damage is then used to estimate the structural response to the new input signal. One set of coefficients from the training database will minimize the sum of the squared residual errors and these coefficients are associated with a known size, level or type of damage in the training database. This damage state is then classified as the state of the unknown connection that is being probed (a “vote” for classification of a particular damage state). This comparison takes place for each of the remaining input signals in the training database. This entire process is then repeated using a large set of input signals that are imparted to the structure in its unknown damage state (the same data as was used in the first classification step). The votes for each damage state are then summed and the plurality of votes is the estimated condition of the bond. The entire two-part statistical damage state classification paradigm is depicted visually in Figure 3.4.

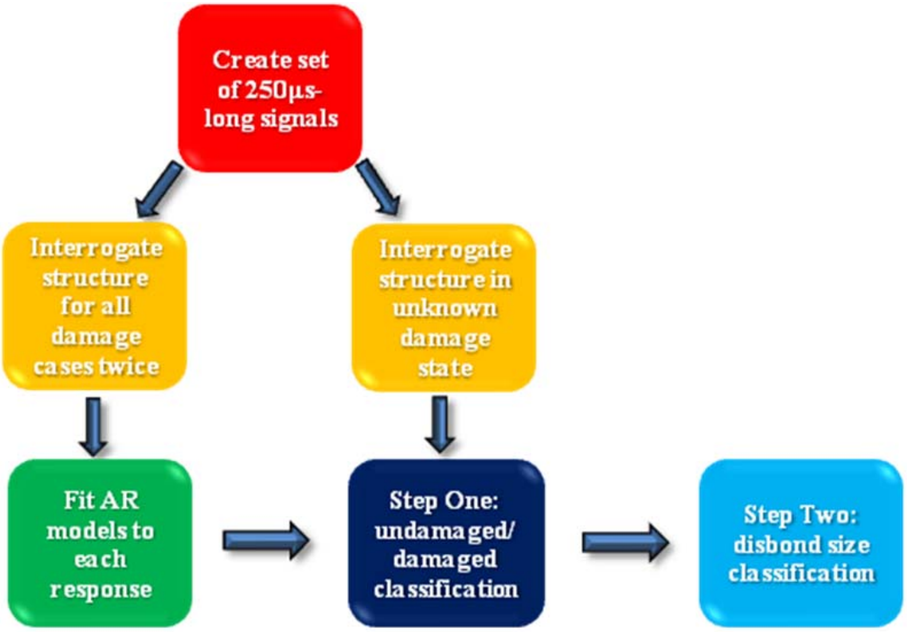

Figure 3.4. Ultrasonic statistical classification paradigm.

3.3 Section summary

This section introduced several damage-sensitive feature extraction algorithms that will be applied to physical experiments in the following sections of the dissertation. Section 4 details initial studies on bolted connections and corrosion in a plate that are performed using the state-space prediction error feature outlined in Section 3.1. The AR model-based classification schemes introduced in Section 3.2.2.2

and Section 3.2.2.3 are applied to both bolted connections and adhesively-bonded composite connections in Section 5.

4 STATE-SPACE PREDICTION ERROR APPLICATIONS

The following experiments all employ the state-space prediction error feature described in Section 3.1. Section 4.1 shows that the state-space prediction error feature, along with a modified chaotic burst excitation signal (1 MHz frequency over a very short time period), is able to locate and identify the size of corrosion damage in an aluminum plate. Section 4.2 applies this state-space prediction error algorithm to an aluminum portal structure with bolted angular connections. This method is effective at identifying incipient levels of bolt preload loss. Section 4.2.2 then shows that the AR model-based damage feature described in Section 3.2.1 has comparable damage identification capability to the state-space prediction error, but at a much-reduced processing power, making it more apt for embedded SHM applications.

4.1 Corrosion detection in a metal plate

In this study, an experiment is undertaken using an aluminum plate with an array of piezoceramic patches bonded to one side. Damage is initiated through the process of electrolytic corrosion. The previously outlined spatio-temporal prediction error algorithm is used to determine the existence, location, and extent of damage. The actuation signal that is used in this experiment was created using the procedure outlined in Section 2.1 with a center frequency of 1 MHz and is sampled at a rate of 25 MHz. A 40 microsecond portion of this signal is then taken and multiplied by a Hanning window to create a burst-type signal. This very short signal is then zeropadded with 2048 pretrigger points that are later used to remove DC offset from the signal and enough zeros are added to the end of the signal so that the entire signal length is one millisecond. Figure 4.1 shows the entire signal as well as a close-up of the 40 microsecond burst portion of the signal as it exits the amplifier.

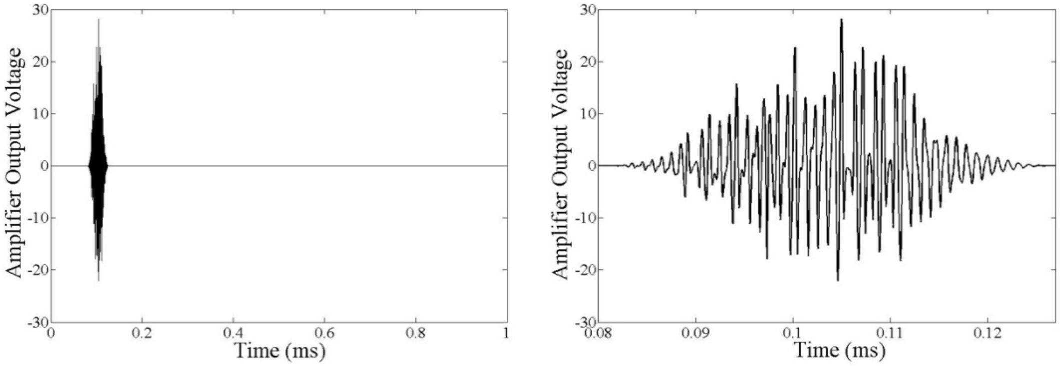

Figure 4.1. Excitation signal used for corrosion in a metal plate experiment.

Testing is performed on a 1.2m x 1.2m x 1.6mm (4ft x 4ft x 0.0625in) plate made of aluminum 6061-T6. During testing the plate is suspended above the ground in a free-free orientation using wire and surgical tubing. Nine piezoceramic (PZT) patches of radius 3 mm (0.125 in) were attached to the plate using cyanoacrylate with a grid spacing of 30 cm (12 in). Wires from each piezoceramic patch were routed into a National Instruments (NI) PXI-2527 multiplexer set up in dual 16x1 2-wire mode. This multiplexing is done so that both the actuator and sensor patch can be quickly specified through switching software instead of hardwiring the particular pair for each test. The excitation signal specified above is sent from a NI PXI-5412 signal generator at a rate of 25 MS/s with 14-bit resolution with a voltage range of ±9 V. This signal is sent through a Krohn-Hite 7602 wideband power amplifier and exits with the above pictured voltage range of approximately ±28 V. The multiplexer routs this amplified signal to the appropriate piezoceramic patch and the ensuing response is received at a given sensing piezoceramic patch. This sensed signal then goes through the multiplexer to a NI PXI-5122 high speed digitizer that also samples at 25 MS/s with 14-bit resolution. This process is repeated for all possible sensor paths with the multiplexer switching, synchronization, and data acquisition being controlled by a custom created LabVIEW virtual instrument file. This experimental setup and the layout of the nine piezoceramic actuators can be seen in Figure 4.2.

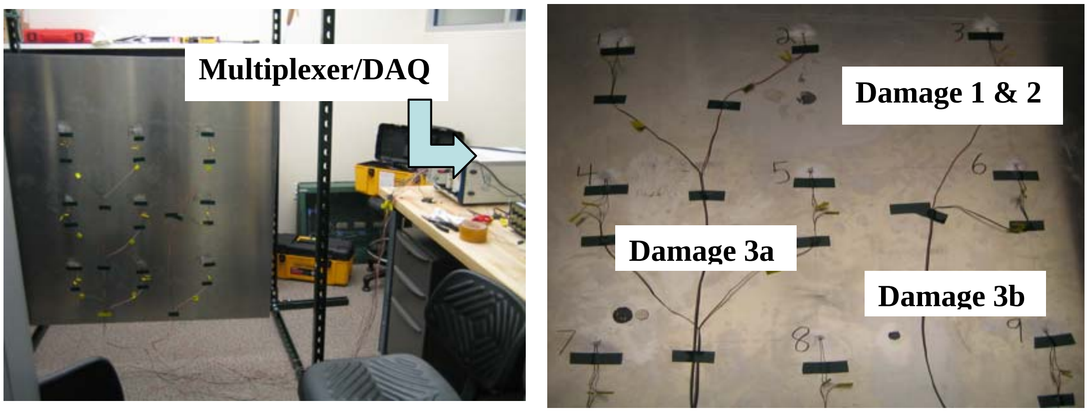

Figure 4.2. Corrosion in a metal plate experimental setup.

Each sensor signal is averaged 10 times and only the first 1500 points (60 microseconds) of the recorded wave packet is kept. Only 1500 points are kept so that, to the degree it is possible, only the direct path between the actuator/sensor pair is interrogated. If more points were kept the signal would contain more reflections from indirect paths. This process is then repeated 100 times with successive records added to the end of the last one so that a total record length of 150,000 points is achieved. Each record is broken up into 4 runs of length 37,500 points. The signal is extended and split up into runs in order to form more robust statistical features. All runs are normalized by subtracting the mean and dividing by standard deviation before embedding in order to remove any possible environmental variation from the signal. The number of fiducial points used for each prediction error algorithm is 10% of the total number of points, or 3,750. The number of nearest neighbors used to calculate the mass centroid is 0.1% of the total number of points, or 37.

Table 4.1: Actuator/sensor pairs for each interrogated path length.

Path Length 12in	Path Length 17in	Path Length 27in
(1—>2)	(1—>5)	(1—>6)
(2—>3)	(2—>4)	(1—>8)
(1—>4)	(2—>6)	(2—>7)
(2—>5)	(3—>5)	(2—>9)
(3—>6)	(4—>8)	(3—>4)
(4—>5)	(5—>7)	(3—>8)
(5—>6)	(5—>9)	(4—>9)
(4—>7)	(6—>8)	(6—>7)
(5—>8)		
(6—>9)		
(7—>8)		
(8—>9)		

Table 1 is a summary of the actuator/sensor pairs that are employed in this experiment. The three path lengths used along with a corresponding actuator/sensor pair are 12 inches (1—>2), 17 inches (1—>5), and 27 inches (1—>6). Pairs such as (1—>3) are not used because that path is effectively covered by (1—>2) and (2—>3). It should also be noted that for every listed pair the reverse of that pair is also used for redundancy, e.g. (1—>2) and (2—>1).

Three runs of data are taken with the plate in the undamaged condition at different times to attempt to account for environmental variation. The first run is used as the comparison between all other cases and the second two runs become baseline 1 and baseline 2 in subsequent graphs. Damage is applied to the plate through the process of electrolytic corrosion. In this experiment, the aluminum plate acts as the anode and a coil of copper is used as the cathode. A DC voltage of 5V and 1A is attached to both the cathode and anode which are submerged in a saturated solution of salt water. The locations of the applied corrosion damage are shown in Figure 4.2. Damage cases 1 and 2 are applied in the same location at the midpoint between piezoceramic patches 2 and 5. Damage 1 is created by allowing the corrosion process to take place for one hour. Electrolytic corrosion is also allowed to act for 1 hour in damage case 2. Data is taken in between the successive application of corrosion damage at this location. The two stages of damage can be seen in Figure 4.3.

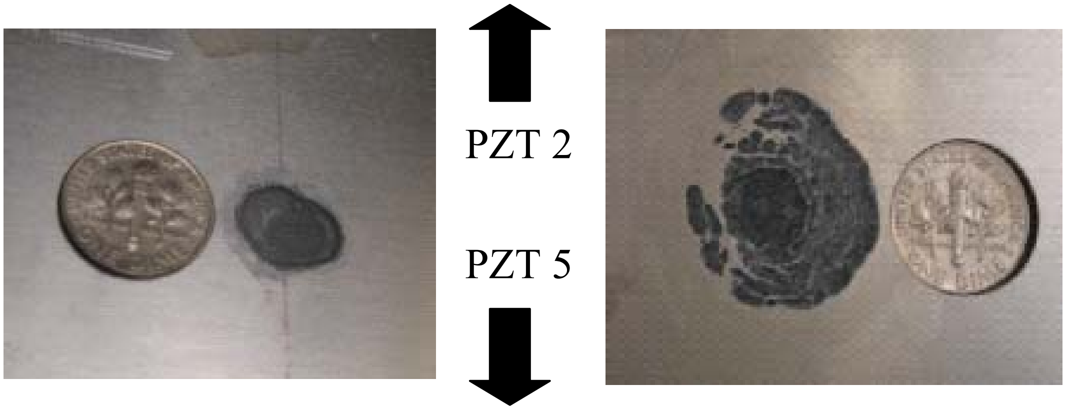

Figure 4.3. Damage case 1 (a, left) and damage case 2 (b, right) are successive damages in the same location.

Damage case 3 consists of two separate damage locations. Damage 3a (same size as damage 2) is located near actuator/sensor 7 and is created by corroding the plate for 1 hour. Damage 3b (same size as damage 2) is located between patches 8 and

9, but is only allowed to corrode for 20 minutes. Thus damage 3b is of much smaller depth than all other damage cases. These two damage cases are pictured in Figure 4.4.

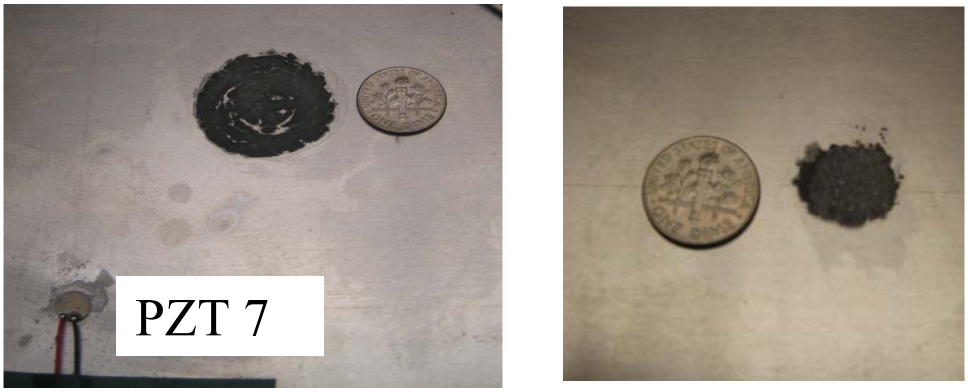

Figure 4.4. Damage case 3a (a, left) and damage case 3b (b, right).

4.1.1 Results

4.1.1.1 Path length 12in

Figure 4.5 depicts the state-space prediction error for all damage levels as well as their associated 10th and 90th quantile error bars. Redundant paths, such as (2—>1) for (1—>2), have been omitted as their results essentially mirror each other and leaving them out results in a clearer graph. The solid black line represents the path (2—>5) and shows a clear monotonic increase in prediction error from baseline to damage 1 to damage 2. This monotonic increase is an excellent result as it shows that this damage detection algorithm can not only identify the existence of damage, but that the nonlinear prediction error will increase for increasing damage. If prediction error did not have a positive correlation with damage size this method would have no potential to identify the extent of damage in any particular case. Damage 3a is shown to be close enough to PZT 7 that both paths involving that patch show a large increase in prediction error for damage case 3. The preceding damage locations all have fairly significant amount of damage, but damage 3b is a corrosion of only the surface of the plate. The path (8—>9) shows separation from all other undamaged paths for damage case 3 which shows promise that this method can be used to identify and locate very small corrosion damage. However, looking at the two previous damage cases it is clear that the prediction error level for damage 3b is actually less than level for several undamaged paths. This increase in prediction error for the undamaged paths for damage cases 1 and 2 are likely not caused by the damage itself because the prediction error returns to the baseline level for damage case 3. In fact, by examining the time histories themselves it can be seen that these differences appear to arise due to extremely slight differences in the synchronization and digitization performed by the National Instruments PXI data acquisition system. With this knowledge it may be possible to correct for this problem in subsequent testing, but it remains to be seen whether this increase in prediction error is an unavoidable byproduct of the current test configuration. Therefore, while damage case 3b has a prediction error that falls inside the range of several undamaged paths it is still promising that it is able to achieve separation from all undamaged paths for the final measurement.

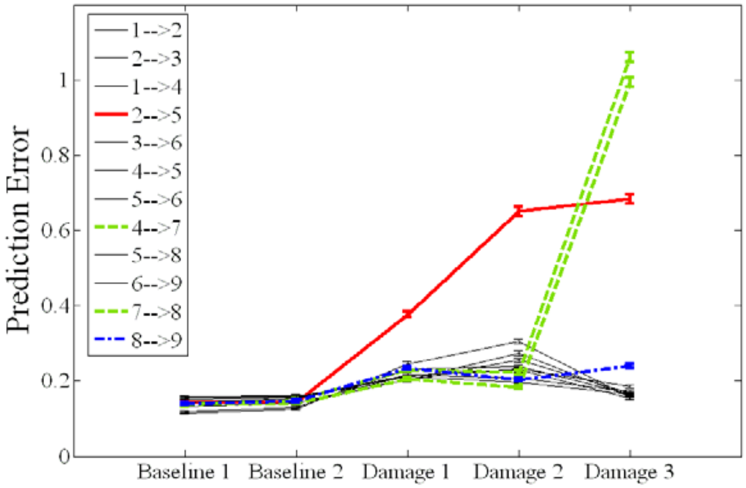

Figure 4.5. Prediction error mean and error bars for 12in path length.

4.1.1.2 Path length 17in

Figure 4.6 shows the prediction error vs. damage case plot for the 17in path length. Again, damage 3a is clearly evident in the path (5—>7). Damage 3b does not appear in this figure because it is small and does not lay on one of the interrogated paths. For this path length damage case 1 yields some interesting results. Figure 4.3 shows that damage 1 is nearly symmetric about the line from PZT 2 to PZT 5. However, the prediction error results show damage for those paths to the left of the damage, (1—>5) and (2—>4), but no apparent damage for the corresponding paths to the right of the damage, (2—>6) and (3—>5). This result appears to be counterintuitive until a larger picture of damage case 1, as seen in Figure 4.7, is examined. This picture shows several large dark spots on the plate to the left of the corrosion damage that were caused because the author was not careful to wipe up excess salt water that had spilled onto the plate before the electrolytic corrosion process was started. Because of the symmetric nature of damage 1 it is deduced that the elevation of prediction error level for the paths (1—>5) and (2—>4) is a result of the slight corrosion that occurred outside the intended damage area due to the spilled salt water. This assertion is backed up by examining the prediction error levels for damage case 2. If the aforementioned paths had been "sensing" the actual damage 1 the results for the 12in path length would result in larger prediction error for this case. For damage case 2, however, there is no change in prediction error from the previous damage case which means that the higher prediction errors for paths (1—>5) and (2—>4) could only have been produced by the salt water corrosion spots. This is an important point because it means that this damage detection method should be able to locate damage better than it appears in Figure 4.6. If the salt water corrosion spots were not present then damage cases 1 and 2 would not be detectable using the 17in path length.

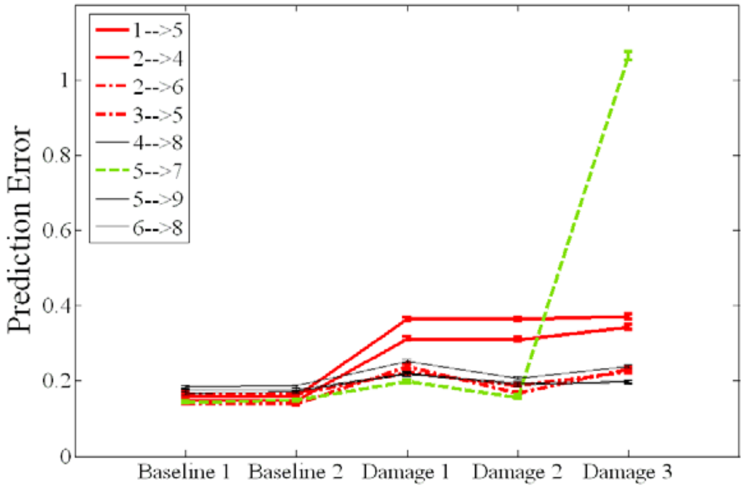

Figure 4.6. Prediction error mean and error bars for 17in path length.

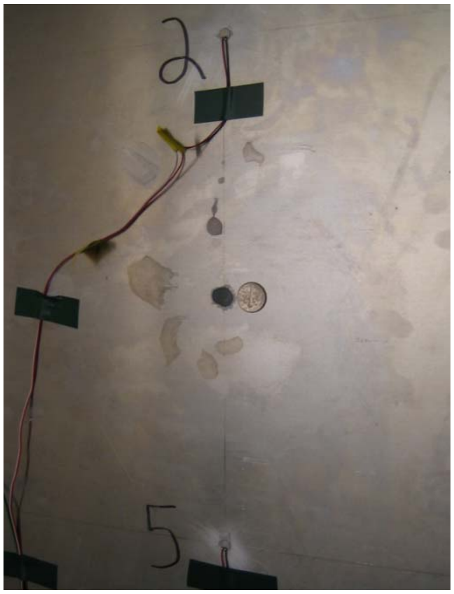

Figure 4.7. Picture of salt water corrosion spots around damage 1.

4.1.1.3 Path length 27in

Figure 4.8 shows that damage 3a is easily identified by the actuator/sensor pair that includes PZT 7 and that damage 3b is unable to be identified. Damage case 1 shows no significant increase for either of the two paths, (1—>6) and (3—>4), that intersect at the damage location. This result shows that damage 1 is too small when the propagating wave has to travel 27in between the sensors and 13.5in in either direction before the wave interacts with the damage. This results shows a limitation for such long path lengths, but as can be seen for damage case 2, if the damage is large enough a long path length can still identify the existence of damage. Damage case 3 again shows an increase in the undamaged prediction error level that partially obscures the identification of damage 2.

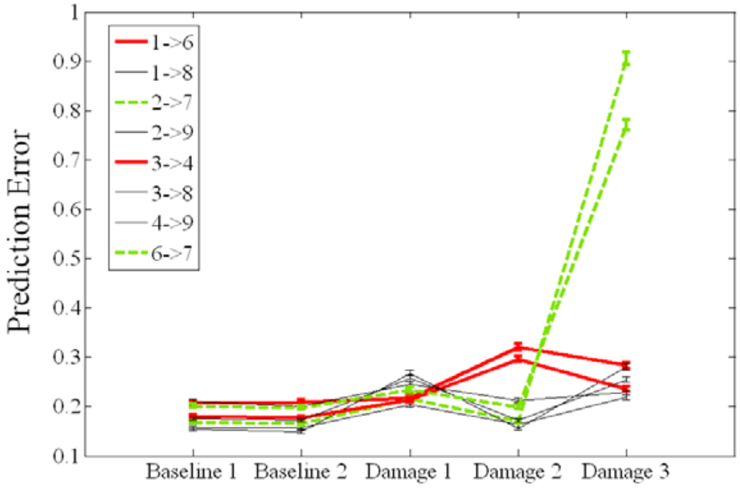

Figure 4.8. Prediction error mean and error bars for 27in path length.

4.1.1.4 Comparison to standard metrics

For this section a five peak 100 kHz toneburst excitation was sent from PZT 2 to PZT 5 and PZT 8 to PZT 9 ten times while the plate was in the undamaged condition. For damage case 1 and damage case 3b three more excitation responses were recorded. Figure 4.9 shows the averages of the normalized baseline time history (solid line) and the averages of the normalized damage case time history (dotted line) for the two small damage cases. It is clear that time-of-arrival and wave attenuation methods would be able to identify damage easily for damage case 1. However, damage case 3b shows almost no difference between the baseline and damaged waveforms. This result shows that the high frequency chaotic excitation used with spatio-temporal prediction error feature may have a greater sensitivity to guided wave metrics because, as noted in Section 4.1.1.1, our method is able to achieve separation between all undamaged paths and those paths that contain damage case 3b.

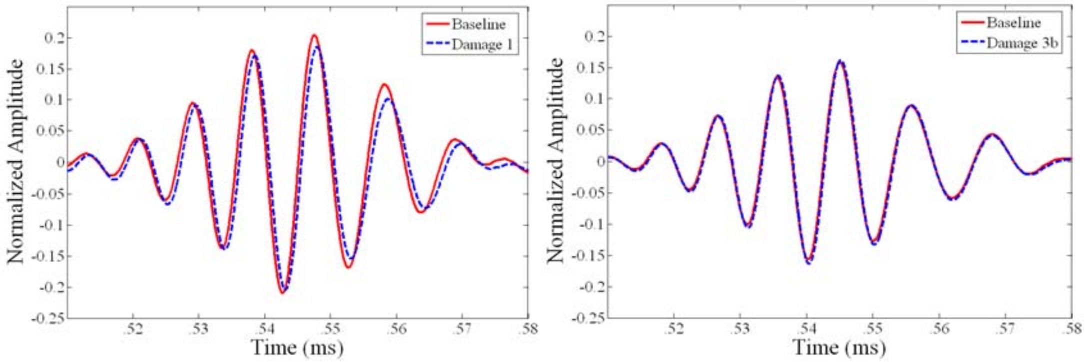

Figure 4.9. Sensed waveform for 100 kHz toneburst excitation with damage 1 between PZTs 2 and 5 (a, left) and damage 3b between PZTs 8 and 9 (b, right). The dark line is undamaged and the dotted line is the damage case.

4.2 Bolted joint preload monitoring

A common structural sub-system used in design is the moment-resisting connection, often executed by threaded fastener assemblies. Threaded fasteners are popular due to advantages such as the ability to develop a clamping force and the ease with which they may be disassembled for maintenance or replacement. It is well known that such fasteners loosen under shock, vibration, or thermal cyclic loading, and a recent comprehensive discussion of these effects is given in (Hess, 1998). A combined finite element and experimental study of dynamic shear load-induced loosening has even shown that the minimum load required to initiate loosening is lower than previously reported (Pai and Hess, 2002). Because of the highly localized nature of bolt loosening and failure, most approaches in this field have involved two- and three-dimensional finite element formulations (Bursi and Jaspart, 1997; Bursi and Jaspart, 1998, Pai and Hess, 2002). These model-based approaches have been well suited to studying the fundamental nature of the problem and guiding the design process, but they are not useful for *in situ* joint assessment in the field.

Therefore, a proof of concept experiment is created to test the effectiveness of ultrasonic chaotic excitation and state-space prediction error in bolt preload loss detection. The excitation signal is created using the process outlined in Section 2.1 such that the significant frequency information in the signal is between 80-85 kHz. This range was arbitrarily chosen as a region in which only two propagating wave modes exist and whose dispersion curves in that frequency region are mostly flat.

Testing is carried out on the bolted aluminum frame portal structure shown in Figure 4.10. The structure is made up of two 30cm x 5cm x 1cm (12in x 2in x 0.375in) vertical bars connected to a 56cm x 5cm x 1cm (22in x 2in x 0.375in) horizontal bar by two 5cm x 5cm x 0.6cm (2.5in x 2.5in x 0.25in) angle brackets. The vertical members are connected to a 60cm x 15cm x 1cm (24in x 6in x 0.5in) aluminum base plate with two more angle brackets. Two MFC patches are attached to the structure with cyanoacrylate using a vacuum bagging procedure to ensure bond quality. These Smart Material Corp. MFC patches (M 2814 P2) measure 3.5cm x 1.8cm (1.4in x 0.7in) and are approximately 2mm (0.075in) thick. The second sensing MFC patch is located directly below the patch pictured in Figure 4.10. The actuation signal is created by the output channel of a National Instruments PCI-6110 DAQ card at a rate of 4 MHz and has a voltage range of ±10 V. This signal is then routed through a Krohn-Hite 7602 wideband power amplifier and exits with a voltage range of ±20 V.

This amplified signal is sent to the actuation MFC while the sensing MFC simultaneously samples the structural response at a rate of 4 MHz.

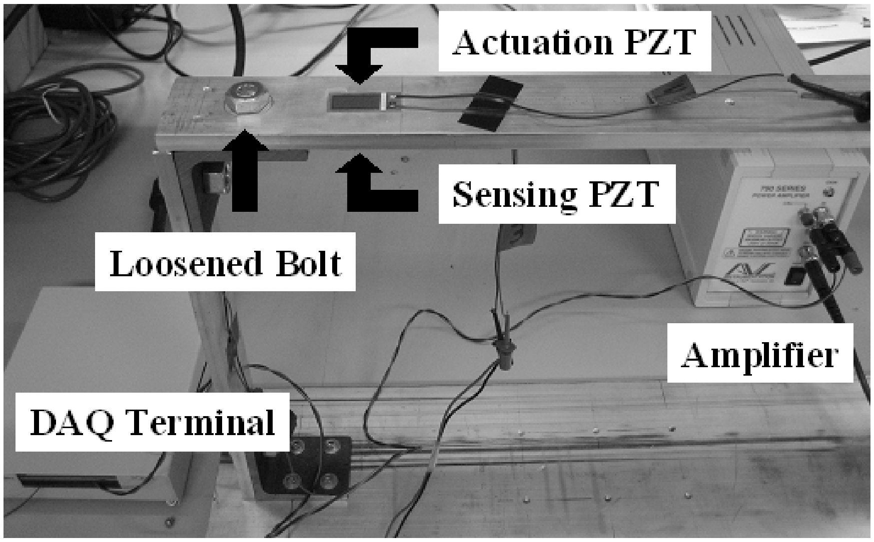

Figure 4.10. Aluminum portal structure with bolted angular connections.

The entire length of the signal is 0.1 seconds long which gives a record length of 400,000 points. Each record is broken up into 5 runs of length 80,000 points. The signal is split up into runs in order to form more robust statistical features. All runs are normalized by their standard deviation before embedding in order to remove any possible environmental variation from the signal. The number of fiducial points used for each prediction error algorithm is 10% of the total number of points, or 8,000. The number of nearest neighbors used to calculate the mass centroid is 0.1% of the total number of points, or 80. This process is repeated after loosening the bolt shown in Figure 4.10 to initiate damage into the structure. The bolt is loosened through the use of piezostack that is placed around the bolt. Voltage to the piezostack is controlled by a Piezomechanik GmbH SVR-1000 amplifier that can output voltages between 1000 V and -200 V. The bolt is torqued to 120 in-lb with 1000 V actuating the piezostack to form the undamaged condition. Voltage is then reduced by 50 V for successive damage levels with -200 V (which creates twenty-four damage levels) corresponding to approximately 80 in-lb. Torque levels and bolt preload between these two voltages are not linearly related to the piezostack voltage.

4.2.1 Results

Figure 4.11 depicts the state-space prediction error for all damage levels as well as their associated 10th and 90th quantile error bars. The results for this damage metric show that the state-space prediction error algorithm is able to statistically identify and separate very small levels of incipient damage due to bolt preload loss. There is a strict monotonic increase in prediction error across as the piezostack voltage decreases (bolt preload decreases). The damage metric levels off between 300 V and 0 V and then begins to increase at a faster rate until the lowest piezostack voltage at -200 V. The ability of this method to detect such small changes in bolt preload level is due to the high frequency content (and therefore short wavelength) of the excitation signal. A global excitation could never determine and locate damage at these incipient levels. Computing these prediction errors is computationally expensive, however, and therefore the performance of computationally inexpensive AR model metrics is examined.

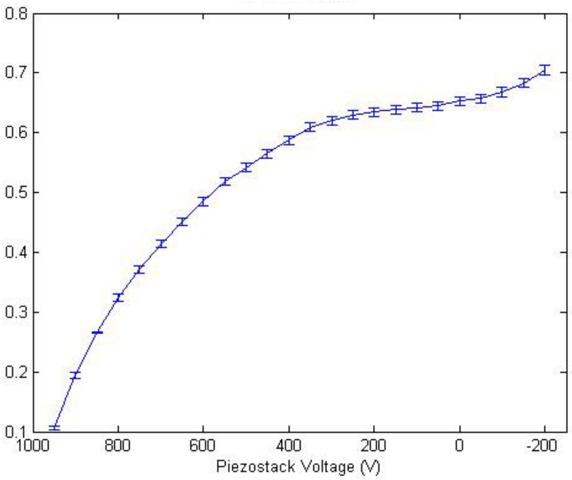

Figure 4.11. Prediction error mean and error bars for increasing damage (decreasing piezostack voltage).

4.2.2 AR model comparison

The same data are examined using an AR model with an order of p=5 to see how well damage can be detected using a very simple forward linear predictor.

Figure 4.12 depicts the standard deviation of the residual error e that is obtained from the AR model. Both standard temporal regression and the extended spatio-temporal regression trend similarly for increasing damage. The results from this much simpler calculation (as compared to the state-space prediction error) show that it may be possible in certain cases to use only standard deviation of the residual error as a damage feature instead of calculating attractor-based prediction errors. Therefore, in Section 5 only AR model-based features are used to discriminate damage.

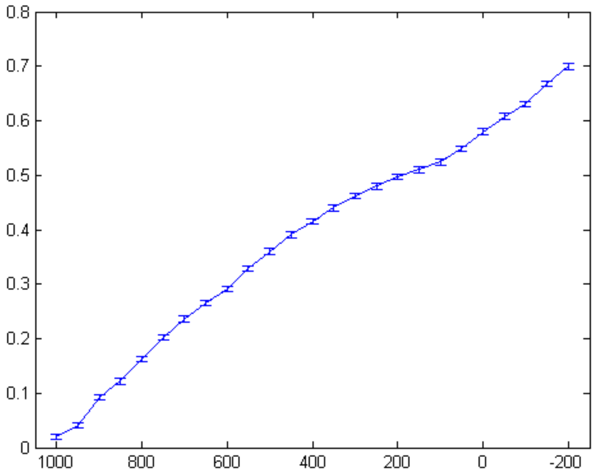

Figure 4.12. Standard deviation of residual errors from AR model.

4.3 Section summary

The results from Section 4.1 indicate that the use of chaotic ultrasonic waves can be used for the detection of corrosion damage in plate-like structures. This effect is important because our method offers important advantages over standard time-of-arrival and attenuation metrics in sensitivity to damage and performance under non-ideal actuator/sensor bond quality. In this experiment it was discovered that PZT 1 and PZT 6 had degraded bonding conditions that significantly changed the shape of any wave that was excited or sensed by one of these two piezoceramic patches. This change in shape would make it difficult to institute any kind of standard time-of-arrival or attenuation feature. It does not affect the spatio-temporal prediction error because this damage detection algorithm only looks for changes in attractor geometry from a baseline state. Thus, even if the undamaged attractor does not resemble the undamaged attractors from paths with correctly bonded piezoceramic patches it is still possible to easily and automatically identify when and where damage occurs.

The results from Section 4.2 indicate that the use of chaotic ultrasonic waves for the detection of incipient levels of bolt preload loss (even in a joint with a complicated geometry as is present in this experiment) is possible. The ability of the spatio-temporal attractor-based prediction error metric to identify small levels of incipient damage is particularly encouraging, as characterizing damage to a structure at its earliest stages allows for the possibility of condition-based maintenance. This method also has advantages over standard guided wave methods such as time-of-arrival and wave attenuation, which can only be used on structures with simple geometries. The standard deviation of the residual errors obtained from a standard temporal AR model of order p=5 is a damage feature that is able to effectively resolve incipient damage levels at a significantly lower computation cost to the state-space prediction error method.

There are still several issues that remain unresolved. Further work must be done in trying to eliminate the unwanted increase in prediction error of the undamaged paths for several damage cases. If this reduction can be achieved (perhaps through a different data normalization technique) it will be possible to detect smaller levels of damage. The suitability of the excitation signal is another concern that must be addressed. The signal parameters for this experiment were chosen arbitrarily as an example of a short wave packet (40 milliseconds) that still exhibited a substantial amount of chaotic behavior. It is possible that a more appropriate excitation could be used that would yield better results.

5 AUTO-REGRESSIVE MODEL APPLICATIONS

This section will detail the use of the damage-sensitive features based on auto-regressive (AR) models outlined in Section 3.2.2. These features are employed instead of the spatio-temporal prediction error techniques discussed in Section 4 because they possess similar abilities to discriminate damage as state-space prediction error, but at a fraction of the computation and storage cost. This reduction in processing complexity is especially important for any embedded SHM system. Section 5.1 uses the damage size/type classification procedure outlined in Section 3.2.2.3 on a single bolt metal lap joint and the same multiple bolt metal portal structure that is used as a test structure in Section 4.2. Section 5.2 then examines the possibility of using evolutionary algorithms to optimize (in a detection sense) the active chaotic excitation signal used for the single bolt lap joint. Section 5.3 first applies the same classification procedure outlined in Section 3.2.2.3 to an adhesively-bonded composite wing-to-spar specimen. This damage feature is used to identify multiple disbond sizes as well a poorly bonded section along the wing-to-spar bond. It is shown that this classification scheme is able to compensate for the effects of temperature variability generally experienced by an in-service aircraft. The complete two-step classification scheme introduced in Section 3.2.2 is then used on a set of similarly configured composite wing-to-spar structures. The effects of within-unit and unit-to-unit variability are able to be studied by testing on multiple structures.

5.1 Bolted metal connections

Having shown the ability of AR model-based features to identify incipient levels of bolt preload loss in Section 4.2.2, the damage classification scheme outlined in Section 3.2.2.3 is applied to two experimental test platforms. One structure is a single-bolt lap joint and the second structure is the portal assembly that has already been introduced in Section 4.2. The same chaotic ultrasonic excitation used in the initial bolt preload monitoring study discussed in Section 4.2 (significant frequency information in the signal is between 80-85 kHz) is also used for each of the two test structures in this section. Each input signal is applied to the structure 50 times and then averaged to reduce experimental noise. The actuation signal is created by the output channel of a National Instruments PCI-6110 DAQ card at a rate of 4 MHz and routed through a Krohn-Hite 7602 wideband power amplifier. This amplified signal is sent to the actuation MFC while the sensing MFC simultaneously samples the structural response at a rate of 4 MHz.

5.1.1 Single bolt lap joint

The first experimental apparatus on which testing was carried out is the single bolt lap joint shown in Figure 5.1. The structure is made up of two 30cm x 5cm x 1cm (12in x 2in x 0.375in) aluminum bars connected to each other with a single bolt. Two MFC patches are attached to the structure with one on both sides of the joint. Each of these Smart Material Corp. MFC patches (M 2814 P2) has an active area of 3.5cm x

1.8cm (1.4in x 0.7in), are approximately 2mm (0.075in) thick and are bonded to the structure 5cm (2in) from the bolted connection (on each side) using cyanoacrylate. Due to the symmetry of the problem, it is not important which patch is used as the sensor and which as the actuator and either configuration will yield similar results. For this experiment the transducer on the left side of the lap joint in Figure 5.1 is used as the actuator.

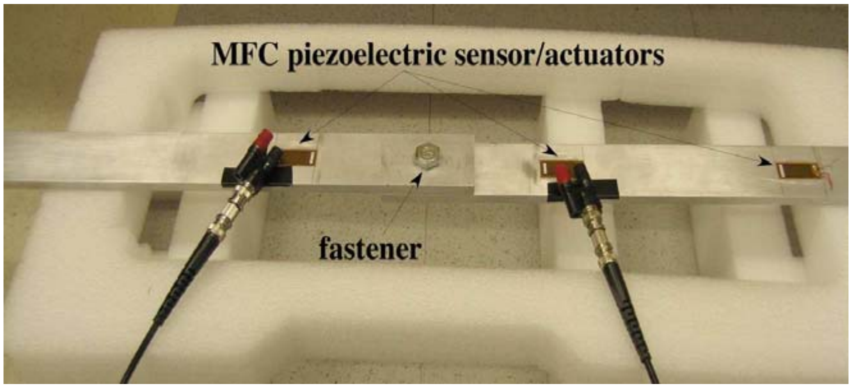

Figure 5.1. Single bolt lap joint experiment.

Table 5.1: Classification "vote" distribution of experimental lap joint data.

Actual Condition	***Votes***				**Outcome**
	Condition 1 (Loose)	**Condition 2 (Finger)**	**Condition 3 (3.5 N-m)**	**Condition 4 (14 N-m)**	
Condition 1 (Loose)	**175**	46	0	4	Correct
Condition 2 (Finger)	1	**150**	74	0	Correct
Condition 3 (3.5 N-m)	0	37	**188**	0	Correct
Condition 4 (14 N-m)	0	24	122	**79**	Incorrect

In this study, using 30 distinct chaotic inputs, data is taken at each step of a bolt tightening sequence in which the bolt condition is: 'loose' (Condition 1), 'finger-tight' (Condition 2), 3.5 N-m (Condition 3), and 14 N-m (Condition 4). This sequence is then repeated three times to simulate assembly and disassembly of the joint in a real structure. The first two assembly/disassembly sequences are used to create a training database. Structural responses obtained during the third sequence are used as test inputs. To test the ability of the classification scheme described in Section 3.2.2.3 to correctly identify bolt preload condition, 15 of the 30 generated response time histories are selected as database training inputs. The remaining 15 responses are used as test set inputs. All four bolt condition time responses are examined for each of the 15 test inputs. The classification scheme then determined, in each case, the actual bolt condition based solely on knowledge it acquired from the 15 database training inputs. Table 5.1 shows the vote results for the 4 conditions. Each row represents the actual condition of the bolt and each column is the number of classification votes assigned to that condition. If the statistical classifier correctly identified every test condition the table would only have votes along the diagonal. The correct bolt conditions are shown in bold.

The true bolt condition was correctly assessed by the statistical classification algorithm in all cases but Condition 4 (the most tight), which was estimated by vote-counting to be in Condition 3. There are several factors contributing to this damage case misidentification. First, specifying bolt torque on a real joint can be difficult and in this experiment an inexpensive torque wrench with a fairly low resolution was used. Second, the transfer relationship between torque and preload is hysteretic, nonlinear and is highly dependent on local contact, which will vary each time the bolt is tightened. Third, in this experiment it was difficult to maintain the boundary conditions of the lap joint between tests and it is believed that this also led to inflated number of incorrect votes. Given these concerns, the actual preload indicated by a particular torque level may vary significantly from test to test and almost certainly contributed to a much lower percentage of correct identification of individual test cases (66%) than may have been possible in a more rigorously controlled experiment.

In future tests an instrumented bolt can be used so that a direct measure of preload is available instead of just bolt torque. This should improve results, however in real world situations bolt preload will be specified by torque specifications. Other improvements that are not dependent on knowing exact bolt preload level are possible. Foremost among these are the choice of parameters that affect the creation of the input time signals (carrier frequency f_c, frequency ratio R, modulation depth d) as well as feature extraction (AR model order, size of training and test databases). Using genetic algorithms (specifically differential evolution) to create an optimal input waveform is discussed in Section 5.2.

5.1.2 Multiple bolt portal structure

As mentioned in the previous section, it is believed that a test bed with more reliable end boundary conditions should result in a greater percentage of correct classifications. It is also desired to test a structure that had multiple bolted connections in order to examine the ability of the statistical classification algorithm to identify multiple damage locations within a structure. This ability to locate damage within a multiple bolt structure is a necessity, as virtually all practical field applications will fall into this category. Therefore, the aluminum frame structure shown in Figure 5.2 is employed to address these concerns. This is the same test structure used in Section 4.2.

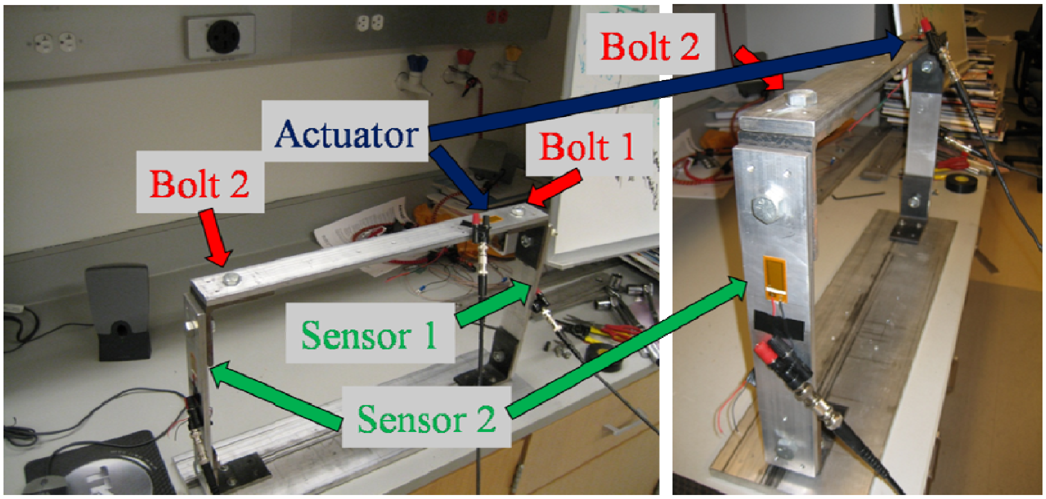

Figure 5.2. Multiple joint frame structure experiment.

Table 5.2 shows the damage cases that are considered in this study. 'Tight' indicates 14 N-m, 'finger tight' indicates nominal preload (less than 3 N-m), and 'loose' indicates no preload. While there are thus 7 “conditions” defined, as indicated, there are only 3 damage levels for each bolt. Similar to Section 5.1.1, the last 7 cases were used as test cases against the training database created using the first 14 cases.

Table 5.2: Test conditions of the multiple joint frame structure.

Case	Bolt 1 Condition	Bolt 2 Condition
1	Tight	Tight
2	Finger Tight	Tight
3	Loose	Tight
4	Tight	Finger Tight
5	Tight	Loose
6	Finger Tight	Finger Tight
7	Loose	Loose
8	Tight	Tight
9	Finger Tight	Tight
10	Loose	Tight
11	Tight	Finger Tight
12	Tight	Loose
13	Finger Tight	Finger Tight
14	Loose	Loose
15	Tight	Tight
16	Finger Tight	Tight
17	Loose	Tight
18	Tight	Finger Tight
19	Tight	Loose
20	Finger Tight	Finger Tight
21	Loose	Loose

Table 5.3: Classification "vote" distribution of multiple joint frame data.

Damage Case	MFC 1(Bolt 1)			MFC 2 (Bolt 2)		
	Tight	Finger Tight	Loose	Tight	Finger Tight	Loose
15	**225**	0	0	**225**	0	0
16	0	**152**	73	**225**	0	0
17	2	115	**108**	**225**	0	0
18	**225**	0	0	0	**134**	91
19	**225**	0	0	0	98	**127**
20	1	**140**	84	0	**196**	29
21	0	3	**222**	06	1	**224**

The classification vote chart for each MFC sensor is shown in Table 5.3. The bold numbers in each row indicate the true condition of the bolt. Therefore a correct classification is made if the bold number is the largest in its row. As such, the correct classification was made in each case except for bolt 1 in damage case 17. The damage localization ability of this method is still strong as the overall percentage of correctly identified individual test cases is 84%. The 'tight' condition was classified correctly for almost every individual test signal. However, the distinction between 'finger tight' and 'loose' is less clear (especially given that ‘finger tight’ is a very qualitative, non-repeatable condition). This unclear discernability between the ‘finger tight’ and ‘loose’ damage conditions suggests grouping these two damage cases into one simple ‘loose’ category and using the classification scheme to make a decision only whether the joint is damaged or undamaged.

Table 5.4: Classification "vote" distribution of multiple joint frame data for healthy/unhealthy determination.

Damage Case	**MFC 1(Bolt 1)**		**MFC 2 (Bolt 2)**	
	Tight	**Loose**	**Tight**	**Loose**
15	**225**	0	**225**	0
16	0	**225**	**225**	0
17	2	**223**	**225**	0
18	**225**	0	0	**225**
19	**225**	0	0	**225**
20	1	**224**	0	**225**
21	0	**225**	0	**225**

Therefore, the categories 'finger tight' and 'loose' were combined into a more general 'loose' category by establishing the critical threshold value at a preload level of ‘finger tight’. In this attempt to make a purely healthy/unhealthy joint status determination, proper classification is achieved with each damage case. This simple classification works so well that votes for individual test responses choose the correct joint configuration greater than 99% of the time, as can be seen in Table 5.4.

5.2 Optimized excitations

Section 5.1 detailed the ability of active chaotic ultrasonic excitation combined with an AR model-based classification scheme to detect bolt preload loss and location in a multiple-joint frame structure. However, the waveform used in the previous section was not examined for suitability to the particular application. The use of evolutionary algorithms to optimize active excitations has already been studied in the vibration domain (Olson et al. 2007; Olson et al. 2009a; Olson et al. 2009b). Therefore, in this section the parameters that are required to create a particular chaotic ultrasonic excitation are manipulated by an evolutionary algorithm in order to change the dynamic properties of the waveform. Each generated waveform is then applied to the structure in a damaged and undamaged state. The fitness of each solution is measured by how well the damaged state can be differentiated from the baseline undamaged state and evolutionary pressure forces the creation of a waveform with improved detection capability. The simple bolted lap joint shown in Figure 5.1 is used as the test structure for this study. The bolt is loosened through the use of a piezostack actuator that is placed around the bolt. Voltage to the piezostack is controlled by a Piezomechanik GmbH SVR-1000 amplifier that can output voltages between 1000 V and -200 V. The bolt is torqued to 120 in-lb with 1000 V actuating the piezostack to form the undamaged condition. Voltage is then reduced to -200V for the damaged condition which corresponds to approximately 80 in-lb.

5.2.1 Feature extraction

Once the chaotic ultrasonic wave is launched into the structure and detected, after its interaction with the joint, the primary task remains what feature(s) from the measured waveform may be extracted to assess the joint. Two structural response time series are obtained while the joint is in an undamaged state and one response time series is gathered while the joint is in a damaged condition. One of the undamaged responses is used to create an AR model of order p=5 to be used as the baseline. Residual errors are then calculated from the remaining undamaged signal as well as the damaged signal using the baseline AR coefficients. Therefore for each tested excitation, a distribution of residual errors from the baseline-undamaged comparison is gathered as well as residual errors corresponding to the baseline-damaged comparison. The fitness of the prescribed excitation signal is then calculated with the following function:

$$\text{fitness} = \frac{(\mu_\text{b} - \mu_\text{c})^2}{\sqrt{\sigma_\text{b}\sigma_\text{c}}} \tag{5.1}$$

where μ_b and σ_b are the mean and standard deviation of the baseline-undamaged comparison and μ_c and σ_c are the mean and standard deviation of the baseline-damaged comparison. The fitness function is designed to reward excitations that result in a larger separation of means of the residual error from the AR model. In addition, a smaller variance will result in higher fitness.

5.2.2 Differential evolution

The evolutionary algorithm that is employed in this study is known as differential evolution and was first introduced by Storn and Price (Storn and Price 1997). Like all genetic algorithms, differential evolution seeks to steer a randomly generated initial population toward an optimal solution via multiple generations of mutation, crossover and selection. Populations are comprised of vectors that contain real values for a number of parameters that are to be optimized. Suitability of a particular solution vector is assessed with the fitness function shown in Eq. (5.1). Each vector in the population is compared with a trial vector that has been created through mutation and crossover. The vector of parameters that produces a higher value using the fitness function is advanced to the next generation until the population becomes saturated with high fitness solutions.

Mutation is accomplished through the use of vector differentials. Two vectors V_1 and V_2 are randomly chosen from the population and subtracted to form a vector differential. The mutated vector is then constructed by multiplying this differential by a scaling factor F and then adding this to a third vector V_3 so that the overall expression for the mutation vector is $V_3 + F*(V_1- V_2)$. A target vector from the population is then chosen for the crossover step in which one value from either the target vector or mutated vector is chosen for each parameter to create the trial vector.

This selection is accomplished by generating a random number between zero and unity. If this number is less than the crossover constant *CR* then the value from the target vector is selected and if it is greater than *CR* the value from the mutated vector is chosen. This is repeated for each parameter in the vector. The parameters from the target and trial vectors are then used to create two excitation signals. The vector producing the excitation signal that results in a higher fitness value is then advanced to the next generation. The particular algorithm used in this study also employs elitism; the maximum fitness in each generation is automatically saved and advances to the next generation.

Table 5.5: Allowable values of parameters to be optimized.

Parameter	Minimum Value	Maximum Value
R	1E-6	0.25
d	0.1	1
f_c	40 kHz	400 kHz
N	4000	100000

The four parameters that comprise a vector in the differential evolution algorithm are frequency ratio R, modulation depth d, carrier wave frequency f_c and signal length N. The minimum and maximum allowable values for these parameters are summarized in Table 5.5. A population size of 10 is used in this study and the algorithm is run for 100 generations. The scaling factor has a value of $F = 0.9$ and the crossover constant is $CR = 0.5$.

5.2.3 Results

Figure 5.3 depicts the results of the experiment by showing the maximum fitness for each generation of the differential evolution algorithm. At the end of 100 generations the maximum fitness is 1.46 which is two orders of magnitude greater than the initial random population average fitness of 0.01. The maximum and average fitnesses were still increasing in the 97th generation so it is likely that a larger number of generations could have produced a result with higher fitness.

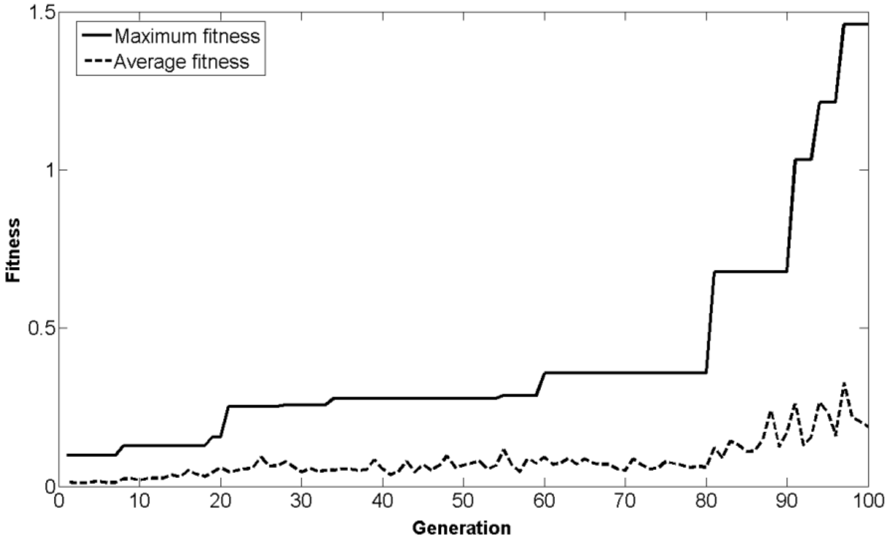

Figure 5.3. Maximum and average fitness vs. generation.

Table 5.6: Optimal parameter values.

Parameter	Optimal Value
R	6.92E-4
d	1
f_c	400 kHz
N	100000

Table 5.6 shows the parameter values that were able to produce the maximum fitness values. It is clear that the evolutionary algorithm preferred the maximum allowable value for modulation depth, carrier wave frequency, and signal length. This implies that if carrier wave frequency or signal length had been allowed to increase beyond the maximum allowable values that a greater fitness value could be obtained. Figure **5.4** shows the excitation signal that these optimal values produced, the residual error from the baseline-damaged comparison as well as the residual error distributions of the baseline-undamaged and baseline-damaged comparisons. It is clear that the differential evolution has produced a solution that is a two-tone beat sequence. This two-tone optimal excitation was also discovered in studies by Olson et al. (Olson et al. 2007; Olson et al. 2009). Also, the sinusoid is somewhat undersampled with only 10 samples per period (400 kHz sinusoid sampled at 4 MHz). Figure **5.4**b shows that the largest residual errors occur at the beginning of the time series when the waveform has just travelled through the joint and arrived at the sensing MFC. However this region of larger residual error is not what causes the fitness to increase as the errors are symmetrical and therefore do not affect the mean. In fact it is the long region of relatively low residual error during which the lap joint is undergoing full-field insonification that the residual errors become bimodal (as can be seen Figure **5.4**c) which causes the mean to shift. This region is the reason the evolutionary algorithm chose the longest possible signal length. Figure **5.4**c shows that with the extracted feature and fitness calculation used in this study that there is not a very large separation between undamaged and damaged distributions as both are centered on zero. It appears that the bimodal nature of the damaged distribution is the cause of the high fitness value.

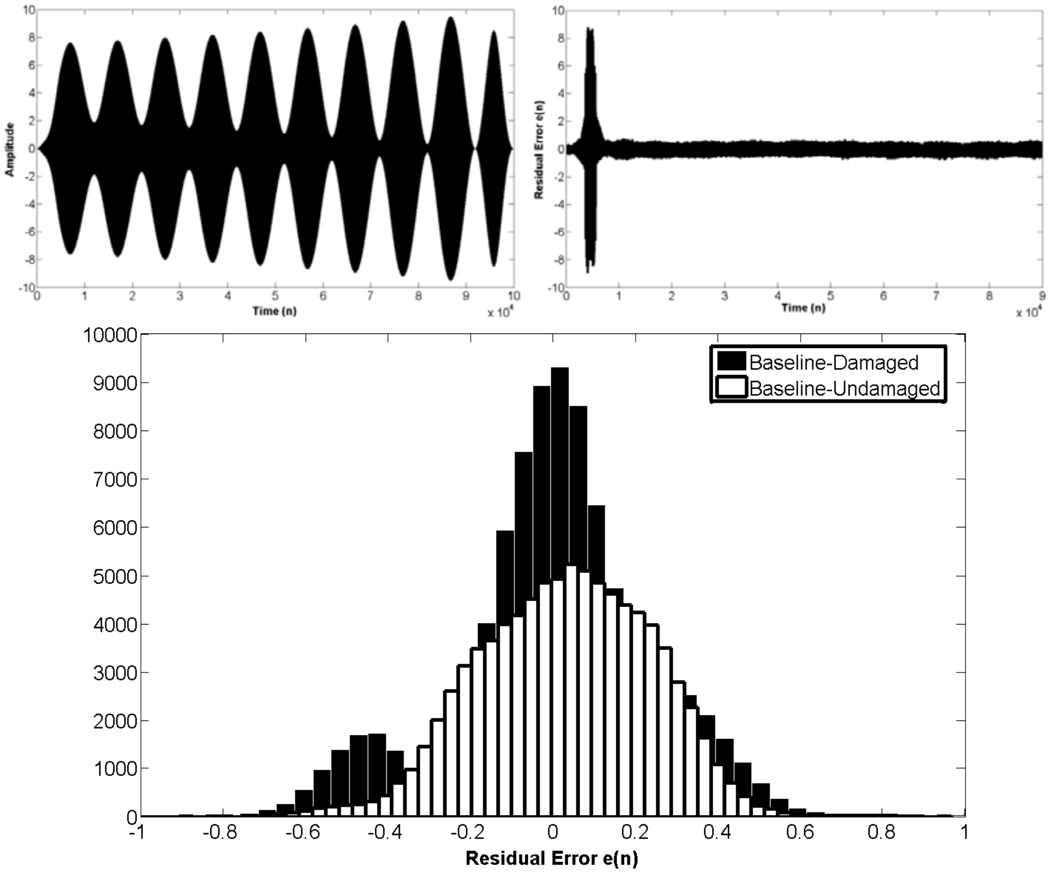

Figure 5.4. (a, top left) Optimal excitation signal; (b, top right) residual error *e(n)* from the baseline-damaged condition using optimal excitation; (c, bottom) baseline-undamaged and baseline-damaged residual error distributions using optimal excitation.

5.2.4 Conclusions

In conclusion, evolutionary algorithms identified an optimal excitation whose fitness is two orders of magnitude greater than the fitness of an excitation formed from random parameters. This optimal excitation is largely sinusoidal in nature that is likely a byproduct of the AR model prediction error feature that is used for damage discrimination. It is also shown that long signal lengths gave higher fitness results due to the bimodal nature of residual errors during the full-field insonification stage of the excitation response.

It is worth noting that when using genetic algorithms there is no guarantee that a truly optimal global solution will be found by the algorithm, which can settle on a less optimal local maximum fitness. However, an increase of fitness of two orders of magnitude is still quite improved for a proof of concept study. There are several changes that could be made to this algorithm to improve the optimality of the solution. By using unaltered residual error output from an AR model, the error distribution will always have a mean at or near zero. If the absolute value of the residual error is used instead it would be possible to separate the means and therefore the distributions of the undamaged and damaged cases. With a non-zero mean, evolutionary pressures should prioritize a shorter, more chaotic signal with only the large residual error portion remaining instead of the long region of relatively low residual errors. This would lead to much better damage resolution and higher fitness values. Another parameter that was not optimized in this study was the order of the AR model. However, the two orders of magnitude improvement in fitness over random excitation parameters proves that signal optimization is an important task for any SHM system, and that evolutionary algorithms are capable of optimizing these parameters.

5.3 Adhesively-bonded composite joints

5.3.1 Single composite plate

This study examines the ability of the damage size/type classification method outlined in Section 3.2.2.3 to classify different bond state damage conditions of an adhesively-bonded composite joint, including various disbond sizes and a poorly cured bond. The test structure is analogous to a wing skin-to-spar bonded joint and consists of a custom made 8-ply $[0/\pm45/0]_s$ carbon fiber-reinforced plastic (CFRP) plate that is bonded to a tubular CFRP spar. The CFRP plate measures 30cm x 30cm x 1mm (12in x 12in x 0.04in) square and the spar has an outer square diameter of 5cm x 5cm (2in x 2in) with a wall thickness of 6mm (0.25in). The bonded area contains two different disbond sizes of 1.6cm^2 and 6.4cm^2 ($0.25\ \text{in}^2$ and $1.0\ \text{in}^2$) created using Teflon inserts as well as a portion of the bond that has been poorly cured by using only 50% of the prescribed level of hardener. An active excitation signal is imparted to the structure through a MFC patch on one side of the bonded joint and sensed using an equivalent MFC patch on the opposite side of the joint and there is an MFC actuator/sensor pair for each bond condition to be identified. The test structure is pictured in Figure 5.5.

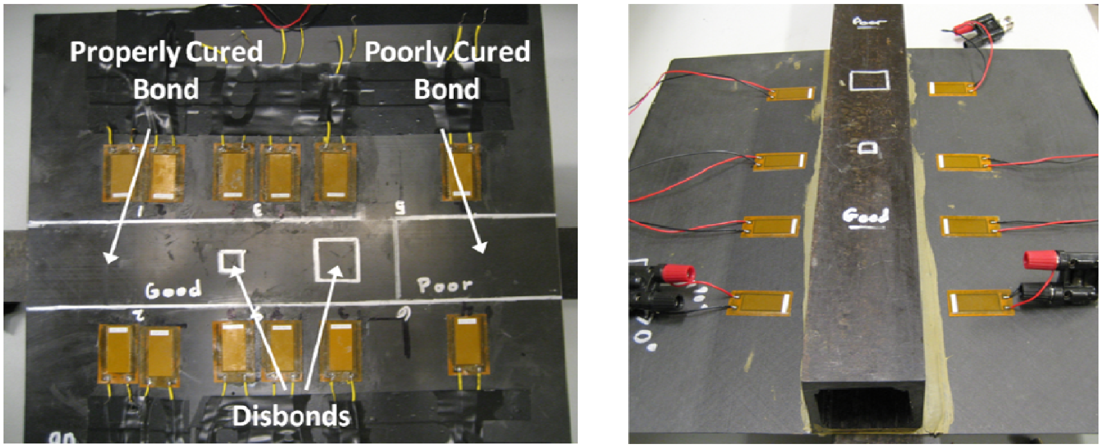

Figure 5.5. Experimental platform showing location of disbonds and poorly cured section (a, left) and location of MFC actuators for each bond condition (b, right).

Two MFC actuator/sensors were attached to the structure on each side of the bond for each of the three damaged bond states as well as one pair for the undamaged bond area for a total of eight MFC patches. Each MFC patch is affixed to the structure one inch from the spar bond line. Each input signal is applied to the structure 25 times and then averaged and filtered to reduce experimental noise. The actuation signal is created by the output channel of a National Instruments PCI-6110 DAQ card at a rate of 4 MHz and routed through a Krohn-Hite 7602 wideband power amplifier. This amplified signal is sent to the actuation MFC while the sensing MFC simultaneously samples the structural response at a rate of 4 MHz.

For the following experiments, in order to test the ability of the classification scheme described in Section 3.2.2.3 to correctly identify bond condition, 30 time response histories are created using a specific set of signal creation parameters. Half of these 30 generated response time histories are selected as database training inputs. The remaining 15 responses are used as test set inputs. All four bond conditions are probed three times with the first two time history responses being used for the training database and the remaining responses used to determine bond condition for the test set inputs. In each case the actual bond condition is determined based solely on knowledge it acquired from the 15 database training inputs.

5.3.1.1 Optimal parameter investigation

In order to determine the set of input signal parameters that produce optimal bond state identification, the statistical classification scheme is employed for an array of signal parameters and the overall ability of each set of parameters to correctly identify each bond state is then examined. Previous numerical and experimental work done by Matt, Bartoli and Lanza di Scalea on the same test structure showed that, when using through transmission characteristics of simple toneburst inputs, an excitation frequency of 200 kHz was best able to identify bond state condition due to a coupling of S_0 and A_1 modes at that frequency (Matt et al. 2005; Lanza di Scalea et al. 2007). In this study a number of excitation center frequencies from 100 kHz to 300 kHz are considered, as well as frequency ratios ranging from 0.01 (nearly sinusoidal) to 0.50 (highly chaotic). When considering the feature extraction parameters a number of AR model orders from 3 to 25 are employed. Figure 5.6a-d depicts the ability of the statistical classification scheme to correctly identify bond condition by plotting the percentage of correct votes against the various signal input and feature extraction parameters already discussed.

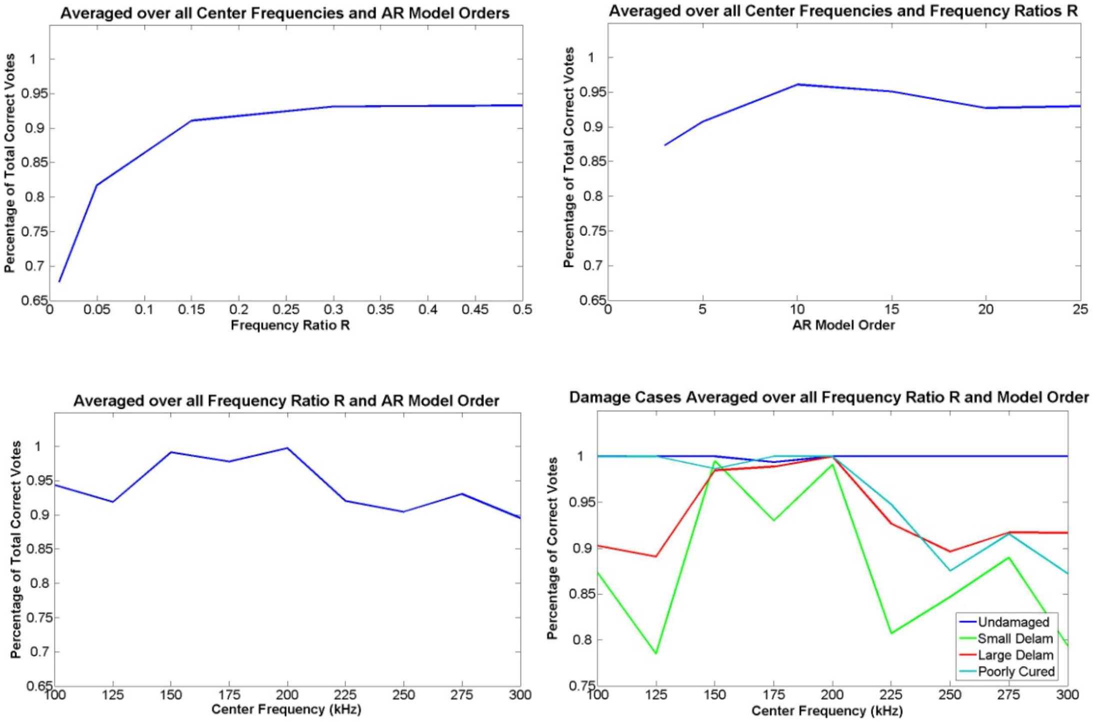

Figure 5.6. Classification scheme results showing percentage of total correct votes vs. (a, top left) frequency ratio, (b, top right) AR model order, (c, lower left) center frequency and (d, lower right) center frequency for each individual bond condition.

Figure 5.6a shows the ability of the statistical classification scheme employed together with chaotic insonification to correctly identify bond condition for various frequency ratios. As previously mentioned, the lower the frequency ratio the more sinusoidal the input signal appears and conversely the higher the frequency ratio the more chaotic the input signal appears. This signal parameter characteristic occurs because as the frequency ratio becomes small, the chaos operates on a longer time scale. If a small enough time window is used to create the signal, a very small *R* value will result in the chaotic time scale being much longer than that of the entire signal. In this case the signal will appear to be almost sinusoidal. The opposite effect holds true if a large frequency ratio is used because the time scale the chaos operates on will be much smaller than the length of the signal and the signal will therefore contain more chaotic information. It is clear that a signal with more chaotic information, when paired with this pattern recognition scheme, is best able to determine true bond state condition. There is negligible difference between a frequency ratio of 0.3 and 0.5 but the overall trend that a more chaotic signal provides greater classification ability is a sufficient conclusion. Figure 5.6b depicts the effect of AR model order on the damage identification ability of the statistical classification scheme. In general, if too low of an AR model is used (anything less than 10) the percentage of total correct votes has a noticeable decrease. When averaged over all frequency ratios and center frequencies an AR model order of 10 does slightly better than higher AR model orders. However, the effectiveness of a particular model order is clearly dependent on the particular frequencies in which the chaotic information is present. Closer investigation of the data reveal that, depending on the signal input parameters, an AR model order somewhere between 10 and 20 will produce optimal classification of each particular bond state.

Figure 5.6c illustrates the effect of various center excitation frequencies on the ability to correctly classify bond condition. The graph shows that center frequency is a highly important parameter as there appears to be “sweet spots” where the algorithm correctly classifies almost 100% of individual test cases (150 kHz and 200 kHz) as well as several frequencies which do not perform as well including 175 kHz which is intermediate to the two sweet spots in the frequency regime. As previously mentioned, numerical simulations (Matt et al. 2005) showed a mode coupling occurring at 200 kHz which could be the reason for the excellent performance of the damage detection algorithm across all frequency ratios and model orders at that frequency. The same study does not indicate a mode coupling effect at 150 kHz. However, these are only numerical results, and the true physical structure may contain mode coupling effects at 150 kHz. Figure 5.6d shows that the undamaged bond condition is correctly identified for almost 100% of the individual input signals for any center frequency. The ability to discern the poorly cured bond state appears to decrease as center frequency increases and the small disbond case is the most often misidentified bond condition, as would be expected due to its size.

5.3.1.2 Temperature variability

The experimental apparatus used in this study is meant to simulate a wing skin-to-spar bonded joint that is used in aerospace applications. Therefore, if this statistical classification scheme using chaotic insonification is to be used for *in situ* health monitoring, including in-flight and on the ground, its behavior and effectiveness relative to external temperature must be considered. This study therefore employs the use of a thermal chamber to test the efficacy of the above outlined method for temperatures varying from -40°C to 40°C, a range that covers most flight and ground conditions. For the thermal chamber test a center frequency of 200 kHz, frequency ratio of 0.5 and AR model order of 10 are employed as these parameters produced near 100% correct identification of individual test signals for the room temperature experiments. Figure 5.7 shows the initial thermal chamber results for cases in which the baseline AR coefficients are determined at various temperatures. It is clear that the damage detection algorithm only performs well at temperatures close to that of the temperature at which the baseline AR coefficients are determined. A temperature change of more than 10 degrees Celsius usually results in significant reduction of classification effectiveness. However, when the proper baseline AR coefficients are used for a particular temperature the statistical classification method still achieves near 100% correct classification of individual test signals.

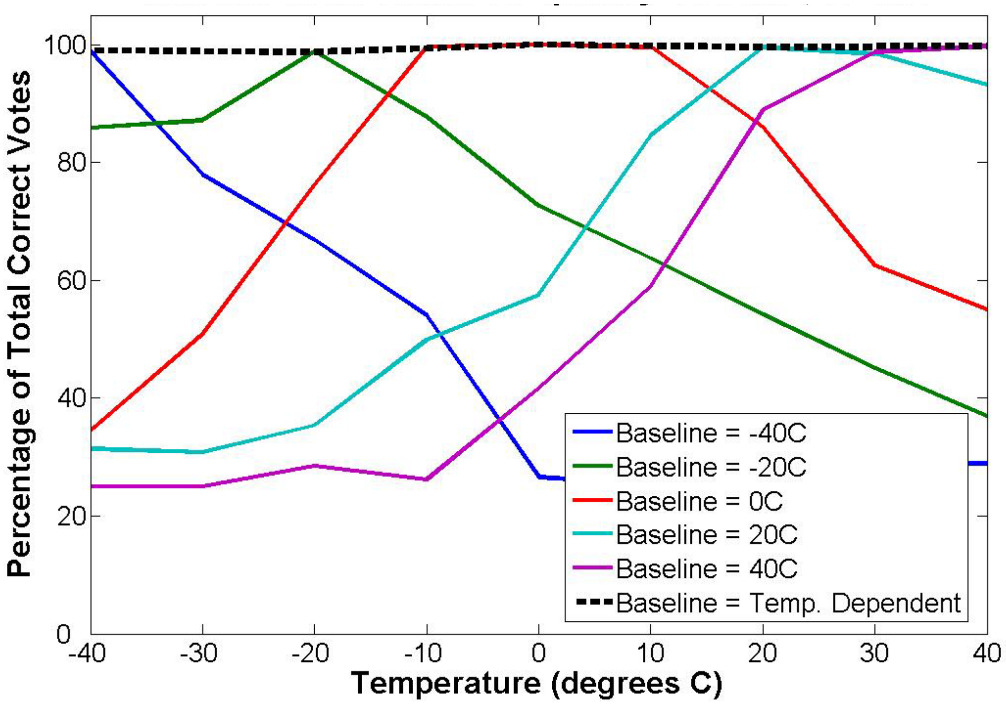

Figure 5.7. Percentage of total correct votes vs. temperature for cases in which the baseline AR coefficients are determined at various temperatures.

It is therefore possible to correct for temperature variations by storing baseline AR coefficients for the range of temperatures that the intended apparatus is likely to see during real world applications. It still must be determined how many sets of baseline AR coefficients must be stored and what the proper method for interpolation between these temperatures is. Therefore, this study examines using baseline AR coefficients taken every 20 degrees Celsius (-40°C, -20°C, 0°C, 20°C, 40°C) which is referred to in the following figures as 5tempbase and using baseline AR coefficients taken every 10 degrees Celsius (-40°C, -30°C , -20°C, -10°C, 0°C, 10°C, 20°C, 30°C, 40°C) which is referred to in the following figures as 9tempbase. Testing was carried out at 5 degree Celsius temperature increments. It can be seen in Figure 5.8 that the value of each AR coefficient tends to shift in a fairly reliable manner, usually in a near linear fashion, as the temperature changes. It is then possible to create a baseline of AR coefficients at all temperatures using polynomial fits from testing carried out at only a few intermediate temperatures.

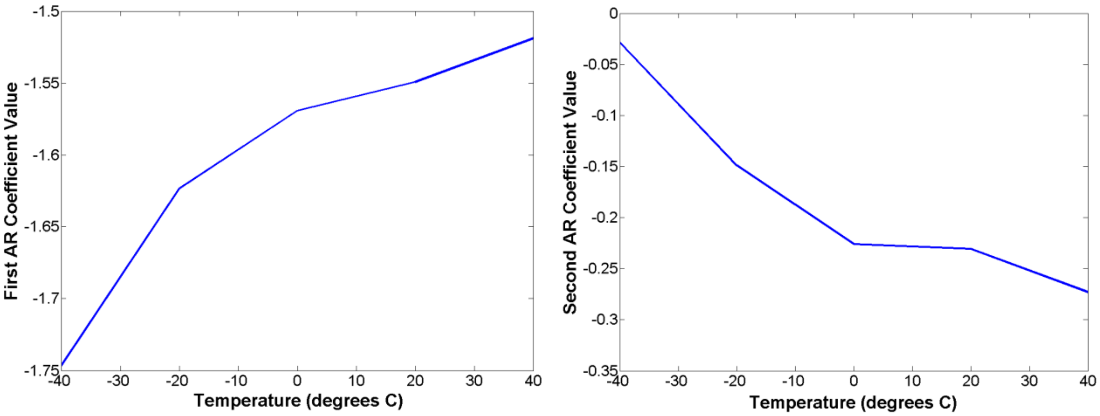

Figure 5.8. Actual coefficient values vs. temperature for the first (left) and second (right) AR coefficients.

Figure 5.9 shows the effectiveness of using various order polynomial fits (from linear to fourth order) to determine baseline AR coefficients for intermediate temperatures. It is clear that using baseline AR coefficients determined every 10 degrees Celsius produces better results than using baseline AR coefficients determined every 20 degrees Celsius. In both cases a fourth order polynomial produces the highest percentage of total correct votes over all temperatures with no lower result than 92% for the 5tempbase case and no lower result than 98% for the 9tempbase case. However, because the AR coefficients were being fit to a polynomial the optimal AR coefficients for a particular temperature were not always used as the polynomial does not necessarily go directly through this known data point.

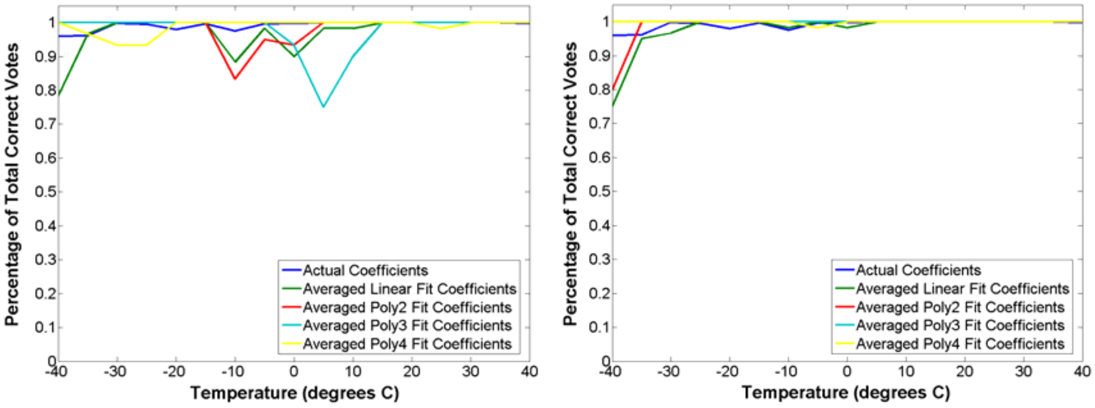

Figure 5.9. Percentage of total correct votes for various fitting techniques using the 5tempbase (a, left) and 9tempbase (b, right) methods.

Therefore, a lookup table method in which the AR coefficients for temperatures in the baseline database are directly used, and any intermediate temperatures are simply linearly interpolated, is also examined. Figure 5.10 shows the result of using this method. It is clear that even in the 5tempbase case (baseline AR coefficients determined in 20 degree Celsius increments) that linear interpolation of AR coefficients for intermediate temperatures results in 100% correct classification of individual test cases. This result is not surprising given that Figure 5.8 shows that the

AR coefficients trend almost piece-wise linear as temperature changes. This study therefore concludes that the best method for temperature correction is to store baseline coefficients for a small number of temperatures that span the known operational values of the structure and then to linearly interpolate via a lookup table the AR coefficients necessary to correctly classify bond condition for any intermediate temperatures.

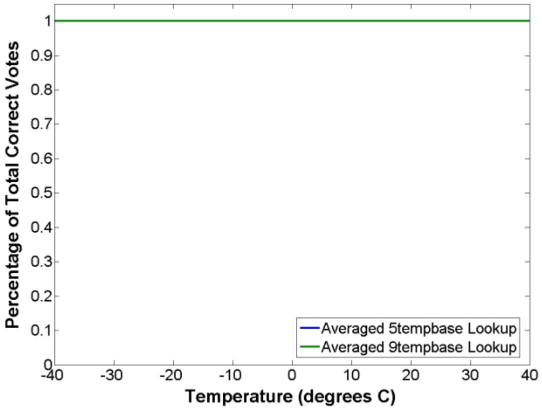

Figure 5.10. Percentage of total correct votes for direct linear lookup table using the 5tempbase and 9tempbase methods.

5.3.2 Multiple composite plates

The previous section showed the ability of the bond state assessment algorithm outlined in this study to compensate for temperature variations (variability due to the environment). Other types of variability that can affect the outcome of this scheme include unintentional inhomogeneities in a single manufactured specimen ("within-unit" variability) and inconsistencies in the manufacturing process itself across specimen lots ("unit-to-unit" variability). Within-unit variability includes the effects of manufacturing variability along the bond line, MFC bond condition inconsistency, and geometric effects that result from different placements of the MFC sensor/actuator pairs. This study examines the ability of the full two-part supervised learning classification scheme outlined in Section 3.2.2 to not only to classify disbond size but also to compensate for the different sources of variability discussed above. This classification is performed using data from a similarly configured composite bond for which baseline data are available. The test structures are again analogous to a wing skin-to-spar bonded joint and there is an MFC actuator/sensor pair for each bond condition to be identified on three composite wing-to-spar adhesive bonded joints. The test structures consist of a carbon fiber-reinforced plastic (CFRP) plate (manufactured by McMaster-Carr) that is bonded to a tubular CFRP spar using Loctite® Hysol® 9462 'Two Component Epoxy Adhesive'. The CFRP plate measures 12in x 12in x 0.016in square and the spar again has an outer square diameter of 2in x 2in with a wall thickness of 0.25in. The bonded area for two of the specimens contains two different sizes of disbond (0.25 in^2 and 1.0 in^2) that are created using Teflon inserts. The structures with disbonds are labeled Plate 1 and Plate 2. The third test structure (Plate 3) was manufactured with no disbonds so all paths are undamaged and geometric effects can be studied. The locations of the MFC actuators/sensors for Plate 1 and Plate 2 are pictured in Figure 5.11. C-scans that depict the bond state of each specimen can be seen in Figure 5.12.

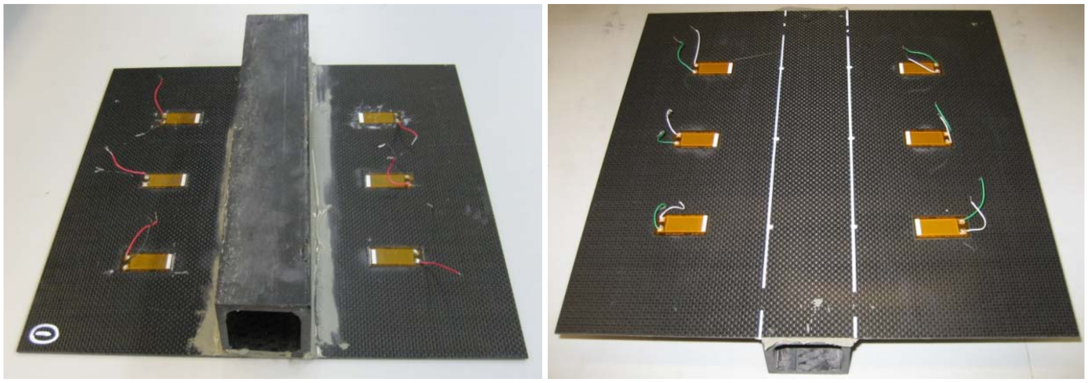

Figure 5.11. Experimental platform showing location of bottom-mounted MFC actuators on Plate 1 (a, left) and top-mounted MFC actuators on Plate 2 (b, right).

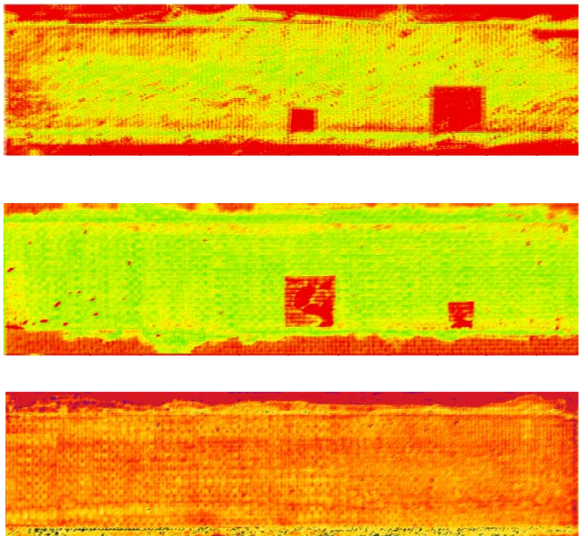

Figure 5.12. C-scan images showing locations and sizes of disbonds for Plate 1 (a, top) and Plate 2 (b, middle) as well as undamaged Plate 3 (c, bottom).

Plate 1 features two MFC actuator/sensors that are attached to the CFRP plate on each side of the bond for both of the damaged bond states as well as one pair for the undamaged bond area for a total of six MFC patches. The MFC patches are located on the spar side of the bond as seen in Figure 5.11. The MFC patches on Plate 2 are located on the opposite side of the CFRP plate from the bonded area. Plate 3 also has six MFC patches that are bonded on the spar side of the structure, as in Plate 1. Each of the MFC patches are bonded to the structure using Loctite® Hysol® E120HP^{TM} epoxy adhesive. Each MFC patch is affixed to the structure one inch from the spar bond line. Each input signal is applied to the structure 25 times and then averaged and filtered to reduce experimental noise.

For the following experiments, in order to test the ability of the classification scheme described in Section 3.2.2 to correctly identify bond condition, 90 time response histories are created using a specific set of signal creation parameters. Half of these 90 generated response time histories are selected as database training inputs. The remaining 45 responses are used as test set inputs. All three bond conditions on each structure are probed three times with the first two time history responses being used for the training database and the remaining responses used to determine bond condition for the test set inputs. In each case the actual bond condition is determined based solely on knowledge it acquired from the 45 database training inputs.

5.3.2.1 Optimal parameter investigation

A preliminary study is undertaken to determine the set of input signal parameters and extracted feature parameters (such as AR model order) that produce optimal bond state identification for the new set of test structures. This study uses receiver operating characteristic (ROC) curves as a means of identifying in a rigorous statistical manner the optimal parameters necessary for the classification scheme to operate efficiently, including the choice of alpha (Type-I error) that results in the best trade-off between Type-I and Type-II error.

The classification algorithm can have one of four outcomes for a particular test case. A true positive occurs when the bond being interrogated is damaged and the algorithm also concludes that it is damaged. If the algorithm concludes that this damaged bond is undamaged that is referred to as a false negative. A false positive occurs when the bond being interrogated is undamaged and the algorithm concludes that it is damaged. Similarly, if the algorithm correctly concludes that this undamaged bond is undamaged that is known as a true negative. ROC curves are formed by plotting the rate of true positives found by the classification scheme (true positives divided by true positives plus false negatives) against the false positive rate (false positives divided by false positives plus true negatives). Essentially, the more area under a ROC curve the better job of correctly identifying bond state that particular parameter is doing because there will be a high number of true positives compared to a low number of false positives.

The bond state assessment algorithm is used for an array of signal parameters and the overall ability of each set of parameters to correctly identify each bond state is then examined. In this study a number of excitation center frequencies from 100 kHz to 350 kHz are considered, as well as frequency ratios ranging from 0.15 (slightly chaotic) to 0.50 (highly chaotic). When considering the feature extraction parameters a number of AR model orders from 5 to 30 were employed. Figure 5.13a-d depicts the ability of the VCC/EVS-based statistical classification scheme to correctly identify bond condition by plotting the receiver operating characteristic (ROC) curve. This plot depicts the true positive rate against the false positive rate for all possible classifications (both undamaged and damaged).

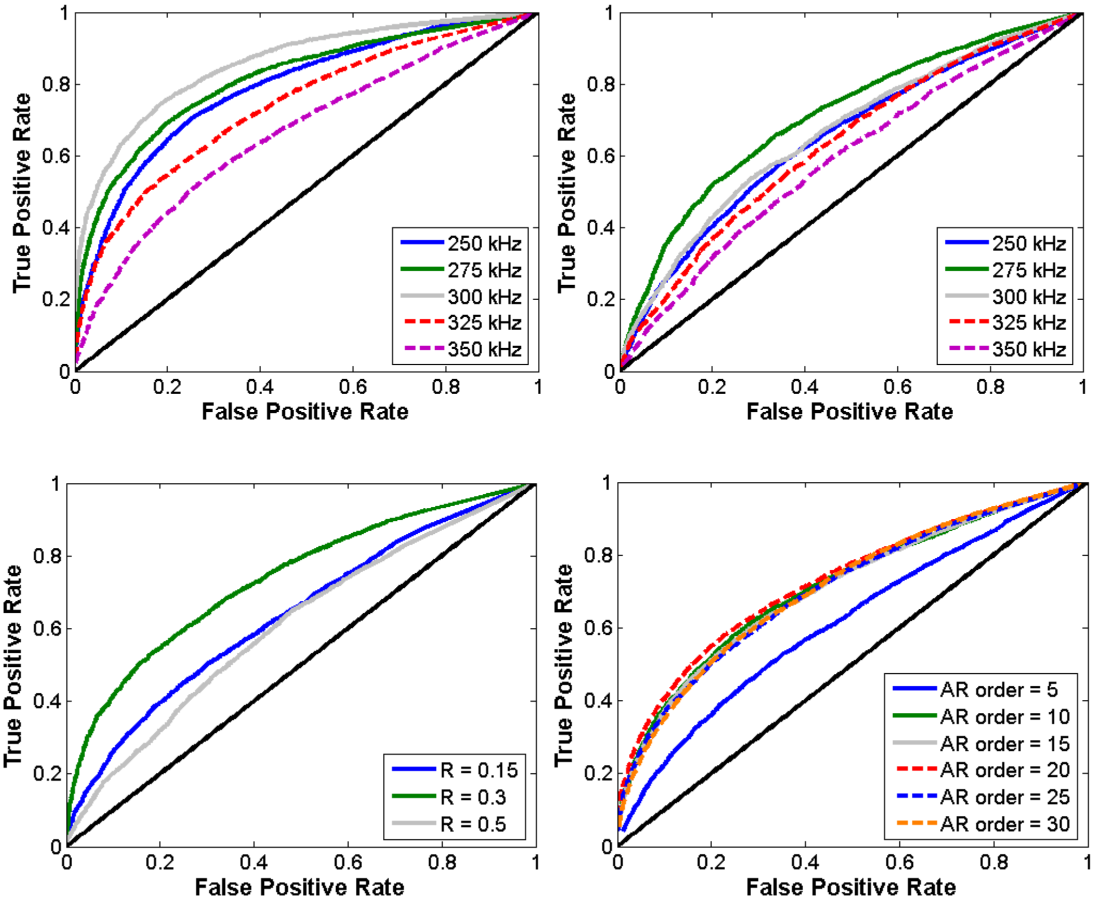

Figure 5.13. ROC curves for (a, top left) Plate 1 center frequencies, (b, top right) Plate 2 center frequencies, (c, lower left) Plate 1 frequency ratio R and (d, lower right) Plate 1 AR model order.

Figure 5.13a shows various ROC curves acquired by changing the center frequency of the excitation signals on Plate 1. Performance of the bond state assessment algorithm increases from a center frequency of 100 kHz up until 300 kHz, at which point the performance degrades as the center frequency continues to increase to 350 kHz (only center frequencies from 250 kHz to 350 kHz are shown here). This means that for the particular geometry of the test specimen and with MFC patches affixed to the same side of the plate as the bond line that a center frequency of 300 kHz is best suited for bond state assessment. Figure 5.13b depicts the same change in center frequencies as Figure 5.13a except that the data is from Plate 2 which has the MFC patches bonded on the opposite side of the bonded spar. There is similar behavior to the previous plot in which performance increases from 100 kHz to a particular optimal frequency and then decreases again. However in this case the optimal center frequency is 275 kHz. This change is due to the different way the guided wave propagates through the bond when introduced to the plate on the opposite side of the spar.

Figure 5.13c shows the ability of the statistical classification scheme employed together with chaotic insonification to correctly identify bond condition for various frequency ratios on Plate 1. A frequency ratio of 0.3 appears to be best suited for bond state assessment. The ROC curves for Plate 2 frequency ratios are very similar and again show that a frequency ratio of 0.3 is optimal. Figure 5.13d depicts the effect of AR model order on the damage identification ability of the statistical classification scheme. All AR model orders appear to work approximately equally well, except for an order of 5, with an AR model order of 20 performing the best among the group. Again Plate 2 shows similar results for the AR model order. It is not possible to create a ROC curve for Plate 3 as there are no true positive results because there is no damage (and thus, no hypothesis test). Figure 5.14 shows the optimal ROC curves for Plate 1 and Plate 2.

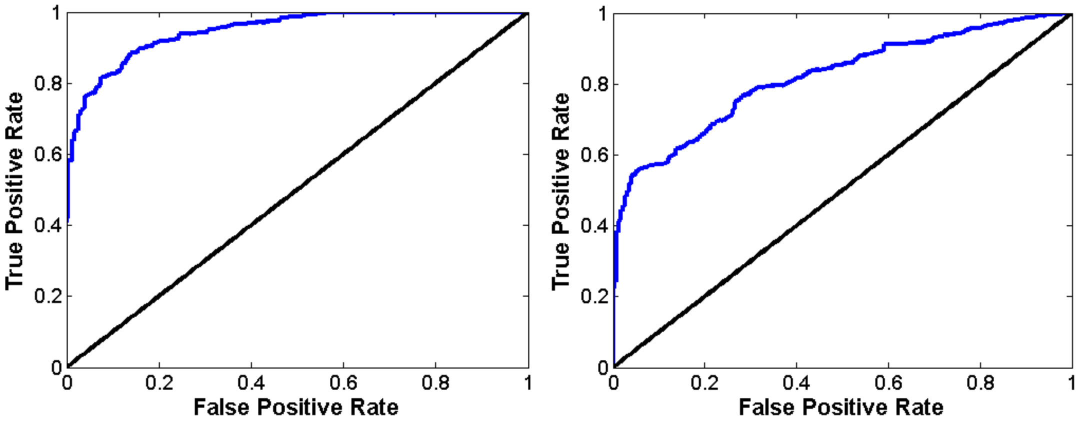

Figure 5.14. Optimal ROC curves for (a, left) Plate 1 and (b, right) Plate 2.

5.3.2.2 Temperature variability

The proposed classification scheme must still be evaluated for temperature robustness on the multiple wing skin-to-spar specimens in order to validate it for aerospace applications. This study again employs the use of a thermal chamber to test the efficacy of the above outlined method for temperatures varying from -40°C to 40°C, a range that covers most flight and ground conditions. The optimal set of parameters that will be used in the following experiments is a center frequency of 300 kHz for Plate 1 and Plate 3 (MFC patches on the same side as the bond) and a center frequency of 275 kHz for Plate 2 (MFC patches on the opposite side as the bond). A frequency ratio of 0.3 will be used for all specimens as well as an AR model order of 20. These are the most optimal parameters that were identified using ROC curves in the previous section.

5.3.2.2.1 Step one: damage existence classification

An alpha level of 0.05 (5% type I error) is used to choose the lower confidence limit for the undamaged VCC distribution. Figure 5.15 shows the percentage of outliers for each bond state being inspected on Plate 1 and Plate 2. This percentage of outliers is plotted against temperature and the "training database" of AR coefficient vectors has been acquired at each temperature. If the percentage of outliers is above the 5% type I error that has been specified, the bond state assessment algorithm has determined that the unknown bond being inspected is damaged.

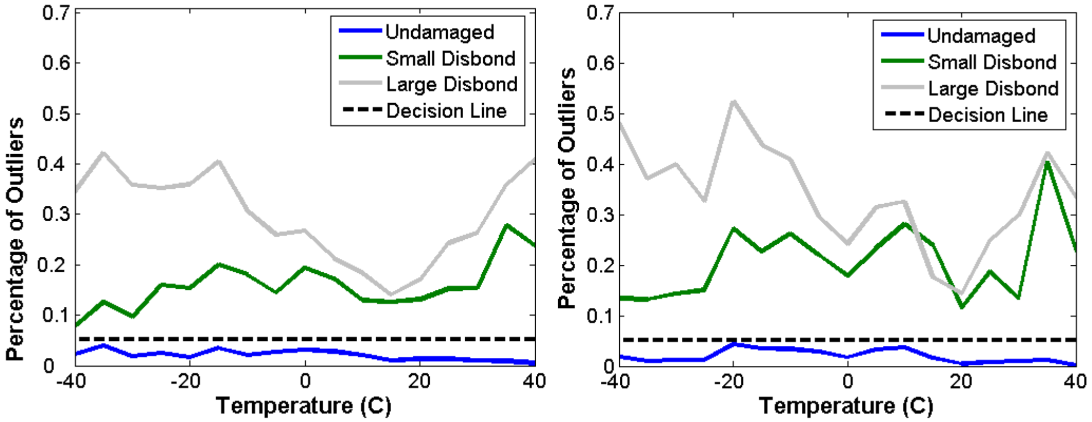

Figure 5.15. Percentage of outliers vs. temperature for each bond condition on (a, top left) Plate 1, (b, top right) Plate 2.

Figure 5.15a and Figure 5.15b show that for every temperature the undamaged path and paths with disbonds are correctly classified because the blue undamaged line is always below the decision boundary and the red and green disbond lines are always above the decision boundary. It is therefore possible to correct for temperature variations by storing baseline AR coefficients for the range of temperatures that the intended apparatus is likely to see during real world applications. However it is not necessary to store AR coefficients for all possible temperatures because only a few temperatures need to be stored and AR coefficients for intermediate temperatures can be linearly interpolated between existing baseline AR coefficients. This study again uses the 5tempbase and 9tempbase methods of AR coefficient interpolation outlined in Section 5.3.1.2. Testing is carried out at 5 degree Celsius temperature increments.

Figure 5.16 depicts the same results as are seen in Figure 5.15 except that AR coefficient values are linearly interpolated at temperatures for which no baseline data is present. The 5tempbase method depicted in Figure 5.16a works well except for two temperatures at which the number of outliers for the undamaged path rises above the critical threshold. The 9tempbase method shown in Figure 5.16b has 100% correct classification at all temperatures. This study reaffirms that the best method for temperature correction is to store baseline coefficients for a small number of temperatures that span the known operational values of the structure and then to linearly interpolate, via a lookup table, the AR coefficients necessary to correctly classify bond condition for any intermediate temperatures.

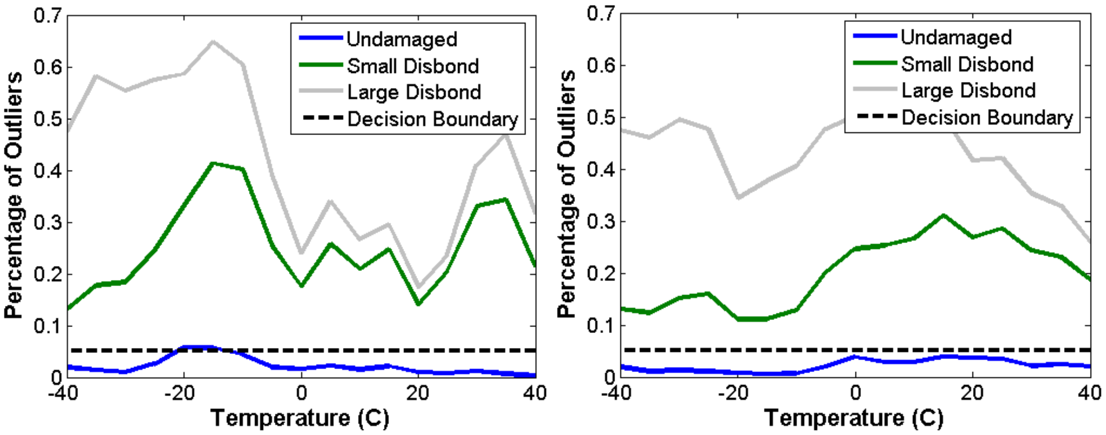

Figure 5.16. Percentage of outliers for Plate 2 using the 5tempbase (a, left) and 9tempbase (b, right) methods of AR coefficient interpolation.

5.3.2.2.2 Step two: disbond size classification

Having already determined what paths have some form of disbond or damage, the second bond state assessment algorithm employed in this study seeks to classify the size of the disbond. Figure 5.17 shows the percentage of total correct votes for each disbond size using either the 5tempbase or 9tempbase AR coefficient interpolation method for Plate 1 and Plate 2. The 5tempbase and 9tempbase methods appear to work equally well and the large disbond is correctly identified in almost 100% of individual cases. The small disbond is occasionally misclassified but the lowest result at 15°C on Plate 2 is still greater than 90% correct classification.

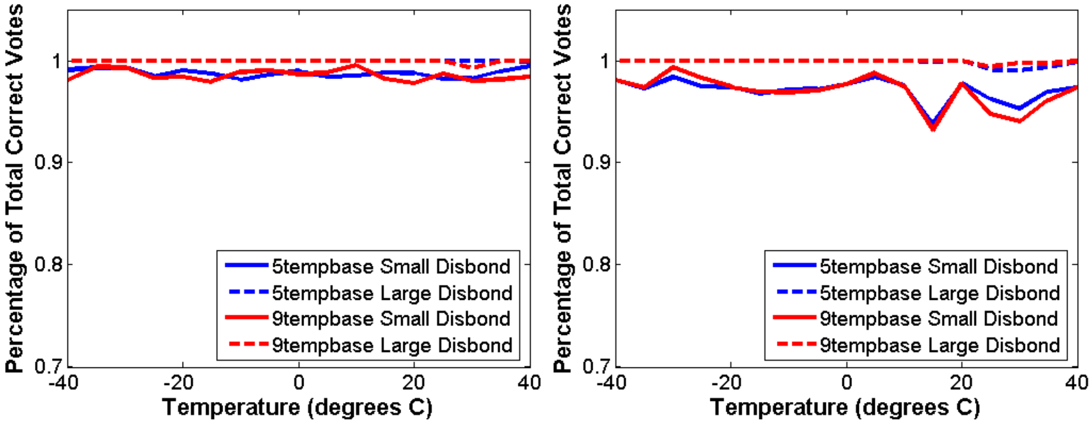

Figure 5.17. Percentage of total correct votes for each disbond size using the 5tempbase and 9tempbase AR coefficient interpolation methods on Plate 1 (a, left) and on Plate 2 (b, right).

5.3.2.3 Other sources of variability

It is possible to observe the resulting effects of within-unit variability by examining Plate 3, in which all paths were undamaged. Figure 5.18 shows the number of outliers using the VCC feature for Plate 3. In this figure, one path was chosen to be the baseline undamaged path and the other two paths were used as test cases. The number of outliers for each of the two test undamaged paths is above the 5% threshold but are less than 7.5% and much less than the number of outliers seen in the paths with disbonds on Plate 1 and Plate 2 shown in Figure 5.15a and Figure 5.15b. This result only comes from one test structure, but it appears that it may be possible to build a safety factor (in this case 1.5) into the lower confidence limit to account for the various sources of within-unit variability on a particular structure and still be able identify when and where the state of the bond has been changed. This result is important because it means it may not be necessary to store baseline data for every

MFC actuator/sensor pair in a structure as it may be possible to generalize baseline data from elsewhere in the structure as long as the geometries are similar.

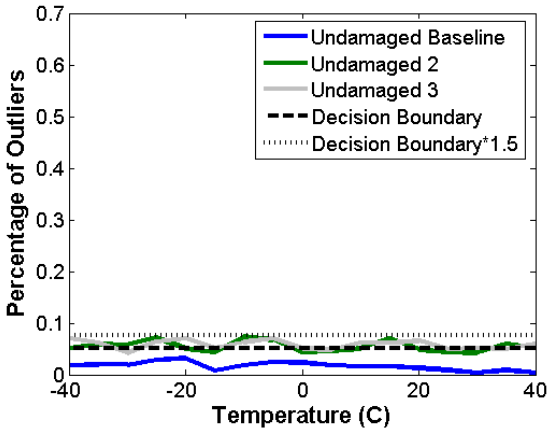

Figure 5.18. Percentage of outliers vs. temperature for each bond condition on Plate 3.

Unit-to-unit variability arises due to inconsistent manufacturing processes from specimen to specimen, which compound the within-unit sources of variability previously discussed. In well-controlled automated industrial applications with very tight tolerances or requirements, unit-to-unit variability is typically lower than within-unit variability. However, in this study each specimen was manufactured individually by hand, and consequently the unit-to-unit variability is considerably larger than within-unit variability. Figure 5.19 illustrates the large effect of this manufacturing inconsistency. Figure 5.19a shows averaged AR coefficients that are acquired using an AR model order of p=10 for the three different bond conditions on Plate 1 and the undamaged bond condition on Plate 3 that is in the same geometric location as the undamaged bond condition on Plate 1. Inspection of Figure 5.19a reveals that the AR coefficient vector from the undamaged bond condition on Plate 3 differs as much from the AR coefficient vector from the undamaged bond condition on Plate 1 as the AR coefficient vectors from the two disbond conditions on Plate 1. This large difference between the AR coefficient vectors from the undamaged bond condition in the same geometric location on each plate shows that the unit-to-unit variability is too large to use baseline data gathered on one specimen to discern the damage state of a second specimen. This conclusion is depicted graphically in Figure 5.19b, which shows the percentage of outliers vs. temperature for each bond state on Plate 1 using the undamaged bond condition on Plate 3 as the baseline undamaged condition. The percentage of outliers for the undamaged bond condition on Plate 1 is well above the decision boundary and would therefore be classified as damaged if the undamaged bond condition from Plate 3 were used as a baseline. Thus it is concluded that for the manufacturing techniques used in this study (individual test specimen construction by a non-expert human technician) that unit-to-unit variability is too large to allow for baseline data gathered from one plate to be used to diagnose the bond condition of a second plate. This result does not preclude the possibility that with more controlled manufacturing processes that unit-to-unit variability could be small enough that baseline data from only one specimen would be needed to properly assess the bond condition of a specimen lot.

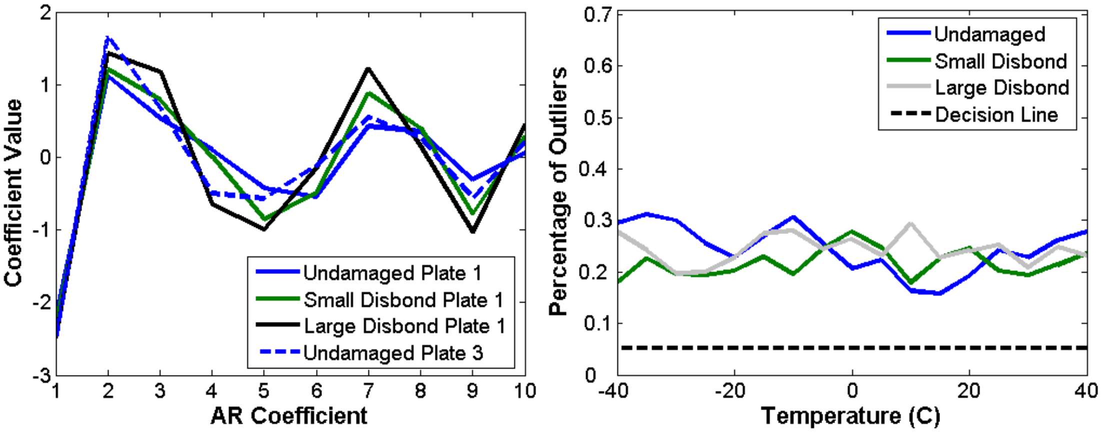

Figure 5.19. Averaged AR coefficient vector comparison for each bond condition on Plate 1 vs. undamaged bond condition on Plate 3 (a, left). Percentage of outliers vs. temperature for each bond condition on Plate 1 using undamaged bond condition on Plate 3 as the undamaged baseline (b, right).

5.4 Section summary

This study has shown the structural health monitoring capability of chaotically modulated ultrasonic waves that are imparted to a bolted metal joint or a composite bonded wing skin-to-spar structure through a piezoelectric patch. The classification damage detection scheme was shown to be effective in identifying bolt preload configuration in experiments on single and multiple joint structures. For the single composite structure experiment in Section 5.3.1 the damage size/type classification scheme is shown to be effective in identifying various bond damage states including different disbond sizes as well as poorly cured bonds and has the ability to compensate for temperature variation. This study has also shown the ability of a two-part bond state assessment algorithm to correctly classify the existence and size of a disbond within a composite bonded wing skin-to-spar structure. The use of vector consistency criterion (VCC) values derived from comparison of AR coefficient vectors, in combination with outlier analysis based on extreme value statistics, allows damage existence classification to be possible even without baseline data from every MFC sensor/actuator pair in a structure. Disbond size can then be determined in a supervised learning manner by employing a classification technique derived from information theory. This method also has the ability to compensate for temperature variability provided baseline AR coefficients have been recorded at a suitable number of temperatures that span the operating range of the structure (and that temperature is independently measured *in situ* during operation, which is, in practice, typically done).

6 CONCLUSIONS, CONTRIBUTIONS AND FURTHER WORK

6.1 Conclusions and contributions

The desire to push aging civil, mechanical, and aerospace structures beyond their intended design lives has highlighted the need for structural health monitoring (SHM) strategies that are able to detect, locate, and quantify various forms of damage within them with a goal of improved life cycle engineering from design to retirement. Recent advances in sensor technology, distributed networks, advanced signal processing techniques and pattern recognition algorithms have begun to be exploited for *in situ* SHM systems. SHM systems using active ultrasonic excitations are especially suited to the problem of damage localization and classification due to the high frequency regime (small wavelength) of the excitation signal. In most cases, however, the ultrasonic excitation signals and feature extraction techniques being employed for in-situ assessment are only applicable to relatively simple component geometries due to the highly complex modal interactions with boundaries and other impedance-mismatched substructures. This dissertation contributes to the growing body of knowledge in this field by introducing a new class of excitation signals and pattern recognition algorithms that, when paired with novel sensor networks, improve on the ability of standard SHM techniques to locate and identify various forms of damage on more complex geometry systems, with a focus upon bolted and adhesively-bonded composite joints.

This dissertation describes a methodology whereby chaotic guided waves are created and optimized (in a detection sense) and used as probes to perform damage assessment by building both time- and state-space domain models (rooted in pattern recognition) and using statistical modeling for performing damage classification under Type I/II error control. Multiple chaotic ultrasonic excitation formats are explored, including short-time chaotic wave packets and long-time chaotic bulk insonification, in which the diffuse, reverberant wave field is examined to identify changes commensurate with relevant damage modes. This method of insonification, in addition to enhanced pattern recognition techniques, allows this damage detection scheme to be employed on complex structural geometries with which *in situ* standard ultrasonic-based SHM methods cannot be used.

The outlined SHM method is applied to various test structures with different forms of induced damage including an aluminum plate with corrosion damage, bolted connections on several aluminum test structures (single and multiple-bolt configurations) and several adhesively-bonded composite wing-to-spar structures. The AR model-based classification schemes outline in Section 3.2 and used successfully on multiple test platforms in Section 5 are especially promising for use in continuous SHM because of their low computation requirements. Chaotic signal creation parameters are optimized for individual test structures and the outlined SHM method is shown to be able to correct for multiple sources of variability, such as temperature, within-unit variability and unit-to-unit variability.

6.2 Future work

There are several avenues of further work that can be evaluated to improve the efficacy of the proposed SHM method and verify its applicability to real-world structures. Issues that need to be examined include the relation of sensor/actuator density to damage classification effectiveness as well as how close an MFC needs to be placed to the monitored joint to be able to detect damage (range dependence). While beyond the scope of this dissertation, the specific placement of the MFC sensing array can have profound effects on the detection and classification ability of the approach (Flynn and Todd 2009). Also, in this research the optimal choice of parameters that affect the creation of the input time signals (carrier frequency f_c, frequency ratio R, modulation depth d) as well as feature extraction (AR model order, size of training and test databases) is largely determined by examining a range of values for each of these parameters and choosing the set of parameters that optimize detection capability. This *ad hoc* method works reasonable well, but it was shown in Section 5.2 that it may be possible to use genetic programming to determine a global optimum parameter solution that is not easily found by only testing a few finite parameter vectors. Using genetic algorithms (specifically differential evolution) to create an optimal input waveform for maximum damage discernment should greatly improve the effectiveness of the outlined SHM method.

Several issues regarding the use of this SHM method on real-world structures must also be examined. The effect of environmental noise was largely negated in each experiment by using highly shielded cabling. Such thick cabling may not be suitable for use in real-world structures (such as aircraft), and so the effects of noise on the ability of the classification algorithm to correctly identify damage location, type, and size may become more apparent. There is also a need to examine the effect that dynamic loading of a structure during in-service conditions will have on the efficacy of this SHM method. This is especially important for aerospace applications in which structural components undergo a significant dynamic load. The loading issue could be addressed by augmentation with either physics-based models (derived from finite element analyses) or probabilistic load models.

REFERENCES

Abarbanel, H.D.I. (1996). *Analysis of Observed Chaotic Data*, Springer: New York, NY.

Abbate, A., Koay, J., Frankel, J., Schroeder, S.C. and Das, P. (1997). Signal detection and noise suppression using a wavelet transform signal processor: application to ultrasonic flaw detection, *IEEE Trans. UFFC*, **44**: 14-26.

Allemang, R.J. (2003). The modal assurance criterion – twenty years of use and abuse, *Journal of Sound and Vibration,* **262**(3): 651-675.

Alleyne, D.N., Lowe, M.J.S. and Cawley, P. (1996). The inspection of chemical plant pipework using Lamb waves: defect sensitivity and field experience, In: *Review of progress in quantitative nondestructive evaluation*, Thompson, D.P. and Chimenti, D.E. (eds.), Plenum, New York: 1859–1866.

Arnhold, J., Grassberger, P., Lehnertz, K., and Elger, C.E. (1999). A robust method for detecting interdependences: Application to intracranially recorded EEG, *Physica D*, **134**:419-430.

Badii, R., Broggi, G., Derighetti, B., Ravani, M., Ciliberto, S., Politi, A. and Rubio, M.A. (1988). Dimension increase in filtered chaotic signals, *Phys. Rev. Let.,* **60**: 979-982.

Barron, R. (Editor) (1997). *Engineering Condition Monitoring: Practice, Methods and Applications*, Pierson Education.

Boller, C. and Staszewski, W.J. (2004). Aircraft structural health and usage monitoring, *Health Monitoring of Aerospace Structures – Smart Sensor Technologies and Signal Processing,* W.J. Stazewski, *et al.*, Eds. Wiley: Chichester, West Sussex, UK.

Bray, D. and McBride, D. (1992). *Nondestructive Testing Techniques*, John Wiley & Sons: New York.

Brockwell, P.J. and Davis, (1991) *Time Series: Theory and Methods,* Springer, New York, pp.113-118

Broomhead, D.S. and King, G.P. (1986). Extracting qualitative dynamics from experimental data, *Physica D*, **20**: 217-236.

Broomhead, D.S., Huke, J.P. and Muldoon, M.R. (1992). Linear filters and non-linear systems, *J. Royal Stat. Soc. B,* **54**: 373-382.

Bursi, O.S. and Jaspart, J.P. (1997). Basic issues in the finite element simulation of extended end plate connections, *Computers and Structures,* **43**: 17–42.

Bursi, O.S. and Jaspart, J.P. (1998). Benchmarks for finite element modeling of bolted steel connections, *Journal of Construction Steel Research,* **69**: 361–382.

Castaings, M., Cawley, P. and Farlow, R. (1996). Air-coupled ultrasonic transducers for the detection of defects in plates, In: *Review of progress in quantitative nondestructive evaluation*, Thompson, D.P. and Chimenti, D.E. (eds.), Plenum, New York: 1083–1090.

Castillo, E. (1988). *Extreme Value Theory in Engineering*, Academic Press, San Diego.

Chatterjee, A., Cusumano, J.P. and Chelidze, D. (2002). Optimal tracking of parameter drift in a chaotic system: experiment and theory, *J. Sound & Vib.,* **250**(5): 877-901.

Chelidze, D. and Cusumano, J.P. (2004). A dynamical systems approach to failure prognosis, *Journal of Vibration and Acoustics*, **126**(1): 1-7.

Cusumano, J.P. and Chatterjee, A. (2000). Steps towards a qualitative dynamics of damage evolution, *Int. J. Solids & Struct.,* **37**: 6397-6417.

Davies, M.E. and Campbell, K.M. (1996). Linear recursive filters and nonlinear dynamics, *Nonlinearity*, **9**: 487-99.

Davies, M.E. (1997). Reconstructing attractors from filtered time series, *Phys. D,* **101**: 195-206.

Doebling, S.W., Farrar, C.R., Prime, M.B. and Shevitz, D.W. (1996). Damage identification and health monitoring of structural and mechanical systems from changes in their vibration characteristics: A literature Review, Los Alamos National Laboratory Report, *LA-13070-MS.*

Doebling, S.W., Farrar, C.R. and Prime, M.B. (1998). A summary review of vibration-based damage identification methods, *Shock and Vibration Digest,* **205**: 631-645.

Farrar, C.R., Doebling, S.W., and Nix, D.A. (2001). Vibration-based structural damage identification, *Philosophical Transactions of the Royal Society A*, **359**: 131-149.

Farrar, C.R. and Worden, K. (2007). An introduction to structural health monitoring, *Philosophical Transactions of the Royal Society A*, **365**: 303-315.

Flynn, E. and Todd, M.D. (2009). Optimal placement of piezoelectric actuators and sensors for detecting damage in plate structures, *Journal of Intelligent Material Structures and Systems*, doi:10.1177/1045389X09338080.

Fraser, A.M. and Swinney, H.L. (1986). Independent coordinates for strange attractors from mutual information, *Physical Review,* **33:** 1134-40.

Giurgiutiu, V. and Zagrai, A. (2002). Embedded self-sensing piezoelectric active sensors for on-line structural identification, *ASME J. Vib. Acoust.*, **124**: 116-125.

Giurgiutiu, V. (2005). Tuned Lamb wave excitation and detection with piezoelectric wafer active sensors for structural health monitoring, *J. of Intell. Mat. and Struct.*, **16**: 291-305.

Grassberger, P. and Procaccia, I. (1983). Characterization of strange attractors, *Phys. Rev. Lett.* **50**: 346-349.

Griffiths, B. (2005). Boeing sets pace for composite usage in large civil aircraft, *High Performance Composites*, May Issue.

Guyott, C.H., Cawley, P. and Adams, R.D. (1986). The non-destructive testing of adhesively bonded structures, *Journal of Adhesion*, **20**: 129-159.

Guyott, C.H. and Cawley, P. (1988). Evaluation of cohesive properties of adhesive joints using ultrasonic spectroscopy, *NDT International*, **21**: 233-240.

Hall, S.R. and Conquest, T.J. (1999). The total data initiative – structural health monitoring, the next generation, *Proc. of the USAF ASIP, 2nd ed.*

Hess, D.P. (1998). Vibration and shock-induced loosening, In: *Handbook of Bolts and Bolted Joints*, Bickford, J.H. and Nasser S. (Eds.), Marcel Dekker, New York.

Kennel, M.B. and Abarbanel, H.D.I. (1992). Determining embedding dimension for phase-space reconstruction using a geometrical construction, *Physical Review A,* **45**: 3403-11.

Kumaraswamy, K., Megalooikonomou, V. and Faloutsos, C. (2004). Fractal dimension and vector quantization, **91**(3): 107-113.

Lanza di Scalea, F., Rizzo, P. and Marzani, A. (2004). Propagation of ultrasonic guided waves in lapshear adhesive joints: case of incident a0 Lamb wave, *J. Acoust. Soc. Am.*, **115**: 146-156.

Lanza di Scalea, F., Matt, H., Bartoli, I., Coccia, S., Park, G. and Farrar, C. (2007). Health monitoring of UAV wing skin-to-spar joints using guided waves and macro fiber composite transducers, *J. Intel. Mat. Sys. And Struct.,* **18**: 373-388.

Logan, D. and Mathew, J. (1996). Using the correlation dimension for vibration dault diagnosis of rolling element bearings – I. Basic concepts, *Mechanical Systems & Signal Processing*, **10**(3): 241-250.

Lowe, M.J.S. and Cawley, P. (1994). Applicability of plate wave techniques for the inspection of adhesive and diffusion bonded joints, *J. Nondestr. Eval.*, **13**: 185-200.

Matt, H., Bartoli, I. and Lanza di Scalea, F. (2005). Ultrasonic guided wave monitoring of composite wing skin-to-spar bonded joints in aerospace structures, *J. Acoust. Soc. Am.,* **118**(4): 2240-2252.

Michaels, J.E. and Michaels, T.E. (2005). Detection of structural damage from the local temporal coherence of diffuse ultrasonic signals, *IEEE Trans. UFFC*, **52**: 1769-82.

Moniz, L., Pecora, L., Nichols, J., Todd, M.D. and Wait, J.R. (2004). Dynamical assessment of structural damage using the continuity statistic, *Structural Health Monitoring,* **3**(3):199-212.

Nichols, J.M., Todd, M.D. and Wait, J.R. (2003). Using state space predictive modeling with chaotic interrogation in detecting joint preload loss in a frame structure experiment, *Smart Materials and Structures,* **12**(4): 580-601.

Nichols, J.M., Todd, M.D., Virgin, L.N. and Nichols, J.D. (2003). On the use of attractor dimension as a feature in structural health monitoring, *Mech. Syst. Signal. Process.*, **17**(6): 1305-1320.

Nichols, J.M., Todd, M.D., Seaver, M. and Virgin, L.N. (2003). Use of chaotic excitation and attractor property analysis in structural health monitoring, *Phys. Rev. E,* **67**: 016209.

Nichols, J.M., Nichols, C.J., Todd, M.D., Seaver, M., Trickey, S.T. and Virgin, L.N. (2004). Use of data driven phase space models in assessing the strength of a bolted connection in a composite beam, *Smart Materials and Structures*, **13**: 241-250.

Olson, C.C., Todd, M.D., Worden, K., and Farrar, C. (2007). Improving Excitations for Active Sensing in Structural Health Monitoring via Evolutionary Algorithms, *Journal of Vibration and Acoustics*, **129**, 784-802.

Olson, C.C., Overbey, L.A., and Todd, M.D. (2009). An experimental demonstration of tailored excitations for improved damage detection in the presence of operational variability, *Mechanical Systems and Signal Processing*, **23**(2): 344-357.

Olson, C.C., Overbey, L.A., and Todd, M.D. (2009). The effect of detection feature type on excitations bred for active sensing in structural health monitoring, *Journal of Intelligent Material Systems and Structures*, **20**(11): 1307-1327.

Pai, N.G. and Hess, D.P. (2002). Experimental study of loosening of threaded fasteners due to dynamic shear loads, *Journal of Sound and Vibration,* **253**: 585–602.

Pai, N.G. and Hess, D.P. (2002). Three-dimensional finite element analysis of threaded fastener loosening due to dynamic shear load, *Engineering Failure Analysis*, **9**: 383–402.

Paret, T.F. (2000). Extent of weld fracturing during Northridge earthquake, *J. Struct. Eng.*, **126**(1): 10-18.

Pecora, L.M. and Carroll, T.L. (1996). Discontinuous and nondifferentiable functions and dimension increase reduced by filtering chaotic data, *Chaos*, **6**: 432-439.

Pecora, L.M., Carroll, T.L. and Heagy, J.F. (1997). Statistics for continuity and differentiability: An application to attractor reconstruction from time series, *Fields Institute Communications*, **11**.

Pilarski, A. and Rose, J.L. (1992). Lamb wave mode selection concepts for interfacial weakness
analysis, *J. Nondestr. Eval.*, **11**: 237-249.

Rokhlin, S.I. (1991). Lamb wave interaction with lap-shear adhesive joints: theory and experiment, *J. Acoust. Soc. Am.*, **89**: 2758-2765.

Rytter, A. (1993). Vibration based inspection of civil engineering structures, Ph.D. Dissertation, Department of Building Technology and Structural Engineering, Aalborg University, Denmark.

Sauer, T., Yorke, J. and Casdagli, M. (1991). Embedology, *J. Stat. Phys.*, **65**: 579-616.

Schreiber, T. (1997). Detecting and analyzing nonstationarity in a time series with nonlinear cross predictions, *Phys. Rev. Lett.,* **78**: 843-846.

Seifried, R., Jacobs, L.J. and Qu, J. (2002). Propagation of guided waves in adhesive bonded components, *NDT&E Int.*, **35**: 317-328.

Shannon, C.E. and Weaver, W. (1949). *The Mathematical Theory of Communication,* University of Illinois Press, Chicago, pp. 75-83.

Sohn, H. and Farrar, C.R. (2001). Damage diagnosis using time series analysis of vibration signals, *Smart Materials and Structures*, **10**(3): 446-451.

Sohn, H., Farrar, C.R., Hunter, N.F. and Worden, K. (2001) Structural health monitoring using statistical pattern recognition,” *J. Dyn. Syst. Meas. Control*, **123**: 706-711.

Sohn, H., Farrar, C.R., Hemez, F.M., Shunk, D.D., Stinemates, D.W. and Nadler, B.R. (2003). A review of structural health monitoring literature: 1996 – 2001, *Los Alamos National Laboratory report*, LA-13976-MS.

Staszewski, W.J., Lee, B.C., Mallet, L. and Scarpa, F. (2004). Structural health monitoring using scanning laser vibrometry: I. Lamb wave sensing, *Smart materials and structures*, **13**(2): 251-260.

Storn, R. and Price, R. (1997). Differential evolution – A simple and efficient heuristic for global optimization over continuous spaces, *J. Global Optimization*, **11**(4): 341-359.

Takens, F. (1981). Detecting strange attractors in turbulence, *Dynamical Systems and Turbulence: Springer Lecture Notes in Mathematics,* **898,** eds Rand, D. and Young, L.S., pp. 366-381, Springer, New York, NY.

Theiler, J. (1986). Spurious dimension from correlation algorithms applied to limited time-series Data, *Phys. Rev. A*, **34**(3): 2427-32.

Todd, M.D., Nichols, J.M., Pecora, L.M. and Virgin, L.N. (2001). Vibration-based damage assessment utilizing state space geometry changes: Local attractor variance ratio, *Smart Materials and Structures,* **10**: 1000-1008.

Todd, M.D., Erickson, K., Chang, L., Lee, K. and Nichols, J.M. (2004). Using chaotic interrogation and attractor nonlinear cross-prediction error to detect fastener preload loss in an aluminum frame, *Chaos: An Interdisciplinary Journal of Nonlinear Science,* **14**(2): 387-399.

Todd, M.D., Nichols, J.M., Nichols, C.J. and Virgin L.N. (2004). An assessment of modal property effectiveness in detecting bolted joint degradation: theory and experiment, *Journal of Sound and Vibration*, **275**: 1113-1126.

Trendafilova, I. and Van Brussel, H. (2001). Non-linear dynamics tools for the motion analysis and condition monitoring of robot joints, *Mechanical Systems and Signal Processing*, **15**: 1141-1164.

Trickey, S., Todd, M., Seaver, M. and Nichols, J. (2002). Geometric time domain methods of vibration based damage detection, *Proc. SPIE Smart Nondestructive Evaluation for Health Monitoring of Structural and Biological Systems,* **4702**: 113-121.

Tuzzeo, D. and Lanza di Scalea, F. (2001). Non-contact air-coupled ultrasonic guided waves for detection of thinning defects in aluminum plates, *Research in Nondestructive Evaluation*, **13**(2): 61-78.

Wait, J.R., Park, G., Sohn H. and Farrar, C.R. (2004). Plate damage identification using wave propagation and impedance methods, *Proceedings of the SPIE 9th Annual International Symposium on NDE for Health Monitoring and Diagnostic,* **5394**, San Diego, CA, March.

Wilcox, P.D., Lowe, M.J.S. and Cawley, P. (1999). Long range Lamb wave inspection: the effect of dispersion and modal selectivity, In: *Review of progress in quantitative nondestructive evaluation*, Thompson, D.P. and Chimenti, D.E. (eds.), Plenum, New York: 151–158.

Worden, K., Allen, D.W., Sohn, H., Stinemates, D.W. and Farrar, C.R. (2002). Extreme value statistics for damage detection in mechanical structures, *Los Alamos National Laboratory Report,* LA-13903-MS.

Worden, K., and Manson, G. (2007). The application of machine learning to structural health monitoring, *Philosophical Transactions of the Royal Society A*, **365**: 515-37.

Xu, P.C., Mal, A.K. and Bar-Cohen, Y. (1990). Inversion of leaky Lamb wave data to determine cohesive properties of bonds, *Int. J. Eng. Sci.*, **28**: 331-346.